SP-1257 (1)

EarthCARE - Earth Clouds, Aerosols and Radiation Explorer

WALES - Water Vapour Lidar Experiment in Space

WATS - Water Vapour and Temperature in the Troposphere and Stratosphere

ACECHEM - Atmospheric Composition Explorer for Chemistry and Climate Interaction

SPECTRA - Surface Processes and Ecosystem Changes Through Response Analysis

MISSION28

REPORTS FOR ASSESSMENT

THE FIVE CANDIDATE EARTH EXPLORER CORE MISSIONS

European Space Agency
Agence spatiale européenne

ESA SP-1257(1)
September 2001

Reports for Assessment
THE FIVE CANDIDATE EARTH EXPLORER CORE MISSIONS

EarthCARE – Earth Clouds, Aerosols and Radiation Explorer

European Space Agency
Agence spatiale européenne

ESA SP-1257(1) – The Five Candidate Earth Explorer Core Missions -
EarthCARE – Earth Clouds, Aerosols and Radiation Explorer

Report prepared by:	Earth Sciences Division *Scientific Co-ordinator:* J. P. V. Poiares Baptista Earth Observation Preparatory Programme *Technical Co-ordinator:* W. Leibrandt
Cover:	Carel Haakman
Published by:	ESA Publications Division c/o ESTEC, Noordwijk, The Netherlands *Editors:* R.A. Harris & B. Battrick

ISBN 92-9092-628-7
ISSN 0379-6566

Price (5 vols.): €60

Contents

1 Introduction

The ESA Living Planet Programme includes two types of complementary user driven missions: the research-oriented Earth Explorer missions and the operational service oriented Earth Watch missions. These missions are implemented via two programmes: the Earth Observation Envelope Programme (EOEP) and the Earth Watch Programme. The Earth Explorer missions are completely covered by the EOEP.

There are two classes of Earth Explorer missions. The Core missions are larger missions addressing complex issues of wide scientific interest. The Opportunity missions are smaller missions in terms of cost to ESA, addressing more limited issues. Both types address the research objectives of the Earth Explorers, which are being implemented according to well-established mechanisms (ESA, 1998). The missions are proposed, defined, evaluated and recommended by the scientific community.

Core and Opportunity missions are implemented in separate cycles. A new cycle is started every four years. The missions are implemented per cycle. The two missions selected in the first cycle of the Earth Explorer Core missions are underway: the Gravity field and steady-state Ocean Circulation Explorer (GOCE) and the Atmospheric Dynamics Mission (ADM-Aeolus), scheduled for launch in 2005 and 2007, respectively. The first cycle of Earth Explorer Opportunity missions is also on-going and will result in the CryoSat and Soil Moisture and Ocean Salinity (SMOS) missions, to be launched in 2004 and 2006, respectively.

This report concerns the second cycle of Earth Explorer Core missions. As a result of the second Call for Ideas for Earth Explorer Core missions, which was released in June 2000, five missions were selected in Autumn 2000 for the second step of the implementation mechanism, i.e. the assessment. These missions are ACECHEM (Atmospheric Composition Explorer for CHEMistry and climate interaction), EarthCARE (Earth Clouds, Aerosols and Radiation Explorer), SPECTRA (Surface Processes and Ecosystems Changes Through Response Analysis), WALES (WAter vapour Lidar Experiment in Space), and WATS (WAter vapour and temperature in the Troposphere and Stratosphere). Reports for Assessment have been prepared for each of these candidate missions .

These reports will be circulated among the Earth Observation research community in preparation of the 'Earth Explorers Granada 2001 User Consultation Meeting', which will be held in Granada, Spain at the end of October 2001. The consultation meeting is part of the evaluation of the candidates that should lead to the selection of three of them for feasibility studies in 2002-2003 and further to the selection of the next two Earth Explorer Core missions to be launched in 2008 (Core-3) and 2010 (Core-4).

This particular 'Report for Assessment' is concerned with the EarthCARE (Earth Clouds, Aerosols and Radiation Explorer) mission. It was prepared by a mission Joint Drafting Team consisting of members of the EarthCARE Scientific Preparatory Group (SPG): A.J. Illingworth (University of Reading, Reading, UK), R.S. Kandel (LMD, Eçole Polytechnique, Palaiseau, France), Hiroshi Kumagai (Communication Research Laboratory, Tokyo, Japan), André van Lammeren (KNMI, De Bilt, The Netherlands), Jean-François Mahfouf (ECMWF, Reading, UK), Teruyuki Nakajima (CCSR, University of Tokyo, Japan), Hajime Okamoto (Tohoku University, Sendai, Japan), Jacques Pelon (Service d'Aeronomie/IPSL, Paris, France) and Makoto Suzuki (EORC, NASDA, Tokyo, Japan).

They were supported by the other members of the EarthCARE Joint SPG, namely Albert Ansmann (Institute of Tropospheric Research, Leipzig, Germany), Kazuo Asai (Tohoku Institute of Technology, Sendai, Japan), Franz H. Berger (Dresden University of Technology, Germany), Jean-Pierre Blanchet (Université du Québec à Montréal, Canada), Yasushi Fujiyoshi (Hokkaido University, Sapporo, Japan), Ernesto Lopez-Baeza (Universidad de Valencia, Spain), Martin Miller (ECMWF, Reading UK), Rolando Rizzi (Università di Bologna, Italy), Nobuo Sugimoto (National Institute of Environment Studies, Tsukuba, Japan), Tamio Takamura (Chiba University, Chiba, Japan) and Takashi Yamanouchi (National Institute of Polar Research, Tokyo, Japan).

Further scientific contributions to this report have been made by various other scientists, in particular by David Donovan (KNMI, The Netherlands), Robin Hogan (University of Reading, UK), Markus Quante (GKSS, Germany), Ehrhard Raschke (GKSS, Germany) and Jacques Testud (CETP/IPSL, France).

The technical content of the report (notably Chapter 6) has been jointly compiled by ESA (Fabrizio Battazza, Jean-Loup Bézy, Arnaud Hélière, Chung-Chi Lin, Joaquin Muñoz and Pierluigi Silvestrin), based on inputs derived from the industrial pre-Phase-A contractors and by the National Space Development Agency of Japan (Yasumasa Hisada, Riko Oki, Kayoko Kondo, Nobuhiro Kikuchi), and the Communications Research Laboratory (Satoru Kobayashi, Hiroshi Kuroiwa). Einar-Arne Herland, Alberto Tobias (ESA) and Chu Ishida (NASDA) should also be acknowledged for their time and effort in reviewing this document and Drusilla Wishart for preparing it for publication.

The difficulty of representing clouds and aerosols and their interactions with radiation, constitutes a major source of uncertainty in predictions of climate change using numerical models of atmospheric circulation. Accurate representation of cloud processes is also critical for the improvement of numerical weather prediction. A first step in gaining confidence in such predictions is to check that these models are at least correctly representative of the clouds and aerosols in the present climate. Unfortunately there are no global datasets, providing, simultaneously, the vertical profiles of clouds and aerosol characteristics together with vertical temperature and humidity profiles and the top-of-the-atmosphere (TOA) radiance. Such datasets are crucial to validate the model parameterisations of cloud processes regarding both water and energy fluxes. The vertical profiles are important in controlling the radiative transfer processes in the atmosphere, and so affect the heating profiles, which then influence the dynamics.

Indirect aerosol effects on cloud radiative forcing as well as cloud parameterisation are today the biggest sources of uncertainty in climate prediction. The critical cloud radiation feedback cannot be modelled without accurate cloud and aerosol parameterisations.

For these reasons, EarthCARE has been specifically defined with the *scientific objectives* of determining for the first time, in a radiatively consistent manner, the global distribution of vertical profiles of cloud and aerosol field characteristics to provide basic, essential input data for numerical modelling and global studies of:

- the divergence of radiative energy
- the aerosol–cloud–radiation interaction
- the vertical distribution of water and ice and their transport by clouds
- the vertical cloud field overlap and cloud-precipitation interactions.

Such data will be used to evaluate the performance of current models, to improve the parameterisation schemes in such models and thus provide better and more reliable predictions.

All the 'Reports for Assessment' follow a common general structure comprising seven chapters. Following this introduction, the report is divided into six chapters:

Chapter 2 addresses the background and provides the scientific justification for the mission set in the context of issues of concern and the associated need to advance current scientific understanding. The chapter identifies the problem and gives the relevant background. It provides a clear identification of the potential 'delta' this mission would provide.

Drawing on these arguments, Chapter 3 discusses the importance of the scientific objectives. It identifies the need for such observations by comparing the data that will be provided by this mission with those available from existing and planned sources, highlighting the unique contribution of the mission.

Chapter 4 focuses on observational requirements based on generic requirements and derives, in the context of the scientific objectives, the mission specific observational requirements.

Chapter 5 provides an overview of the mission elements and their requirements and also discusses external sources required but also other missions benefiting from the mission.

Drawing on Chapter 5, Chapter 6 provides a complete summary description of the proposed technical concept (space and ground segments), establishes basic system feasibility and provides a preliminary assessment of the expected performance.

Chapter 7 outlines programme implementation, including risks, and expected development schedule. In particular, drawing on the previous chapters, it discusses EarthCARE in the context of other related missions.

2 Background and Science Issues

2.1 The Climate Problem – An Overview

The significant transformation of the Earth's atmosphere by human agricultural and industrial activities constitutes the most serious global environmental problem today, bringing with it the threat of accelerating climate change affecting all human societies and the biosphere. Due to the cumulative nature of many greenhouse gas emissions, governments urgently need to make major political and economic decisions, many involving long-term commitments. Whether for mitigation or adaptation strategies, such decisions must be based in part upon predictions of future global warming. Scientists and governments have organised the Intergovernmental Panel on Climate Change (IPCC), in particular to assess the state of the science of climate change. In its third report (IPCC, 2001), predictions of 'global warming' range from 1.4 to 5.8 K (Figure 2.1) with an even wider range for regional scales.

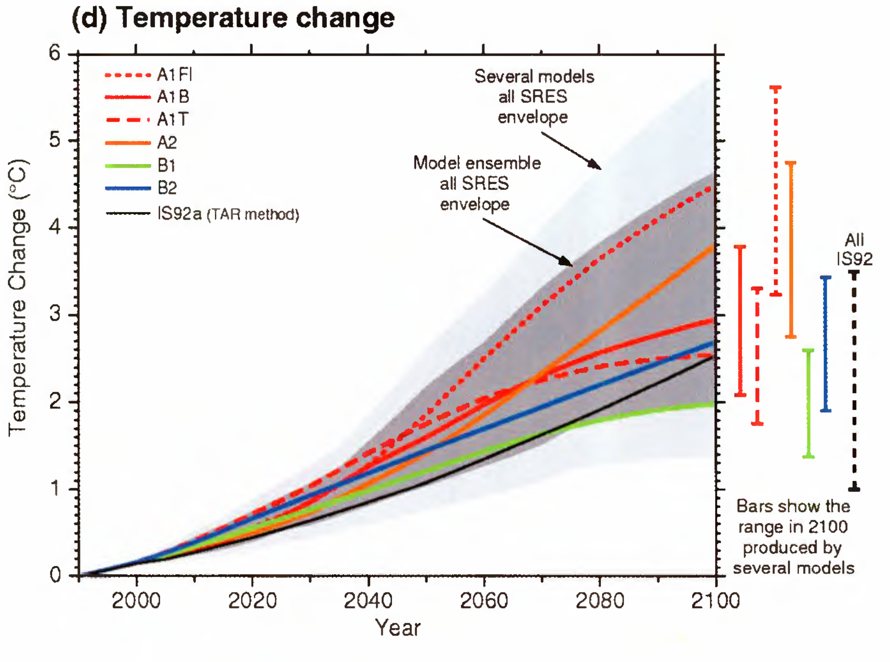

Figure 2.1: *Temperature change (°C) for the 21st century as computed using the SRES emissions scenarios (SRES, 2000) family, and different climate models. The dark shaded envelope shows the range of warming corresponding to the different scenarios considered, for a single climate model. The light shaded envelope shows the still broader range when climate uncertainties are included. The coloured bars to the right show the ranges in global warming predicted for 2100 by different models, for individual emission scenarios (IPCC, 2001).*

A part of this range is related to different social development assumptions (and consequently emission scenarios). However, a large part of this range of uncertainty, as can be seen from the model range bars at the right of Figure 2.1, arises from the limited knowledge in atmospheric sciences, notably with regard to the interactions of clouds and aerosols with radiation.

One need only consider activities such as agriculture, transport, construction and insurance, to realise that predictions of climate variability over different spatial and temporal scales are of enormous social and economic value. The value of climate simulations is further enhanced in a world in which global change means that the statistics of the past will be an increasingly poor guide to the future. All such predictions rely on numerical models representing physical processes in the atmosphere and oceans. Although the laws governing these processes are well known, the simulations remain imperfect. In its Third Assessment Report, the IPCC (2001) notes that "there are particular uncertainties associated with clouds and their interaction with radiation and aerosols", and moreover "there has been no apparent narrowing of the uncertainty range associated with cloud feedbacks in current climate simulations"; it further recommends that "the only way to obtain progress in this complex area of atmospheric science is by consistently combining observations with models" and that "a more dedicated approach is needed".

As mentioned earlier, large uncertainties arise from shortcomings in the treatment of cloud and aerosol processes in climate models and the lack of observations to validate cloud and aerosol parameterisation schemes. The same difficulties bedevil numerical weather prediction models used for short- and medium-range as well as seasonal forecasting. All such models divide the atmosphere into a series of grid boxes, typically 30-50 km in the horizontal (100 to 250 km for climate models) and 500 m in the vertical. For each box, clouds are represented by prognostic variables such as fractional cloud cover, ice and liquid water content, together with some implied cloud overlap for each vertical stack of grid boxes. The overlap assumptions affect both the radiative transfer and the precipitation efficiency of the clouds. There are scarcely any observations to evaluate whether this representation is correct.

A particularly glaring gap is our virtual ignorance of the depth and water content of the widespread tropical ice clouds. A first step is to evaluate whether the current weather and climate are being correctly represented in numerical models, to obtain more confidence in the climate predictions and thus help to provide a universally agreed-upon basis for action both by governments and economic decision-makers. An attempt to do this has involved the use of ISCCP (International Satellite Cloud Climatology Project) cloud data in the AMIP (Atmospheric Model Inter-comparison Programme) comparisons. Figure 2.2 shows that in the latest AMIP comparisons, even though the models are able to produce similar Top-Of-Atmosphere (TOA) up-welling radiative fluxes, they have mean values of vertically integrated cloud water which vary by over

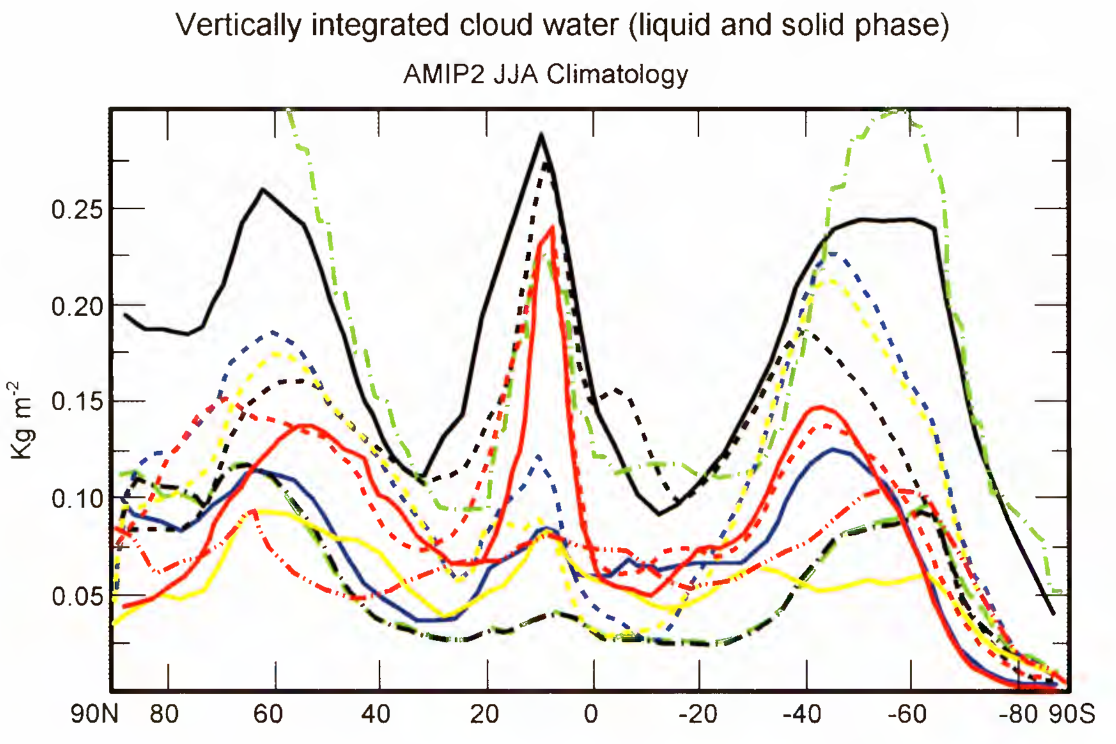

Figure 2.2: *Zonal average of vertically integrated total cloud water path for 14 different climate models for June, July and August (AMIP). Note the significant differences between integrated cloud water. All models were able to produce comparable top-of-the-atmosphere upwelling fluxes.*

an order of magnitude from one model to another, and consequently very different heating profiles, which also result in very different weather patterns.

Expressed as global warming, climate sensitivity depends critically on cloud feedback. In general, more low-level clouds cool the Earth by reflecting sunlight back to space, but additional high level cold clouds tend to warm the Earth by losing less infrared radiation to space. Because any climate change almost inevitably involves changes in cloud cover and cloud properties, 'cloud radiative feedback' can either amplify the original direct radiative forcing or counteract it.

Figure 2.3 provides a striking illustration of how changes in the vertical profile of clouds lead to different heating rates. Consequent important changes in the cloud profiles can then feed back to changes in the atmospheric dynamics. Current satellites constrain the total incoming and outgoing radiation at TOA, but cannot provide reliable observations of cloud vertical structure and consequent energy heating profiles and surface fluxes and their relationships with water vapour and the associated feedback.

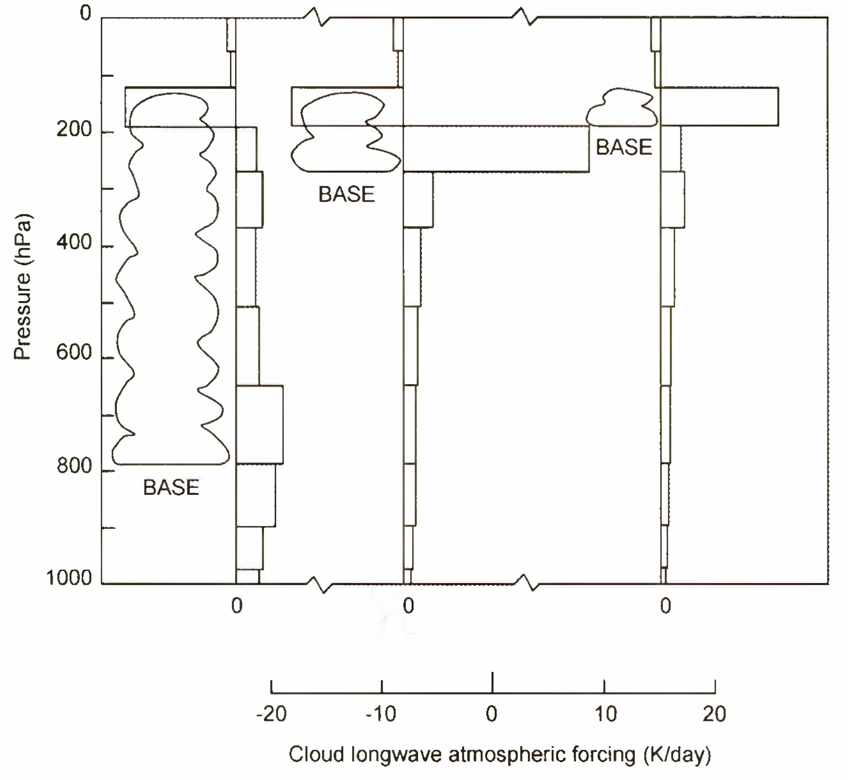

Figure 2.3: *Infrared radiative heating/cooling profiles, calculated for three different cloud base levels (after Slingo and Slingo, 1988). These profiles demonstrate the need for an accurate knowledge of upper and, in particular, lower cloud boundaries.*

The latest IPCC report (Figure 2.4). lists twelve external factors that can force climate change. Note that this figure does not explicitly include clouds because they are not an external factor, although cloud processes play a role in many of the forcings. The change in forcing due to greenhouse gases themselves is high and fairly accurately known, but the five factors judged to have the greatest degree of uncertainty all involve aerosols, with a 'very low level of scientific understanding'. Changes in aerosols can have a significant direct effect by modifying the solar (short-wave) radiation flux reaching the ground, and also affect biochemical and photochemical processes in the atmosphere and clouds. Figure 2.5 shows an example of a simulation of aerosol optical thickness used in one of the climate models in Figure 2.1. The latter shows that certain types of aerosols are transported for long distances, surrounding the globe and producing significant radiative forcing and changes in the cloud field even in remote ocean regions.

The factor identified by the IPCC with the biggest known uncertainty is the 'indirect aerosol' effect that operates by (i) increasing the cloud albedo by decreasing the droplet size, and (ii) changing the cloud lifetime and precipitation efficiency. Effect (i) is potentially the largest and almost as big as the greenhouse forcing, but has the highest uncertainty of all by a large margin. There is so much uncertainty over effect (ii) that it is the only factor that the IPCC was unable to quantify, stating that "No best estimate can be given".

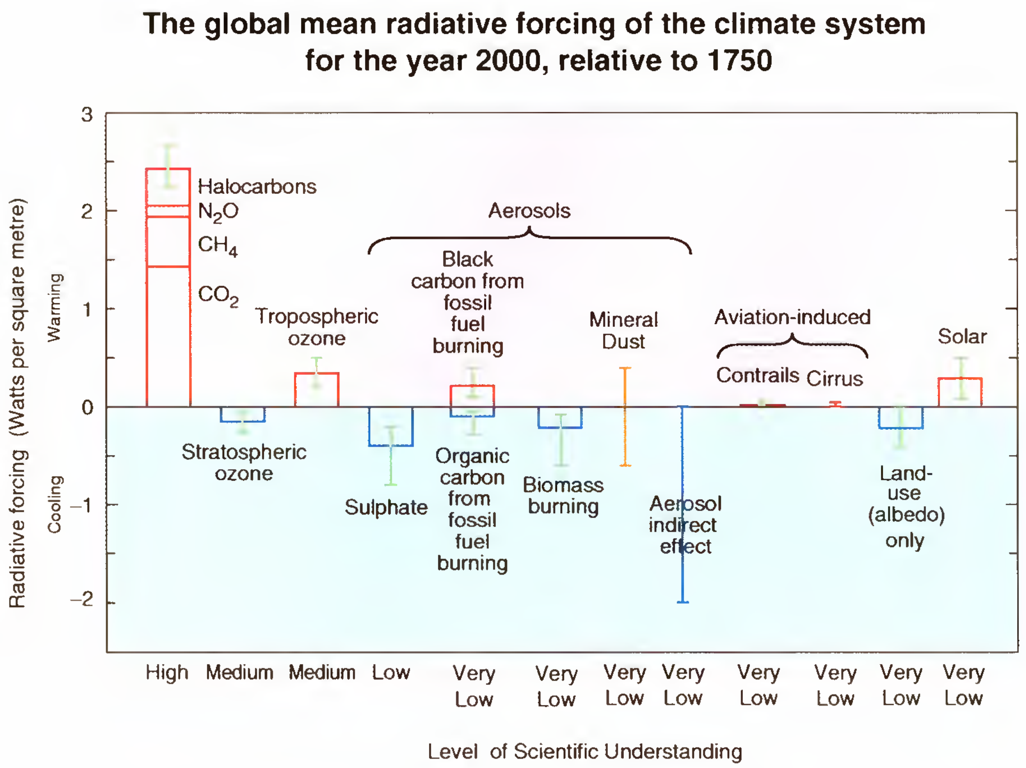

Figure 2.4: *Many external factors force climate change. The bars in the figure provide an estimate of the estimated error from each of these factors. The level of scientific understanding is also shown (IPCC, 2001).*

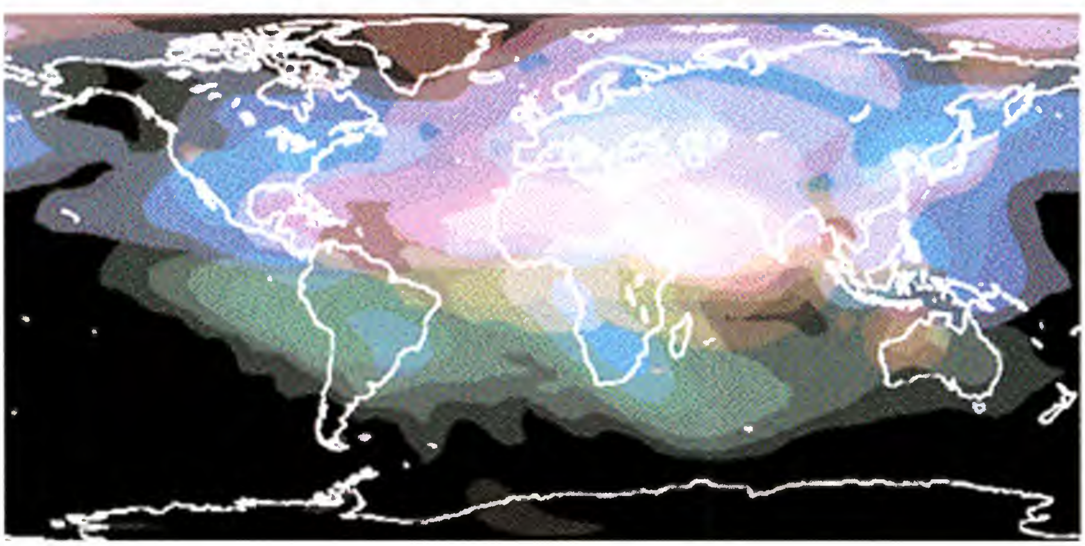

Figure 2.5: *Simulation of global distribution of aerosol optical thickness with CCSR/NIES global climate model implemented aerosol generation/transport processes. Logarithm of optical thickness for each aerosol type of mineral dust (red), sulphate (blue), and carbonaceous (green) are shown. Case of July 1990 (3D-CLARE, 1999).*

Concluding Remarks

As briefly discussed above (for a more detailed discussion see the sections below), indirect aerosol effects on cloud radiative forcing as well as cloud parameterisation are today the biggest sources of uncertainty in climate prediction. The critical cloud radiation feedback cannot be modelled without accurate cloud and aerosol parameterisations.

For these reasons, EarthCARE has been specifically defined with the scientific objectives of determining for the first time, in a radiatively consistent manner, the global distribution of vertical profiles of cloud and aerosol field characteristics to provide basic essential input data for numerical modelling and global studies of:

- the divergence of radiative energy
- the aerosol-cloud-radiation interaction
- the vertical distribution of water and ice and their transport by cloud
- the vertical cloud field overlap and cloud-precipitation interactions.

2.2 Climate Change Forcing, Feedbacks and Existing Observations

2.2.1 Global Warming?

There recently has been increased awareness of the possibility or likelihood of significant changes in the probability distribution of 'extreme events'. However, public discourse concerning observed climate change in the 20th century and anticipated climate change in the 21st century has mostly proceeded in terms of 'global warming', with the planet's climate state subsumed by a single parameter, the global annual mean surface air temperature T.

This simplification, though extreme, allows discussion of the causes of climate changes of the recent past and those expected in the near future in terms of perturbations of the planet's energy balance, identified as radiative forcing in as much as energy exchange of the planet with its environment (Sun and space) is in practice entirely radiative.

Real climate involves complex regional and seasonal patterns of precipitation as well as temperature. Modern climate change simulations make use of three-dimensional general circulation models of the atmosphere–ocean system. Still, results of these simulations are often summarised and interpreted globally. A zero-dimensional conceptual model with climate state parameter T and with three climate control factors can represent this:

- solar 'constant' S, the external source of short-wave (SW) radiative energy flux;
- planetary albedo a, defining the fraction of the mean incident flux S/4 that is not transformed into heat in the Earth-atmosphere system;
- normalised greenhouse factor g (Raval and Ramanathan, 1989), defining the fraction of the thermal radiation flux emitted at the Earth's surface that is not evacuated to space.

Considering a planetary climate state in radiative equilibrium, denoted by the subscript zero, with climate state represented by global mean surface temperature $T = T_0$, planetary albedo $\alpha = \alpha_0$, and normalised greenhouse factor $g = g_0$, the flux $M_{LW} = \sigma(1\text{-}g_0)T_0^4$ of thermal long-wave (LW) radiation from the planet to space is equal to the absorbed solar (SW) radiative flux $M_{abs} = (S_0/4)\,(1\text{-}\alpha_0)$, so that the net radiation (radiation balance) R_N is zero.

$$R_N = 0 = M_{abs} - M_{LW} = \left(\frac{S_0}{4}\right)(1 - \alpha_0) - \sigma(1 - g_0)\,T_0^4 \qquad (2.1)$$

The equilibrium state with global mean surface temperature T_0 (= 288 K) corresponds to solar constant S_0 (= 1368 Wm^{-2}), planetary albedo α_0 (= 0.30), and greenhouse factor g_0 (= 0.39). Radiative *forcing F* of climate change can be written in terms of external perturbations ΔS, $\Delta\alpha$ and Δg of the climate system, evaluating the resulting non-zero net radiation without taking into account further changes $\Delta\alpha'$ and $\Delta g'$ (*feedbacks*) resulting from a change in the state of the system (here represented by changes ΔT in global mean surface temperature).

$$F = F_{SW} + F_{LW} \qquad (2.2)$$

$$F_{SW} = (1 - \alpha_0)\,\frac{\Delta S}{4} - \left(\frac{S_0}{4}\right)\Delta\alpha \qquad (2.3)$$

$$F_{LW} = \sigma T_0^4\,\Delta g \qquad (2.4)$$

Changes in solar constant S are indeed purely external, but both albedo α and greenhouse factor g depend strongly on clouds and atmospheric water vapour. Since the water and energy cycles are closely coupled in the climate system, climate change (represented here by changes in T) necessarily entails potentially strong feedback by way of the water cycle, especially in atmospheric water vapour and clouds.

Over the past two centuries, significant accelerating changes in atmospheric concentrations of carbon dioxide, methane, and minor greenhouse gases are unquestionably the consequence of human activities. Increasing infrared opacity of the atmosphere due to these recent changes constitutes significant LW forcing. Similarly, increasing anthropogenic aerosols modifying albedo and its geographic distribution, contribute to SW forcing. Actual climate change depends on both forcing and feedback, but at this point we consider only the forcings.

2.2.2 Climate Change Forcing

Solar forcing – Computation of SW forcing corresponding to hypothetical solar luminosity changes is straightforward; a variation of 1% has been the accepted standard case. Precise measurements have been made outside the atmosphere only over the last two or three decades, revealing near constancy (11-year solar cycle variation of ±0.1%). Recent analyses suggest that slightly larger variations (still well below 1%) may have played a role in the warming observed between 1850 and 1950 (Stott et al., 2000).

Greenhouse forcing – In most cases, observed changes in TOA emitted LW and reflected SW fluxes include feedbacks as well as forcing. Computation of LW (greenhouse) forcing on the basis of observed or projected changes in greenhouse gas concentrations (CO_2, CH_4, etc.) is relatively straightforward (Hansen et al., 2000). Greenhouse climate change forcing, defined as LW forcing at the tropopause, is not directly observable from space. However, estimates of contributions of changes in minor greenhouse gases such as methane or the CFCs can be checked on the basis of observed changes in the infrared spectrum of the Earth (Harries et al., 2001). Expected effects (observed since at least 1975) are warming at the surface and in the lower troposphere, and cooling in the stratosphere.

Atmospheric short-wave forcing – Natural and anthropogenic aerosol variations affect the reflection of solar SW radiation to space. Estimates have been made of SW forcing due to stratospheric aerosols after the Pinatubo eruption (Stenchikov et al., 1998), and reconstructions exist for earlier eruptions (e.g. Robock, 2000). Such estimates are still uncertain, but they remain relatively straightforward because only additional scattering and absorption by the aerosols are involved, and because the aerosol distribution is fairly uniform over the Earth although changing over months and years. The expected (and observed) effect is one of warming in the stratosphere and cooling in the troposphere. Estimates of SW forcing due to anthropogenic aerosols in the troposphere are far more uncertain, for three reasons:

1) Because the most important tropospheric aerosols are produced in the atmosphere from precursor gases (sulphate aerosols from sulphur dioxide), and because their residence times are generally short (of the order of weeks rather than months or years), their geographic distribution is non-uniform. The associated global mean SW forcing depends on convolution of this geographical distribution with that of insolation, as well as on the radiative properties of the aerosols.

2) Direct radiative effects of anthropogenic aerosols depend both on their geographic distribution and on their radiative properties. Scattering and albedo enhancement (therefore cooling) dominate for sulphate aerosols produced as a result of burning sulphur-rich fossil fuels without 'scrubbing'. However, other anthropogenic aerosols (e.g. soot) can be strongly absorbing (warming the aerosol layer) while at the same time reducing SW flux to the surface (Satheesh and Ramanathan, 2000; Jacobson, 2001). The geographic distributions of the two families of aerosols are poorly known.

3) Finally, it is believed that indirect effects of anthropogenic aerosols, acting as cloud condensation nuclei and changing drop size (or ice crystal size) distributions in clouds, are in many cases much stronger perturbations of SW fluxes than are direct aerosol contributions to scattering and/or absorption of solar radiation. These indirect effects are counted as SW forcing in many climate change simulations. Aerosol SW forcing must be applied with its seasonal and geographic distribution, but which distribution is correct is not known.

2.2.3. Policy Implications of Forcing Uncertainties

Obviously, political, economic, and technological considerations render risky any projection of anthropogenic greenhouse gas and other emissions throughout the 21st century. However, even for a fixed scenario of anthropogenic greenhouse gas enrichment, projections of future anthropogenic radiative forcing remain uncertain, in particular because of the large uncertainties regarding the SW component. Thus, the highest value (6 K global warming by 2100), of the wide 1 to 6 K range of the most recent IPCC projections, corresponds in part to a scenario in which today's moderate warming, due to today's greenhouse forcing of a relatively sensitive climate model, is partly masked by negative SW forcing due to anthropogenic sulphate aerosols. An additional assumption is that tomorrow's SW forcing will return to zero as a result of globalisation of anti-pollution (SO_2 scrubbing) measures while greenhouse forcing continues to grow rapidly. However, the controversial 'alternative scenario' presented by Hansen et al. (2000), is in part based on the hypothesis that anthropogenic aerosol SW forcing due to fossil fuel burning will continue to offset most of the LW forcing due to increased CO_2.

The fact is that we do not know the size or even the sign of today's anthropogenic aerosol SW forcing over many regions of the globe. Our knowledge of aerosol and cloud properties is inadequate for reliable calculation of the likely evolution of indirect aerosol forcing for a given scenario of anthropogenic emissions. Improved understanding of aerosol–cloud–radiation interactions is essential to improve such projections and to inform properly those responsible for major policy decisions.

2.2.4 Feedbacks

Although the 1 to 6 K range of the latest IPCC global warming projections is due in part to uncertainty in the forcing projections, it also includes a range of uncertainty in climate sensitivity. For a given scenario of total radiative forcing F, the expected global warming (see Figure 2.1) depends on uncertain feedbacks, as do the geographical distributions of precipitation and runoff changes. With only thermal radiation feedback, considering that outgoing LW radiation is given by $(1\text{-}g)\sigma T^4$, radiative equilibrium can be restored by a first-order surface temperature change $\Delta T_1 = F/\lambda_0$, where the purely radiative inverse climate sensitivity λ_0 is given by:

$$\lambda_0 = 4(1 - g_0)\,\sigma T_0^3 = 3.3\ \mathrm{Wm^{-2}K^{-1}} \tag{2.5}$$

Note that for the 4 $\mathrm{Wm^{-2}}$ forcing corresponding to doubling of CO_2, ΔT_1 is only 1.2 K. In reality, with a change of climate state (summarised by a value of ΔT different from zero), additional changes $\Delta\alpha'$ and $\Delta g'$ appear in parameters α and g. In the framework of the zero-dimensional model shown here, inverse sensitivity $\lambda = F/\Delta T$ is then given by:

$$\frac{\lambda}{\lambda_0} = 1 - \frac{1}{4}\,\frac{d\ln\left[\dfrac{(1-\alpha)}{(1-g)}\right]}{d\ln T} \tag{2.6}$$

and the difference $(\lambda/\lambda_0 - 1)$ corresponds to the inclusion of feedbacks acting by way of the temperature dependence of albedo and greenhouse factors. Climate response ΔT can either be stronger or weaker than ΔT_0, depending on whether λ/λ_0 is smaller or greater than 1. For $\lambda < 0$, the model climate is unstable rather than simply more or less sensitive to forcing.

If atmospheric absolute humidity and thus greenhouse factor g (cf. Equation .2.6 above) do in fact increase with temperature T, climate sensitivity is amplified by a factor of order two or more. Although contested by Lindzen (1990) and Sun et al. (2001), most climate-modelling specialists consider the operation of positive water-vapour feedback to be well established. By contrast, all agree that cloud radiation feedback is extremely uncertain. Since clouds act on both SW and LW radiative fluxes, partial compensation of opposite effects makes even the sign of the net cloud radiative feedback uncertain. Although much has been learned since Arking's (1991) review of the question, the uncertainties remain as strong as ever.

Modern climate change simulations give global warming for CO_2 doubling ranging from 1.7 to 4.2 K (IPCC 2001). These numbers correspond to climate sensitivity ranging from 0.47 to 1.13 $\mathrm{K(Wm^{-2})^{-1}}$, i.e. an uncertainty of a factor 2.4 in the total feedback factor λ (Equation 2.6 above), much of it due to conflicting results on cloud feedback. This is apparent in Figure 2.6, which shows results of different GCMs for the change in the so-called cloud radiative forcing parameter CRF. Note that CRF is not a climate change forcing in the usual sense. It corresponds to a simulated experiment in which instantaneous radiative flux changes are calculated for clouds instantaneously rendered transparent in a climate model previously run to equilibrium with clouds reflecting, absorbing and emitting radiation (Fouquart et al., 1990). Observational estimates are based on radiative flux differences between clear-sky areas and the average all-sky situation (Ramanathan et al., 1989). Many of the models considered in AMIP yield CRF values in strong disagreement with one another and with the ERBE and ScaRaB observational estimates. Such disagreement casts doubt on model estimates of cloud radiation feedback, related to change of the CRF parameter. The models reproduce certain present-day climate parameters but not others, and there is strong evidence that the culprits are to be found in the cloud parameterisations (Cess et al., 1990, 1996).

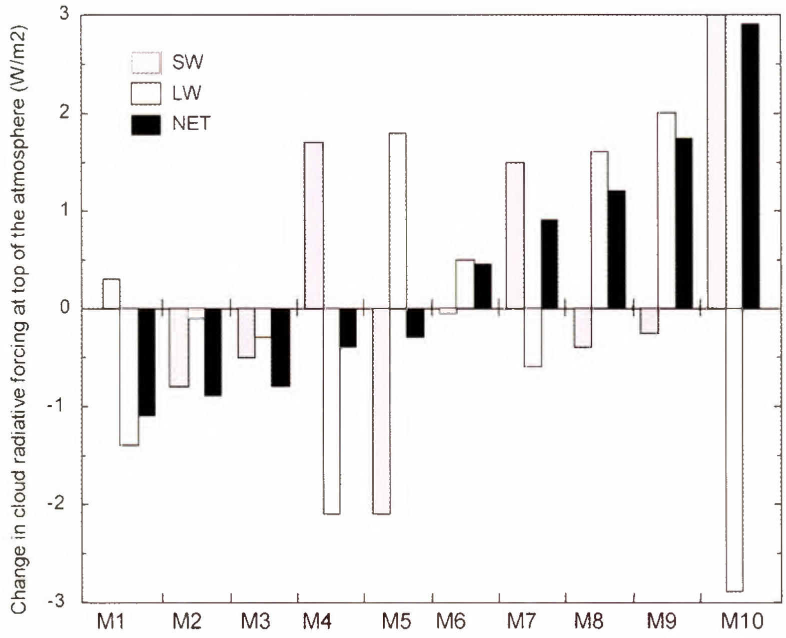

Figure 2.6: *Change in the Top of Atmosphere (TOA) Cloud Radiative Forcing (CRF) associated with a CO_2 doubling (from a review by Le Treut and McAvaney, 2000). Bars M1 to M10 correspond to ten different climate models.*

Senior and Mitchell (1993) demonstrated the important role played by ice clouds in feedback mechanisms associated with a doubling of CO_2 in a climate model. The inclusion of interactive radiative properties for ice clouds produces an overall negative feedback that reduces the global warming from 5.4 to 1.9 K. It counterbalances the positive feedback produced by the reduction of mid-level and low-level clouds. A modification of the treatment of ice sedimentation (based on observations) increases slightly the model sensitivity to 2.1 K. These results show the need for data on various aspects of cloud physics, including the ice phase, to reduce uncertainties associated with climate change predictions.

2.2.5 Relevant Existing and Planned Observations

Consideration of forcings and feedback generally proceeds on the basis of radiative fluxes at TOA (Equation 2.1). Systematic measurements of broadband SW and LW radiances for the determination of such TOA fluxes were made beginning with NASA's Nimbus/ERB and ERBE (Earth Radiation Budget Experiment) missions (House et al., 1986; Barkstrom et al., 1989; Wielicki et al., 1996), continuing with CERES and with the French-Russian-German ScaRaB (Scanner for Radiation Budget) missions (Kandel et al., 1998; Duvel et al. 2001). The CERES project also has the ambition to estimate SW and LW fluxes at the surface and at several levels in the atmosphere using synergetic analysis with the narrow-band, moderately high resolution MODIS data on board the EOS-Terra and EOS-Aqua platforms.

As an example, the OLR produced by the ECMWF model (12-hour forecasts) on 15 March 2001 is compared to the CERES instrument on board EOS-Terra in Figure 2.7. It is important to note that such a comparison, based on instantaneous model fields, is possible because this model is run within a continuous data assimilation cycle. Climate models are usually compared against monthly mean observations. Important positive biases up to 80 Wm^{-2} are noticed for high clouds associated with low OLR values. For observed values larger than 220 Wm^{-2}, the model has an overall negative bias around 5 Wm^{-2}. The associated standard deviation lies between 20 and 50 Wm^{-2}. The geographical distribution of these errors is shown in Figure 2.8 with large positive and negative biases (larger than 50 Wm^{-2}) in cloudy regions both along the ITCZ and over mid-latitudes.

Note that there has been continuing improvement of the bi-directional reflectance distribution (BRDF) functions used to convert observed SW radiances into estimates of reflected SW fluxes. BRDFs have been based in particular on the scanners with rotating azimuth of the scanning plane, which flew on Nimbus-7/ERB and also on ERBE (only occasional rotation of the scanning plane) and on CERES. Other information has come from analysis of the non-Sun-synchronous ScaRaB/Meteor data and of narrow-band measurements from geostationary satellites, providing a wide range of solar incidence angles. POLDER-ADEOS data provide original information on bi-directional reflectance and polarisation.

Broadband geostationary data are expected with GERB on MSG. The analysis will proceed in synergy with the narrow-band SEVIRI imagery.

Systematic determinations of the LW and SW cloud radiative forcing parameters, based on discrimination of clear-sky areas and estimation of clear-sky fluxes, began with ERBE

(Ramanathan et al., 1989) and have continued with ScaRaB and CERES. CRF estimates have also been made for the Nimbus-7 mission by combining the Nimbus-7/ERB and THIR and TOMS data.

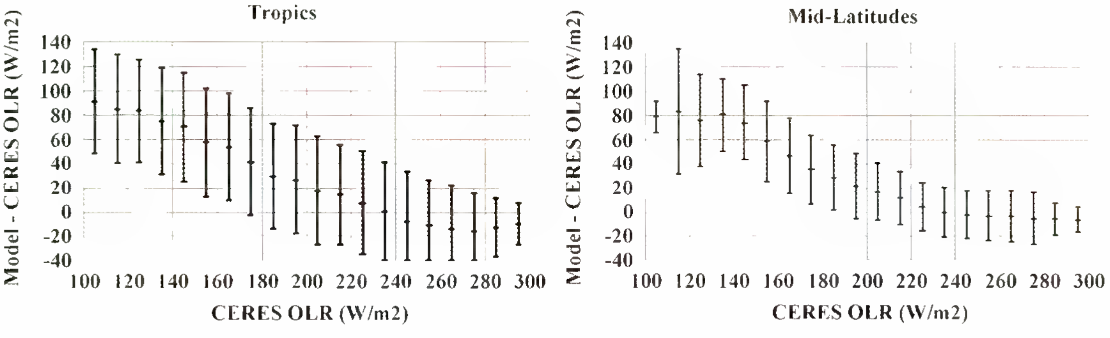

Figure 2.7: *Difference between the TOA long wave radiation (OLR) from the ECMWF model (short-range forecasts) and the corresponding CERES measurements (model-CERES) as a function of CERES observations for 15 March 2001. A distinction is made between tropical (20S-20N) and mid-latitudes. The fluxes are instantaneous values in Wm*$^{-2}$*. The squares and the vertical bars represent, respectively, the mean and the standard deviation in each histogram class. It should be noted that the model bias is of the same order of magnitude as the OLR itself for high clouds and ten times greater than the 10 Wm*$^{-2}$ *target of EarthCARE.*

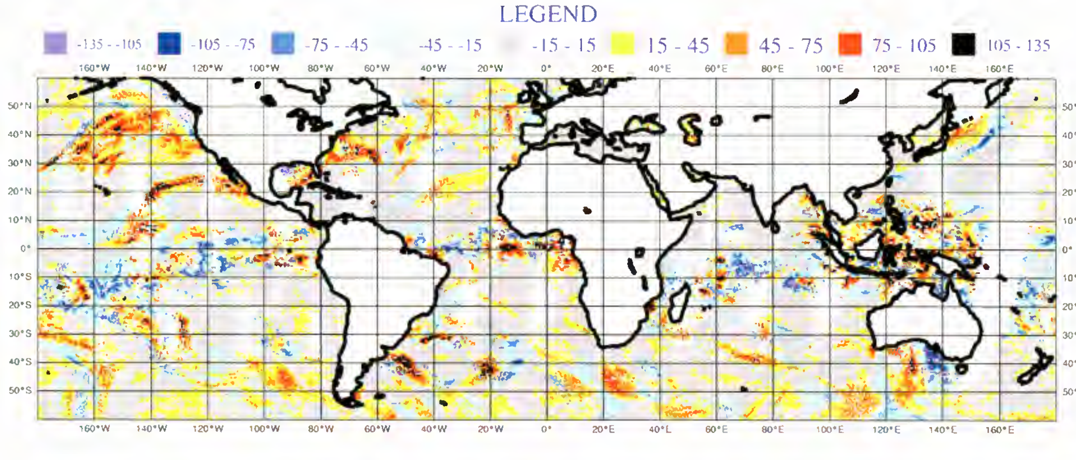

Figure 2.8: *Geographical distribution of differences between instantaneous OLR fluxes from the ECMWF model and those measured by CERES (EOS-Terra) for 15 March 2001 (units: Wm*$^{-2}$*). Differences exceeding the EarthCARE 10 Wm*$^{-2}$ *target accuracy occur over many regions.*

SSM/I radiometers on board DMSP satellites provide information on cloud liquid water through a set of microwave brightness temperatures between 19 and 85.5 GHz, but only over ocean. They are more effective than infra-red sensors at penetrating thick clouds. However, they only provide a vertically integrated quantity and retrievals are contaminated in the presence of rain.

The principal products of the International Satellite Cloud Climatology Project (ISCCP: Rossow and Schiffer, 1999) are cloud parameters based on narrow-band imagery from the operational geostationary and polar orbiting weather satellites, with inclusion of passive atmospheric sounding (TOVS) data (such as optical depth, effective radius, cloud top pressure or effective cloudiness). However, atmospheric physical properties are determined simultaneously, and broadband SW and LW all-sky and clear-sky fluxes can be and are computed at different levels from TOA to the surface (Schmetz, 1989). Accuracy of the in-atmosphere and surface data products derived from ISCCP data (presented in part as ISCCP products, in part as products of other GEWEX radiation projects) is of course limited by the passive character of the measurements, particularly for layers in and below (optically thick) clouds.

It must be emphasised that none of these data sources provides accurate vertical profiles of atmospheric and cloud properties within clouds.

CloudSat and ESSP3-CENA are relevant planned missions to be launched in early 2004. For their relation to EarthCARE,. see Section 3.1.

2.2.6 Concluding Remarks

Predictions of 21st century global warming range from 1.4 to 5.8 K. A part of this range is related to different social development assumptions (and consequently emission scenarios), but a large part of this range of uncertainty, as can be seen from the model range bars at the right of Figure 2.1, arises from the limited knowledge in atmospheric sciences, notably with regard to the interactions of clouds and aerosols with radiation. In addition, equally important predicted changes in the geographical distribution of fresh water have very large uncertainties resulting from gaps in our knowledge concerning cloud processes.

For an assumed anthropogenic emission scenario, calculated short-wave forcing depends critically on aerosol-cloud interactions, and validation of the simulations requires combined simultaneous collocated active and passive observations.

For a given forcing scenario, reliable prediction of climate change (both temperature and precipitation) requires a strong reduction of the uncertainty in cloud feedback, and this can only be done with validated representations of cloud–water–ice processes. Such validation is not possible with presently existing or near-term-planned observations. EarthCARE will provide the needed datasets.

2.3 Representation of Clouds and Aerosols in NWP and Climate Models

The Problem

Clouds and aerosols are responsible for much of the uncertainty in projections of global warming and of changes in the geographical distribution of precipitation, but their representation in General Circulation Models (GCMs) used for weather and climate predictions is a difficult exercise because clouds encompass a broad spectrum of scales, from the very small ones describing microphysical processes, to planetary scales describing cloud organisation in large systems (frontal bands, inter-tropical convergence zone, easterly waves, ...), and the details of their interactions with aerosols are unknown. GCMs can explicitly describe atmospheric motions having horizontal scales larger than a few hundred kilometres and vertical scales of about one kilometre.

Current operational forecasting models have a global horizontal grid scale of 30–50 km while those used for long runs simulating future climate scenarios are limited to 100–250 km. It will never be possible to represent individual clouds in such models, and global numerical models will never explicitly resolve important physical processes describing the formation and dissipation of clouds. These processes are implicitly accounted for through parameterisation schemes, which represent the effect of sub-grid scale processes on resolved model scales. The parameterisation of sub-grid scale processes is a key issue of both climate and NWP models. It is only during the past decade that clouds have been represented in global models by explicit prognostic variables rather than being diagnosed from other variables such as humidity. For example, at each grid box at each vertical level in the ECMWF model the effect of clouds is represented by two prognostic variables, fractional cloud cover and mean water content (in gm^{-3}).

The phase of the clouds (liquid or ice) is currently diagnosed as a monotonic function of the temperature. Other models diagnose fractional cloud cover, but have two separate prognostic variables for ice and liquid water content. Aerosol characteristics (spatial distribution, optical properties) are currently prescribed. This treatment is very simplistic, but the inclusion of the new cloud variables has had a very positive effect on the reliability of model predictions. However, there is no vertically resolved cloud data to validate whether the model representations are correctly simulating reality. The goal of EarthCARE is to provide such validation data so that the representation of clouds and aerosols in current climate models can be evaluated on a global scale and then improved.

The Role of Clouds

As explained in detail previously, it is essential to describe clouds correctly in climate and NWP models because the response of GCMs to climate changes is extremely sensitive to cloud description. Clouds also influence the atmosphere on shorter time scales. The skill of short- and medium-range forecasts of weather parameters such as precipitation, air temperature and cloudiness strongly depends upon the ability of NWP models to correctly describe cloud elements (Jakob, 1995).

Critical Parameters

Clouds influence both the radiative and hydrological budgets of the atmosphere. The description of radiative effects is based on the knowledge of cloud fraction and cloud liquid and ice water contents. However, in early GCMs, radiative effects were treated separately from moist processes. The reason was that parameterisation schemes for moist processes (grid-scale condensation and cumulus convection) did not assume any cloud stage (all condensed water was instantaneously removed as precipitation). Cloud cover was diagnosed from relative humidity and other large-scale parameters (static stability for low-level clouds, intensity of convective precipitation for cover by convective towers and associated anvils, vertical velocity) as in Slingo (1980). These schemes defined a critical relative humidity vertical profile above which cloud formation occurs. Cloud liquid water was also diagnosed empirically from temperature and humidity profiles using simple assumptions.

Bulk Microphysical Prognostic Variables

In the past decade, cloud water (or total water) has been introduced as an additional prognostic variable in GCMs. This approach provides a proper representation of the thermodynamical effects of sub-grid condensation and a better link between radiative, dynamical and hydrological processes, particularly when cloud radiative properties are linked to the prognosis cloud water. These schemes account explicitly for the physical sources and sinks leading to the production and dissipation of clouds (radiation, vertical motion, turbulence, deep and shallow convection). Such formulations require some description of bulk microphysics in order to account for the conversion of cloud water into rainwater through coalescence, accretion and collection processes. The microphysics can only be expressed in terms of volume-averaged condensation parameters, since the drop size distribution (DSD) of cloud and rain particles cannot be explicitly treated in large-scale models. The main principles of bulk microphysics have been described by Kessler (1969). The condensation process is assumed to occur at 100% relative humidity. The release of precipitation from cloud liquid water is commonly described by the auto-conversion formulation of Sundqvist (1978) and by a sedimentation process for cloud ice water that requires the specification of an icefall terminal velocity (Heymsfield and Donner, 1990). By imposing a statistical distribution of temperature and moisture within a model grid box, it is possible to diagnose fractional cloudiness. The shape of the distribution can depend upon environmental parameters such as turbulent fluxes (Sommeria and Deardorff, 1977), saturation specific humidity (Smith, 1990) or deep convection (Tompkins, 2001). Other schemes such as the one at ECMWF (Tiedtke, 1993) have an additional prognostic variable for cloud fraction. Since liquid water and cloud fraction are only bulk macro-scale quantities, the particle size spectrum is also necessary to derive radiative properties such as the optical thickness, the asymmetry factor or the single scattering albedo. The spectrum is generally specified by imposing the effective radius of the particles either as a constant number or with some dependency upon environmental parameters (Ou and Liou, 1995; for ice particles) or cloud type (Stephens, 1978; Stephens et al., 1984).

Cloud Overlap and Inhomogeneities

In terms of macro-scale properties, the fractional cloud cover within each model grid-box requires assumptions about how model cloud layers overlap on the vertical (currently clouds are assumed to fill the whole grid-box on the vertical). The standard overlap assumption is the 'maximum-random', which assumes a maximum overlap of adjacent cloud layers and a random overlap when cloud layers are discontinuous (Geleyn and Hollingsworth, 1979). The study of Morcrette and Jakob (2000) has shown that model results are sensitive to overlap assumptions for the vertical profiles of radiative fluxes and the evaporation of precipitation. Recent radar data have shown that for some meteorological situations (mid-latitude frontal regimes) the maximum-random overlap assumption can be questionable (Hogan and Illingworth, 2000). Currently, most GCMs, assume homogeneous properties within the cloudy fraction of each model grid-box (homogeneous plane parallel assumption for solving the radiative transfer equation). Various simple empirical corrections have been defined to account for spatial heterogeneities of cloud liquid water in the radiative transfer computations (e.g. Tiedtke, 1996).

Aerosols

When included in NWP models, aerosols are described rather crudely. This is due to the wide diversity of aerosol types and because they have a minor direct effect on instantaneous radiative fluxes. Tanré et al. (1984) proposed a climatological classification of aerosols in five types (stratospheric, volcanic, urban, desert, maritime). For each type, a fixed three-dimensional distribution is prescribed with associated optical properties (Hess et al., 1998). This approach allows the atmosphere to be modified by aerosols through their effect on radiation, but there are no feedback mechanisms. In some climate models (Feichter, 2000), aerosols are represented in a more realistic way. They can be transported by the dynamics and turbulent processes (in the boundary layer and in cumulus clouds). Some of the sources and sinks associated with chemical reactions and cloud interactions (wet deposition, cloud condensation nuclei…) can also be described. These processes are important to include in climate change predictions, since anthropogenic aerosols might play a significant role in global warming

In summary, current GCMs represent clouds at each grid box at each vertical height by prognostic variables such as fractional cloud cover, average ice water content and

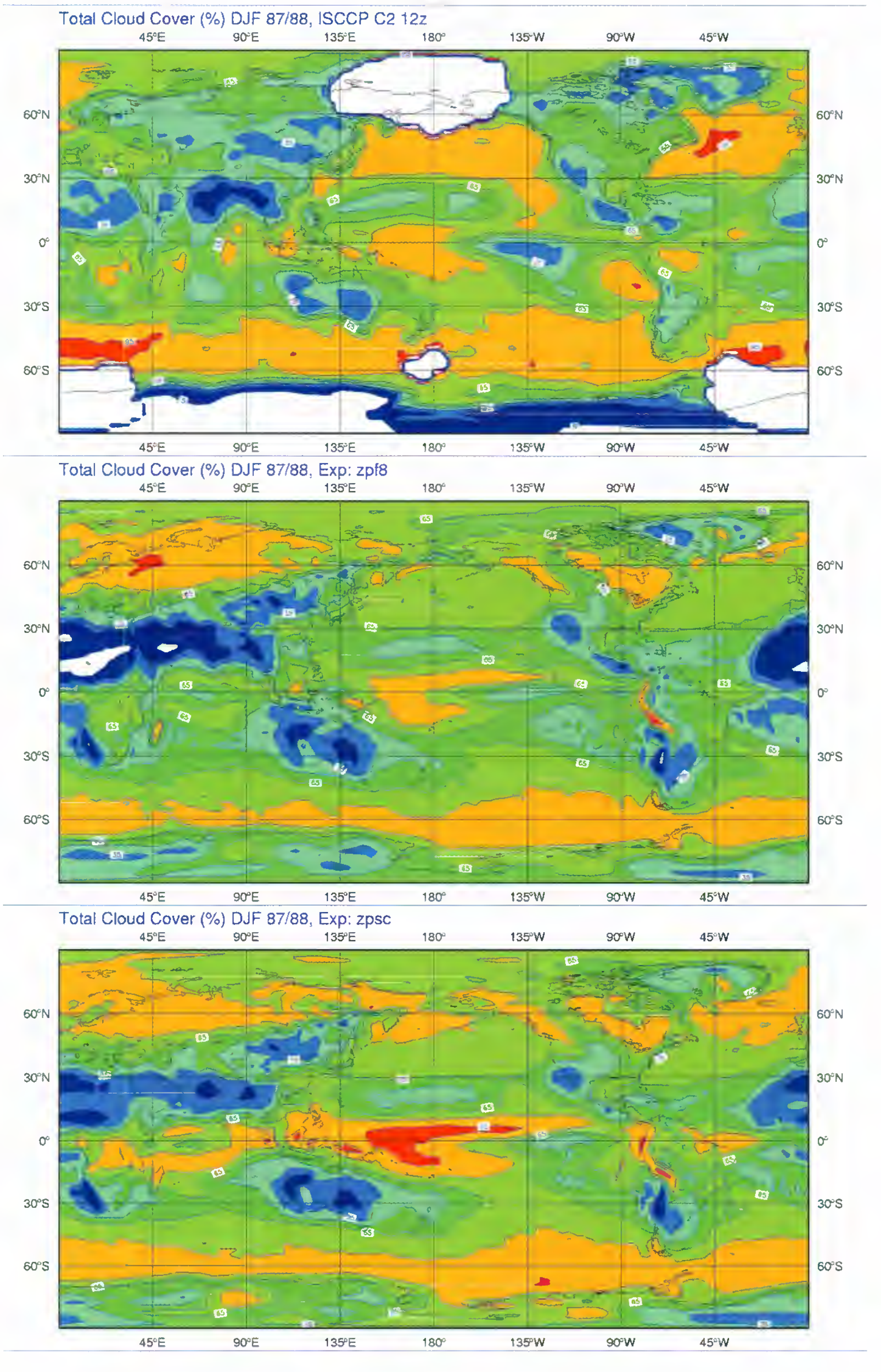

Figure 2.9: *Total cloud cover (%) for December/January/February 1987-88 from T63L31 model simulations: ISCCP climatology (upper) and two different model physics. Contours are 5, 20, 35, 50, 65, 80 and 95% (Janiskova, 2001). Note the major differences over the tropics.*

average liquid water content, whereas parameters such as aerosol characteristics and vertical cloud overlap are presently prescribed. Figure 2.9 shows an example of the significantly different fractional cloud covers (in terms of seasonal mean) that can be obtained from slightly different cloud model physics (changes to cloud ice properties, treatment of cloud inhomogeneities and modified closure for the convection scheme). For reference, the ISCCP climatology is also shown for the same season.

The effect that crucial sub-grid scale and microphysical processes have on model prognostic variables have to be represented through parametrisation schemes. Examples are:

1) Production and dissipation of clouds (radiation, vertical motion, turbulence, deep and shallow convection, precipitation)
2) Cloud overlap assumption and its effect on radiation and production of precipitation.
3) Radiation and its dependence on cloud phase and particle size via optical depth, phase function and effective radius.
4) Cloud particle size spectra and their effect on sedimentation, cloud lifetime and production of precipitation.
5) Glaciation, super-cooled clouds, aggregation and riming of ice crystals to produce snow, graupel and hail.
6) Effects of aerosols on condensation of clouds, nucleation to produce ice, rain production and cloud lifetime.
7) Explicit representation of natural and anthropogenic aerosols through sources, transport processes and sinks.

At present, no vertically resolved global observations of clouds and aerosols are available to validate the representation of clouds and aerosols in current models. There is some limited information on integrated liquid water path but our knowledge of vertical profiles, in particular for ice water content and aerosol loading, and their vertical variation is virtually zero. Only when such data are available can current models be adequately evaluated and the parameterisation schemes further developed and improved.

2.4 EarthCARE Contribution

The Problem

The problem with evaluating current cloud, aerosol and radiation parameterisations is the large ambiguity in the source of the model errors in radiances and/or broadband flux densities. Radiative effects of clouds and aerosols depend on a number of different parameters, such as:

i) macroscopic cloud structure (cloud top height, cloud base, cloud fraction, cloud overlap – including horizontal cloud inhomogeneity on the sub-grid scale)

ii) cloud condensate content (ice and liquid water content)

iii) cloud micro-physical structure (effective radius, phase of condensate, particle shape)

iv) aerosol parameters important for direct and indirect forcings (optical depths, particle size and composition).

As demonstrated in Figure 2.2 the AMIP survey of the models currently used for predicting climate had mean levels of integrated water content which varied by an order of magnitude, even though these models were able to produce comparable top of the atmosphere fluxes. There is clearly an urgent need to provide data on the vertical structure of ice and liquid water content on a global scale to resolve the enormous discrepancy between different models. This applies also to aerosols, as shown in Figure 2.4.

The Need

In summary, it is crucial to simultaneously measure as many of these parameters as possible in a 'radiatively consistent' manner. This means that the observational requirements for all the above parameters should all be derived from the same radiative flux accuracy. In EarthCARE an instantaneous radiative flux accuracy of 10 Wm^{-2} is used.

The cloud parameterisations are not only relevant for the radiative budget, but also for relevant atmospheric processes within the energy and water cycle such as the onset of precipitation and the run-off (Chahine, 1992) which play an important role in the hydrological cycle

The Solution

EarthCARE will, for the first time, provide vertical profiles of clouds and aerosols measured by active radar and lidar mounted together with an IR Fourier Transform Spectrometer and other passive instruments on the same satellite. These profiles can only be obtained from active instruments and are unavailable from existing passive cloud satellite observations. This will enable us to carry out a global analysis of the performance of climate and NWP models. The envisaged scope of work is provided by the following examples.

i) Lidar analysis from the LITE mission in 1994

Figure 2.10, from Mahfouf et al. (1999), shows the vertical profile of cloud cover as detected from the lidar flown on board the shuttle in 1994 for one part of an orbit and compares it with the cloud cover held in the ECMWF operational model at that time. The LITE (Lidar In-space Technology Experiment) data were binned to both the vertical and horizontal of the model grid. Qualitatively, the vertical extent and placement of deep convective systems in the ITCZ, mid-latitude disturbances, and large scale subsidence areas appear to be in good agreement with the observations for this case. This shows that despite the small footprint of the lidar instrument compared to the model grid size (60 km), such a comparison is relevant. The analysis of 15 orbits has revealed a possible underestimation of the frequency of high altitude cirrus and an overestimation of lower tropospheric clouds by the ECMWF model.

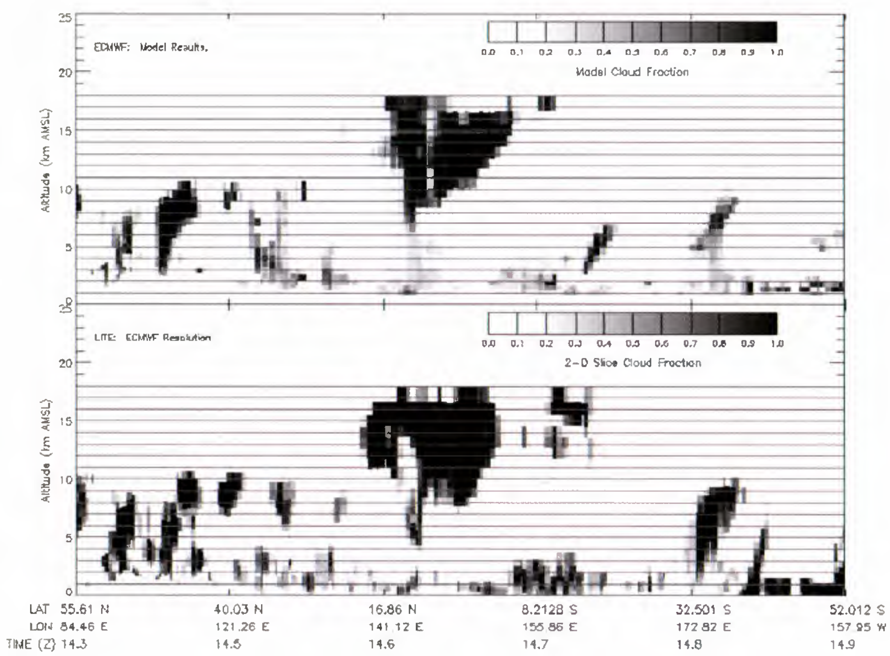

Figure 2.10: *Vertical cross section of cloud fraction from an ECMWF short-range forecast (top panel) and from the Lidar In-space Technology Experiment (LITE) (bottom panel). The chosen orbit (16 September 1994, 14:25-15:00 UTC) spans the Western Pacific warm pool. Note that the ECMWF model seems to have too much high cloud.*

ii) Validation of fractional cloud cover in the operational models from measurements at a single ground station

The vertical profile of fractional cloud cover observed each hour for the month of December 1999 over Chilbolton in the UK is compared with the value held for that hour in two operational models, those of ECMWF and the UK Met Office and the results are displayed in Figure 2.11. The grey stripes in the record of the observed cloud fraction indicate that no data was obtained because the radar at Chilbolton was scanning in an off-zenith direction, but we can see that both models predict the fractional cloud cover with some skill. However, it is clear that the UK Met Office model generally indicates a lower cloud fraction than that of ECMWF. Comparisons of the observed mean cloud fraction and the ECMWF values for that grid box over a three-month period (Hogan et al., 2001) are displayed in Figure 2.12 and reveal some biases in the model representation: once light snow is reclassified as cloud in the model, the observed average frequency of some cloud cover as a function of height agrees well with the model frequency, but the mean cloud fraction amount when cloud is present in the model seems to be too large for heights above 6 km. Clearly a satellite would be able to provide such validation over the whole globe rather than at just one grid point.

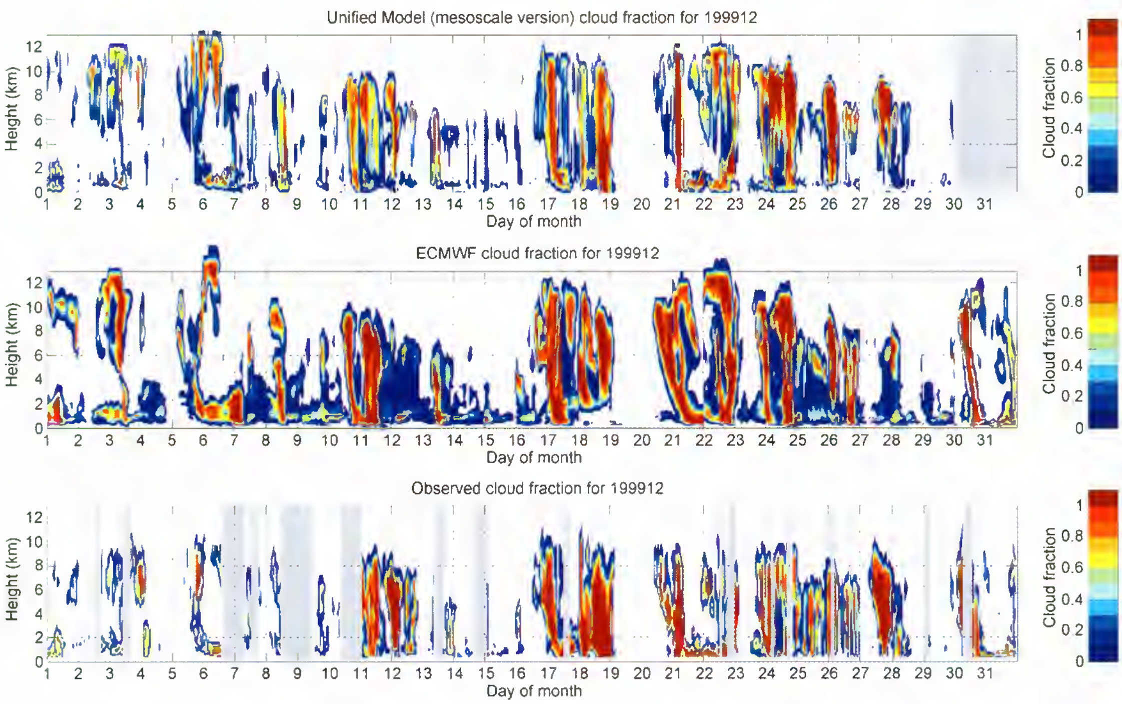

Figure 2.11: *Vertical profiles of fractional cloud cover for a one-month period. The lower panel shows the observations at Chilbolton, UK. The upper and middle panels show respectively the values for the same grid-box for the operational models of the UK Met Office and the ECMWF.*

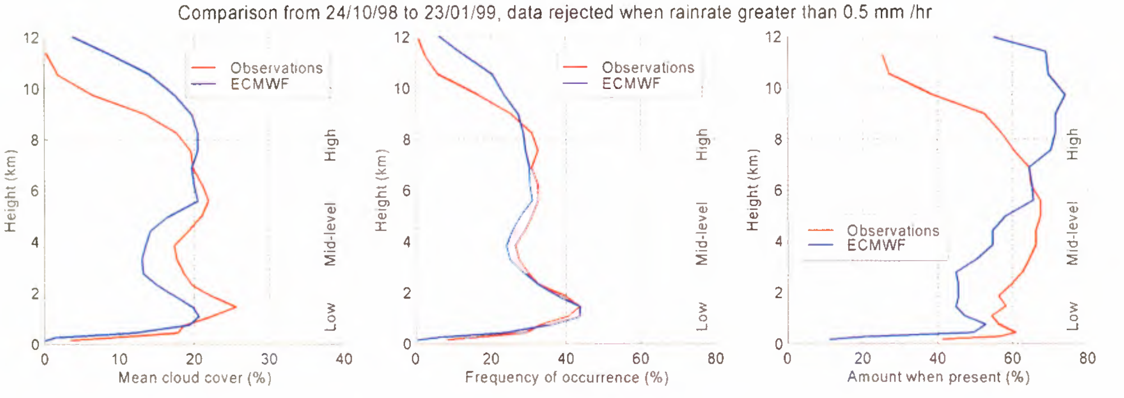

Figure 2.12: *Three-month comparisons of the mean profile of cloud fraction observed at Chilbolton and ECMWF (from Hogan et al., 2001). Note that the frequency of occurrence of cloud is well forecast by the model, but (in contrast to Figure 2.10) the measured amount of cloud when present is higher than the model below 6 km and lower above that height.*

iii) Validation of cloud overlap

When each level of a vertical stack of grid boxes is partially filled with cloud, the way in which the cloud overlap is represented is known to have a marked influence on both the radiative balance and the efficiency with which precipitation is produced. Figure 2.13 shows three possible ways in which the overlap could be represented: random, maximum and maximum-random. Most models use maximum-random, in which the overlap for vertically continuous layers is assumed to be maximum, but the overlap between the vertically continuous layers separated by cloud free layers is random. Analysis of a series of ground based data in the UK by Hogan and Illingworth (2000) in Figure 2.14 reveals that layers separated by cloud free regions are indeed randomly overlapped, but the overlap for vertically continuous cloud is only maximum for short vertical separations, and once the cloud layers are separated by more than 2 km the overlap is essentially random. The implications of this finding are currently being explored by ECMWF. Clearly, the amount of shear may be higher in the mid-latitudes, so satellite data are needed to provide a global measure of how clouds overlap on a global scale.

iv) Supercooled clouds

Figure 2.15 shows how supercooled clouds can be identified from simultaneous radar and lidar observations; the supercooled clouds contain many small liquid cloud droplets and are clearly distinguished by their very high lidar backscatter and extinction, whereas the small cloud droplets make negligible contribution to the radar echo. Hogan and Illingworth (2000) have shown from an analysis (Figure 2.16) of three years of cloud radar and lidar data over Southern England that such supercooled layers are very common in mid-level clouds, and occur on 30% of occasions when there is some cloud around -10°C. Supercooled layers have a significant radiative impact and

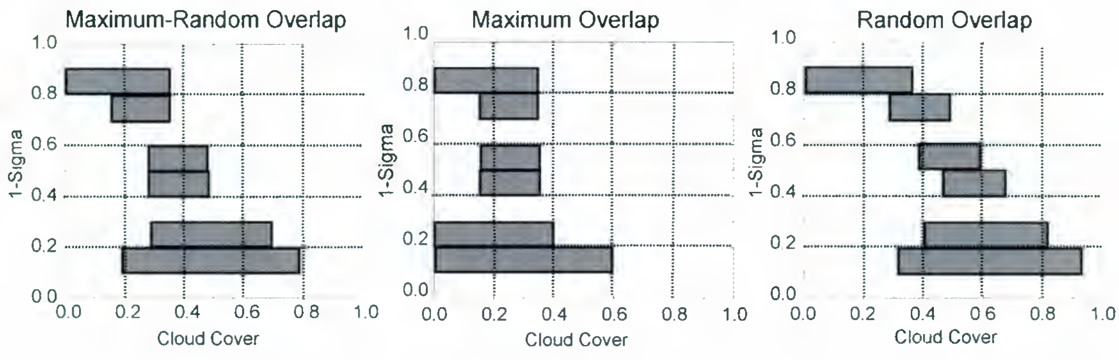

Figure 2.13: *Cloud overlap assumptions. Maximum-random overlap is usually assumed in NWP.*

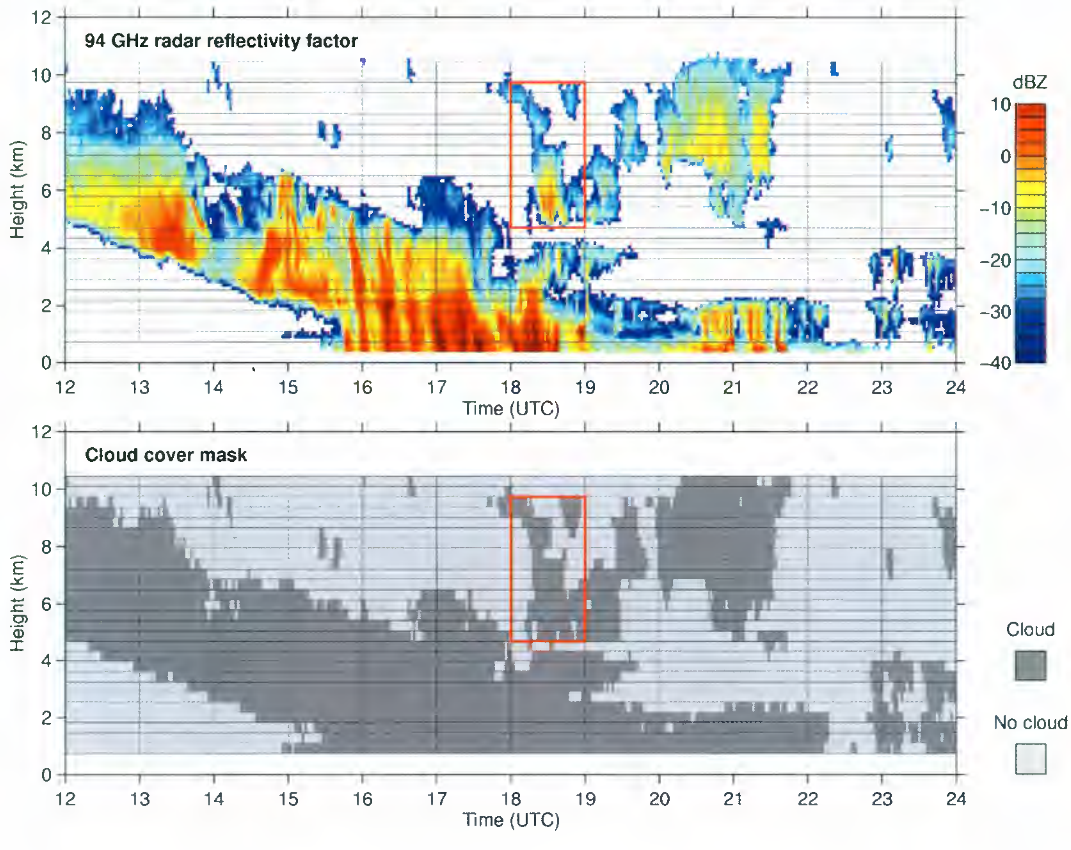

Figure 2.14: *An example of how fractional cloud cover is derived from radar observations on 11 December 1998 for comparison with the hourly values held in the ECMWF model. Note how the continuous cloud cover within the red box becomes randomly overlapped as the vertical separation of the layers increases.*

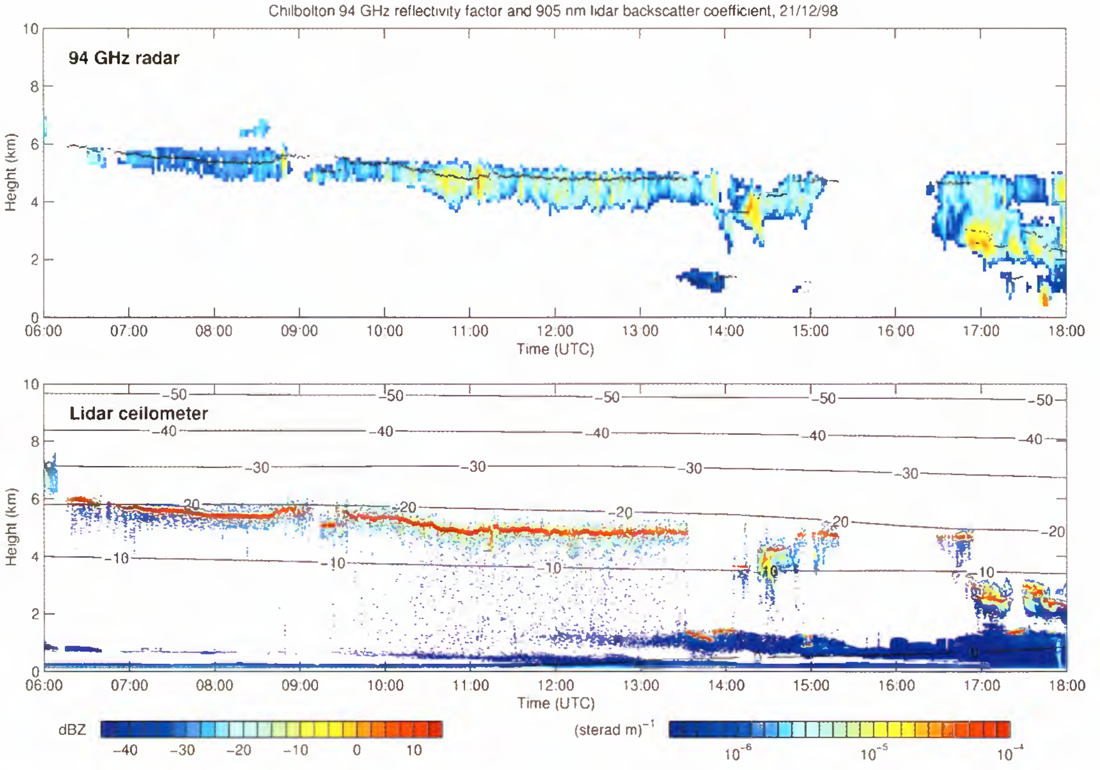

Figure 2.15: *Synergy of ground-based radar and lidar reveals a layer of super-cooled droplets at a height of 5–6 km. The lidar return in the lower panel shows some aerosol in the lowest kilometre, and a highly reflecting and attenuating layer with* $\beta > 5\times10^{-5}\ m^{-1}\ sr^{-1}$ *from super-cooled liquid cloud droplets. The small super-cooled droplets give a negligible radar return, but the outline of the high b region embedded in the ice-cloud has been superposed in black on the radar picture.*

are also important in the production of precipitation. Current models fail to represent them at all. Again a satellite mission will provide global statistics of their occurrence.

v) Retrieval of ice crystal size

A new synergetic radar and lidar inversion procedure (see Section 5.8) has been developed to derive cloud particle effective radius and ice water content. The algorithm uses the radar reflectivity and an effective particle size to parameterise the extinction at the lidar wavelength while treating the derived sizes and lidar multiple scattering effects in a consistent fashion.

The method is specifically suited for the study of ice-clouds. The algorithm has been applied to five months of data from the Southern Great Plains ARM site (Donovan and Van Lammeren, 2001a) and provides, for the first time, data on the variation of effective radius of ice particles with temperature.

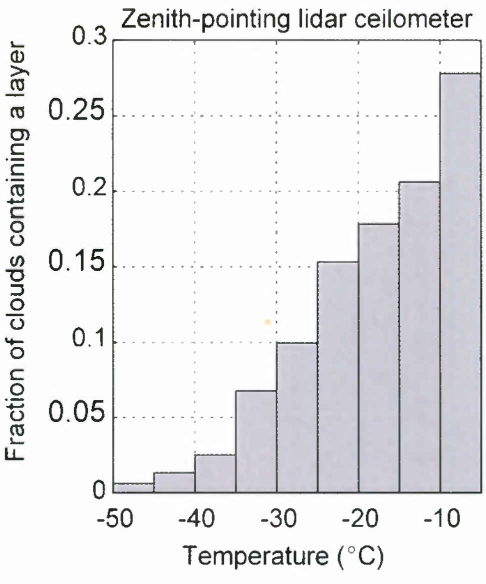

Figure 2.16: *Statistics of the frequency of occurrence of super-cooled layers within clouds as a function of temperature for 1025 days at Chilbolton, UK. From space such data would be available globally.*

The observed relationship between effective ice-particle size and temperature is presented in Figure 2.17. From the depicted R'_{eff} the normal effective radius can be derived using assumptions on the ice particle habit. At present these relationships could be derived only for a very limited number of observational sites, which produce 'long time series' of collocated lidar and radar observations. EarthCARE will provide a global data set of this type of observation.

vi) Aerosols

Aerosols have been measured comprehensively in several recent regional experiments such as TARFOX, INDOEX, SAFARI and ACE-Asia. The observations have shown that extensive aerosol layers are generated from industrial sources and biomass burning. Figure 2.18 shows an example of the detailed vertical structure observed by airborne lidar over the Indian Ocean during INDOEX. Note the aerosols extending up to 2.5 km above the marine boundary, due to monsoon transport far from the sources. These aerosols have a strong impact on the regional radiative budget in the order of -20 Wm^{-2} (Satheesh and Ramanathan, 2000). Combination of the satellite-borne lidar and imager will depict the three-dimensional global distribution of aerosols. Furthermore, the lidar can provide a detailed distribution of aerosols over land areas, which is difficult from passive sensors. Such information can be used for deriving the direct radiative forcing of aerosols over land from radiances measured by imagers, as well as for validating the aerosol chemical transport model simulation, especially over land, as shown in Figure 2.5.

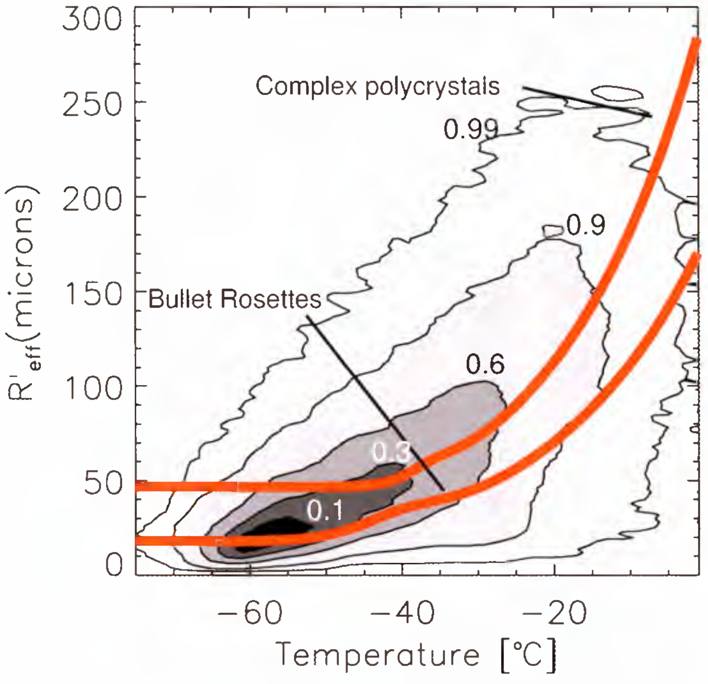

Figure 2.17: *Density plot (normalised to 1.0) of probability of occurrence of R'_{eff} as a function of temperature for five months of observations from the SGP ARM site. The two overlaid lines are taken from the parameterisation scheme described by Kristjansson et al. (2000).*

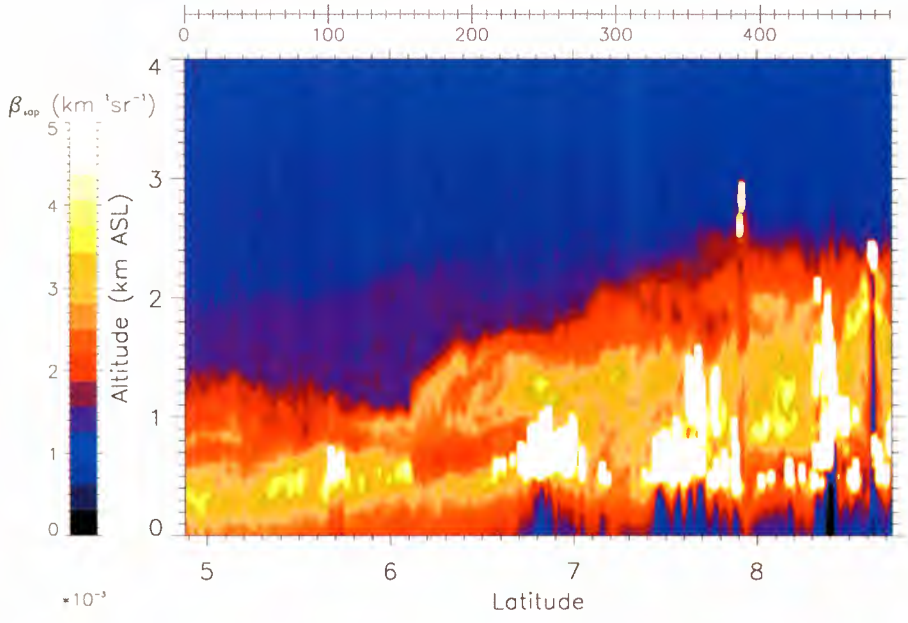

Figure 2.18: *Vertical backscatter profiles from aerosols obtained by airborne lidar (LEANDRE) during INDOEX.*

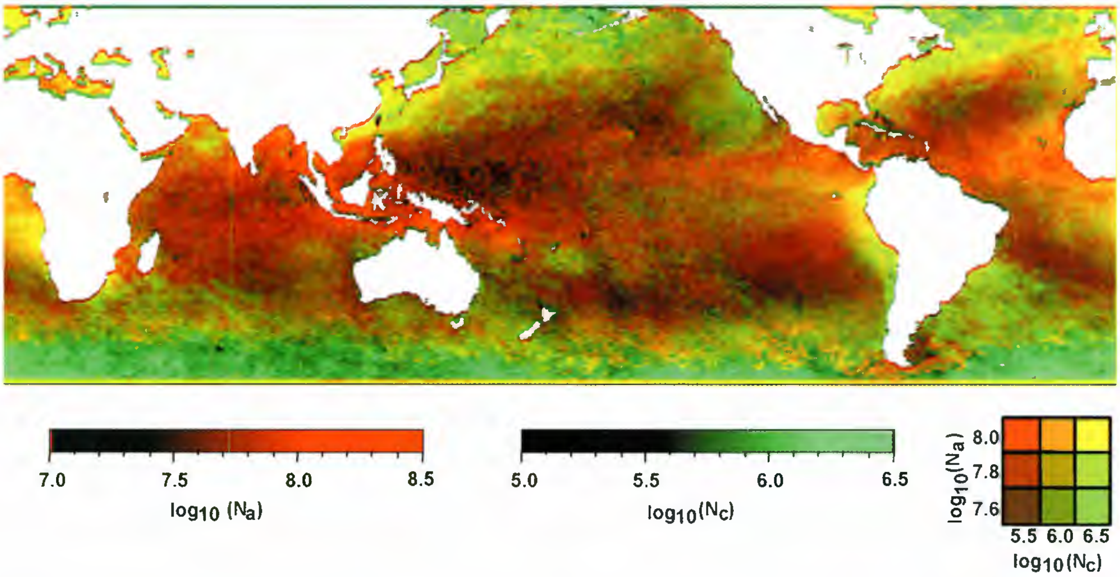

Figure 2.19: *Global map of the correlation between the column aerosol number (particles cm^{-2}) and that of low cloud particles. There are three types of correlation: significantly strong (green), strong (yellow), and weak (red), depending on the cloud formation process. The radiative forcing corresponding to the indirect aerosol effect is difficult to assess unless observation of the cloud vertical structure makes cloud classification possible.*

vii) Evaluation of the aerosol–cloud interaction

The largest uncertainty in the anthropogenic climate forcing in the next 100 years is the radiative forcing due to cloud change caused by aerosols acting as cloud condensation nuclei. Satellite remote sensing has shown that there is a characteristic correlation between cloud particle size and aerosol concentration (Han et al., 1994; Wetzel and Stowe, 1999). Nakajima et al. (2001) compared the column aerosol number and the low cloud particle number (Figure 2.19) to estimate the radiative forcing of aerosol indirect effect from -0.7 Wm^{-2} to -1.7 Wm^{-2} averaged globally over ocean. Such knowledge has to be validated by more direct measurements of aerosols and clouds with active remote sensors. The combination of lidar and CPR observation gives us a capability for vertical sounding of cloud particle size as well as aerosol concentration. This information is especially important to combine with the two dimensional horizontal distributions as in Figure 2.19 for generating the three dimensional structure of aerosol and cloud parameters relevant for evaluating the aerosol–cloud interaction strength.

Use of EarthCARE data

Using the above examples (i to vii) as a guide, we can envisage comparing numerical models with satellite data in several ways. The aim of such comparisons will be to identify model biases in the representation of clouds and radiation, to understand the origin of these biases, and then improve the parameterisation schemes in order to reduce them as much as possible. The satellite data will be used for process studies over a large range of different climate regimes so that a better understanding of the basic physics will lead to more realistic parameterisation schemes. EarthCARE will provide valuable observations for improving the description of cloud sub-grid scale variability (including cloud overlap assumptions) and cloud microphysical properties (such as the definition of particle size and ice sedimentation).

a. *Global model evaluation*

The observations will provide global statistics of profiles of cloud cover, ice and liquid water content, cloud particle size, cloud overlap, and aerosol optical depth as indicated in Figures 2.10 to 2.18. A traditional climatological approach will be to compare the mean values with those held in climate and NWP models. This technique is adopted when using the mean outgoing long wave radiation measured by satellite at TOA to constrain and validate the earth radiation budget of current global circulation models. A TOA constraint is powerful, but of course not unique because the same TOA radiation can correspond to many different vertical profiles. A logical extension is to compare the frequency distribution of the profiles of the variables with the distribution in the models.

b. *Classification by weather regime*

Another approach is to classify the observational data into different weather regimes – such as tropical cirrus anvils and mid-latitude depressions – and compare the observations for each regime at different stages in any evolution it undergoes, with the representation of the particular regime within the weather forecasting and climate models.

c. *Snapshot approach*

Finally, one can adopt the snapshot technique whereby the instantaneous state of the atmosphere is compared with the model representation within an operational weather forecasting system at that time as shown in Figures 2.10 and 2.11. Such an operational forecasting system should assimilate observations on clouds and radiation, as explained below.

d. *Data assimilation*

Modern data assimilation techniques optimally combine different types of observational data (e.g. radiosondes and satellites) with an operational numerical model, to produce the best possible description of the state of the atmosphere. Accordingly, the best approach would be to assimilate the instantaneous vertical cross-sections of the actual three-dimensional structure of clouds provided by EarthCARE. Current techniques assimilate only cloud free radiances at TOA (e.g.

TOVS), sondes and surface observations, but recent advances mean that in the foreseeable future it will be possible to assimilate observations on clouds and in particular EarthCARE products. Atmospheric analyses including EarthCARE data should be used to validate climate models, since they will be the most reliable space-time description of cloud properties on the global scale. The systematic comparison of EarthCARE products with short-range model forecasts will lead to improved specification of forecast error for cloud variables. This in turn will improve the data assimilation system. A better description of the model initial state using EarthCARE observations will also lead to better medium-range forecasts. Research studies on the use of real-time satellite data on limited aspects of cloud properties and rainy areas have already started at various operational centres with promising results. These studies will lead to a proper methodology for the inclusion of the more useful cloud profile information provided by the EarthCARE instruments in advanced data assimilation systems.

2.5 Conclusions

The difficulty of representing clouds and aerosols, and their interactions with radiation, constitutes a major source of uncertainty in predictions of climate change using numerical models of the atmospheric circulation. Accurate representation of cloud processes is also critical for improvement of numerical weather prediction. A first step in gaining confidence in such predictions is to check that these models are at least representing the clouds and aerosols correctly in the present climate.

Unfortunately, there are no global datasets, providing, simultaneously, the vertical profiles of clouds and aerosol characteristics together with vertical temperature and humidity profiles and the TOA radiance. Such datasets are crucial to validate the model parameterisations of cloud processes regarding both water and energy fluxes. The vertical profiles are important in controlling the radiative transfer processes in the atmosphere, and so affect the heating profiles, which then influence the dynamics.

Limited observations from airborne and ground based cloud radar and lidar have demonstrated that these instruments can penetrate clouds and so provide information on the vertical profile of clouds and aerosols, which has given some insight into the performance of models. The EarthCARE instrument complement will have the unique ability to provide global information on the profiles of clouds and aerosols in a radiatively consistent manner. Such data will be used to evaluate the performance of current models on a global scale, to improve their parameterisation schemes and thus provide better and more reliable climate predictions and weather forecasts.

3 Research Objectives of EarthCARE

EarthCARE has been specifically defined with the scientific objectives of determining for the first time, in a radiatively consistent manner, the global distribution of vertical profiles of cloud and aerosol field characteristics, to provide basic essential input data for numerical modelling and global studies of:

- the divergence of radiative energy
- the aerosol–cloud–radiation interaction
- the vertical distribution of water and ice and their transport by clouds
- the vertical cloud field overlap and cloud-precipitation interactions

The problem with evaluating current cloud, aerosol and radiation parameterisations is the large ambiguity in the source of the model errors in radiances and/or broadband fluxes. Radiative effects of clouds and aerosols depend on a number of different parameters, including:

i) macroscopic cloud structure (cloud top height, cloud base, cloud fraction, cloud overlap – including horizontal cloud inhomogeneity on the sub-grid scale),

ii) cloud condensate content (ice and liquid water content) and

iii) cloud micro-physical structure (effective radius, phase of condensate, particle shape),

iv) aerosol parameters important for direct and indirect forcing (optical depths, particle size and composition)

To achieve these objectives, it is crucial to measure in a 'radiatively consistent' manner as many of these parameters as possible for a global sample of clouds and aerosols, to link model errors in radiative quantities to cloud parameterisation errors.

3.1 Related Planned Missions

At present most of the cloud and aerosol parameters are derived from passive instruments. Crude assumptions are made to derive these properties. Almost no direct information on the vertical structure of clouds and aerosol fields is available.

In recent years the space agencies of the USA (NASA), Japan (NASDA) and Europe (ESA) have developed plans for satellites carrying active remote sensing instruments like radar and lidar for cloud observations. Japanese, European and Canadian scientists, supported by NASDA and ESA, have decided to join forces and now jointly propose the EarthCARE mission described in this report. It will fly, on a single platform, a lidar and radar together with a suite of passive instruments (Multi-Spectral Imager, Broad-Band Radiometer and Fourier Transform Spectrometer.

CloudSat

NASA and its partners have planned two demonstrator missions. CloudSat (joint NASA-CSA mission) is a cloud profiling radar mission. It is planned to fly in formation with ESSP3-CENA and EOS-AQUA. At this moment CloudSat and ESSP3-CENA are scheduled for a joint launch in early 2004. This will be the first cloud radar in space. Measurements are planned until the year 2006. CloudSat will fly only a 94 GHz radar. The most important differences between CloudSat and the proposed EarthCARE radar are:

- the EarthCARE radar is more than 10 times more sensitive (11 dB)
- the EarthCARE radar will have Doppler capability with a resolution of 1 ms^{-1} or better.

The increased radar sensitivity is very important for cloud detection. Liquid water stratocumulus clouds are difficult to detect with radar because of the small size of the liquid droplets. Ground-based studies indicate that the EarthCARE radar will detect around 40% of stratocumulus clouds; the lower sensitivity of the CloudSat radar will detect only 20%. For ice clouds, based on the CEPEX data set it is estimated that only some 80% of all radiatively significant cirrus clouds can be detected with a sensitivity of -27 dBZ (CloudSat) while with a sensitivity of -38 dBZ (EarthCARE) approximately 99% of all cirrus clouds are detected.

Finally, the increased sensitivity will result in improved applicability of the synergetic lidar-radar algorithms described in Section 5.8. Applying this algorithm with the radar sensitivity of EarthCARE, cloud particle size and Ice Water Content (IWC) for ice clouds can be derived with a typical accuracy of 30–40% that is consistent with a Top-Of-Atmosphere (TOA) flux accuracy of 10 Wm^{-2}.

To retrieve the correct IWC and optical depth, it is important that both the radar and lidar detect the whole cloud. The CloudSat radar sensitivity of -27 dBZ affects the retrieval results considerably. An example is shown in Figure 3.1. It can be seen that a large bias in the retrieved optical depth is introduced because of the reduced radar sensitivity. Large parts of the cloud are below the sensitivity limit of -27 dBZ. The gaps in the lines appear because the lidar and/or radar do not detect the cloud. Another example is shown in Figure 3.2 where an entire cirrus cloud layer would be missed by the radar in CloudSat leading to LW and SW TOA flux accuracies of around 30 and 20 Wm^{-2}, respectively. In this example the TOA flux accuracy for EarthCARE would be better than 2 Wm^{-2} for both SW and LW. In addition, the vertical profile of temperature and humidity from the EarthCARE FTS contributes to this high accuracy.

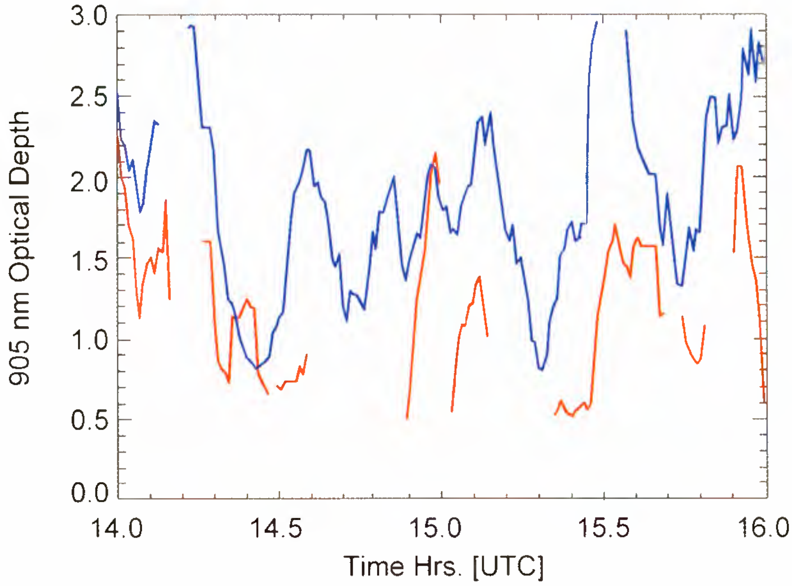

Figure 3.1: *Retrieved optical depth of an ice mid-level cloud based on lidar/radar retrieval for 17 April 1996. The blue line is the result of the retrieval with a radar sensitivity of -35 dBZ (maximum sensitivity of this particular radar system). The red line is the result of the retrieval with a radar sensitivity of -27 dBZ. The gaps in the lines appear because the lidar and/or radar do not detect the cloud. See Section 5.8 for details.*

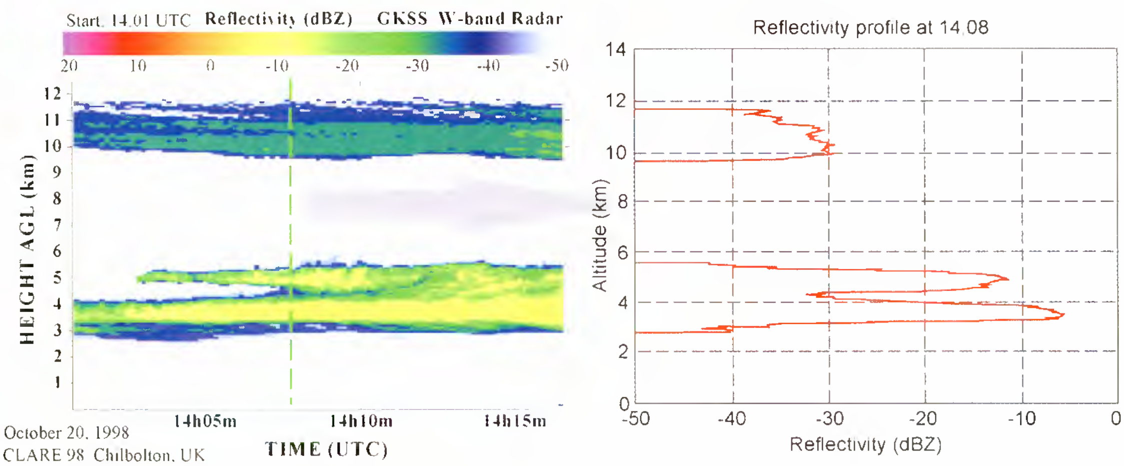

Figure 3.2: *Example of reflectivity profiles measured at Chilbolton during CLARE'98 with the GKSS 94 GHz radar. Note that with a sensitivity of –27 dBZ the cirrus cloud layer would not be measured.*

ESSP3-CENA

The ESSP3-CENA lidar satellite (joint NASA-CNES mission) is expected to be launched in early 2004 into a nearly polar orbit, flying in formation with the CloudSat and EOS-AQUA satellites. The ESSP3-CENA satellite will have two instruments: an imager and a lidar. The basic specification of the ESSP3-CENA lidar is comparable to that for EarthCARE. With this lidar it will be possible to derive cloud top heights and aerosol optical depths. With the lidar alone it will be very difficult to derive information on LWC/IWC. It will also not be possible to derive reliable information on particle size.

The use of a high spectral resolution lidar (one of the two technological solutions being considered for the lidar in EarthCARE), which re-uses the same technologies developed for ADM/AEOLUS, with two separate channels for the Mie and Rayleigh signals, would potentially add new capabilities in terms of the geophysical observables such as: a direct estimate of the optical depth in clouds and aerosols, capability of determining the backscatter to extinction ratio and the characteristics of ice particle and aerosol.

To accurately derive cloud microphysical parameters, lidar-radar measurements have to be combined. Because of the cloud variability at scales above 1 km it is crucial that the lidar and radar observations are collocated. This is an inherent problem for CloudSat and ESSP3-CENA missions as the lidar and radar will be flying on separate platforms. Although the average across-track distance between the two platforms is predicted to be fairly small (better than 2 km) this can still introduce errors on the radar-lidar retrievals. Extensive simulations have shown that these errors in retrieved effective particle size and ice water content can be very large even with spatial separations of the order of 2 km (see Section 5.8). One of the problems is that it is very difficult to estimate the actual accuracy of the retrieved parameters in these cases. It is hoped that the observed along track variability may provide help with this. This is subject of ongoing research. The objectives as defined for EarthCARE cannot be fully achieved by the combination of the CloudSat and ESSP3-CENA missions. This combined mission is regarded as a first step in the direction of a more complete understanding of interactions of clouds, aerosols and radiation.

In conclusion, CloudSat and ESSP3-CENA will provide the first vertically resolved data set for cloud research and a test bed for algorithms and processing. Members of the EarthCARE science team are closely involved in the science teams of both CloudSat and ESSP3-CENA. However, as noted above, there are fundamental differences between these missions and EarthCARE. There is a strong need for the EarthCARE mission after these two precursors, since they will not be able to provide the necessary closure of the Earth's energy budget regarding clouds. This is widely recognised by the scientific community involved in CloudSat, ESSP3-CENA and EarthCARE.

Other Missions

In addition, a TRMM (Tropical Rainfall Measuring Mission, launched in November 1997) follow-on mission, Global Precipitation Measurement (GPM), is planned and will have an additional 35 GHz radar to complement the single 14 GHz radar on the current TRMM. The major aim is to exploit the differential attenuation to provide more accurate rainfall estimates. The 35 GHz radar will only detect very dense (e.g. precipitating) clouds, but because the sensitivity is 40 dB less than for EarthCARE it will fail to detect most clouds. Again, common membership of the science teams will enable the EarthCARE mission to derive some benefit from GPM.

A well-defined strategy of inter-linked research activities will be beneficial to extend the objectives of EarthCARE. Central to this strategy is the bringing together of satellite observations, both operational (e.g. NPOESS, DMSP, MetOp, GCOM) and experimental (Envisat, ADEOS-II, EOS).

3.2 Unique Contribution of EarthCARE

EarthCARE is the first mission dedicated to the retrieval of profiles of cloud properties for use in weather and climate studies and driven by a target accuracy in terms of TOA radiative flux density (± 10 Wm^{-2}).

The primary aim of EarthCARE is to determine worldwide vertical profiles of aerosol and cloud field characteristics to provide basic input data for numerical modelling of weather and climate and atmospheric studies in general. The mission supports the goals of the World Climate Research Programme (WCRP), particularly its sub-programme Global Energy and Water Experiment (GEWEX), which aims to improve understanding of energy and water fluxes within the climate system, thereby securing reliable forecasts of weather and climate.

All predictions of future climate rely on global numerical models that, while very powerful, have limitations arising from parameterisation of sub-grid scale processes. Clouds are very important for weather and play a crucial role in both the hydrological cycle and the energy budget of Earth's climate. Despite their importance there are still large deficiencies in the representation of clouds and aerosols in present-day atmospheric models. Advances in model representation of clouds and aerosols are hampered by a paucity of data on their vertical distributions and characteristics. Vertical profiles of cloud and aerosols cannot be derived with the required accuracy from present spaceborne observations. This is a serious deficiency when attempting to validate model simulations of current climate and thus establish confidence in their ability to predict climatic change.

EarthCARE is expected to yield new insights into the divergence of radiative energy, interactions between clouds, aerosols, and radiation, vertical distributions of liquid water and ice water and their transport by clouds, cloud field overlap and horizontal structure and cloud-precipitation interactions.

The unique capabilities of EarthCARE arise from a mission design constrained by a target accuracy of 10 Wm^{-2} for the instantaneous TOA radiative flux density. This target has led to the selected instrument sensitivities and to the adoption of radar and lidar on a single platform to ensure co-location of their footprints. This is the first mission designed with such an approach.

The high sensitivity of the radar assures detection of 99% of all radiatively significant ice clouds. Co-location of the radar/lidar footprints assures that retrieval of Ice Water Content (IWC) and corresponding effective radius will be accurate to within 30–40%, which is necessary to achieve the stated accuracy in terms of TOA flux density. The radar/lidar combination will also allow the retrieval of information on crystal habit.

The Broad-Band Radiometer and the Fourier Transform Spectrometer provide an essential constraint on the retrieved properties. Synergy with the Multi-Spectral Imager will give additional information on cloud and aerosols, as well as providing the larger scale cloud context. The Fourier Transform Spectrometer will further supply water vapour and temperature profiles that are necessary to completely close the TOA radiative budget.

3.3 Expected Deliverables

EarthCARE will meet its objectives by measuring on a global scale:

- Cloud boundaries (top and base), even of multi-layer clouds, and consequently height-resolved fractional cloud cover and cloud overlap
- Vertical profiles of ice water content and ice particle size
- Vertical profiles of liquid water content
- The occurrence of layers of super-cooled cloud
- Sub-grid scale (1km) fluctuations in cloud properties.
- Detection of precipitation and estimation of light precipitation
- Detection and measurement of convective motions
- Detection of aerosol layers, estimates of their visible optical depth and the depth of the boundary layer.
- Short-wave (SW) and long-wave (LW) radiances at TOA.
- Water vapour and temperature profiles above clouds (and in clear air).
- Spectrally resolved TOA LW radiances.

4 Observational Requirements

4.1 Introduction

EarthCARE will meet the objectives previously discussed by measuring simultaneously the vertical structure of cloud and aerosol fields and their horizontal distribution over all climate zones, the temperature and water vapour profiles and the broad-band radiances emerging at the top of the atmosphere

It is crucial to measure, in a 'radiatively consistent' manner, as many of the relevant parameters as possible for a global sample of clouds and aerosols, and to link model errors in radiative quantities to cloud parameterisation errors.

To ensure that the radiative budget of clouds is closed, the specifications of the instruments have to be derived from a target radiative flux error at the Top-Of-Atmosphere (TOA). The target accuracy required by WCRP for monthly mean TOA radiative fluxes at the climate model grid scale (of order 250 km) is $\pm$ 10 Wm^{-2}. This target accuracy has been adopted for instantaneous TOA radiative fluxes derived from the different EarthCARE measurements on a 50 km spatial scale corresponding to modern GCMs.

The observations of EarthCARE will provide constraints, not achievable by any other means, to improve atmospheric models for both climate and NWP. As discussed in Chapter 2, the treatment of cloud/aerosol/radiation interaction is the most uncertain aspect in climate modelling. Progress in climate modelling is closely linked to progress in numerical weather prediction, so that these observations would also prove useful for operational meteorology.

4.2 Science Requirements

Figure 4.1 depicts the observations and approach required for EarthCARE. The products can be classified into three categories, namely those at the TOA, those within the atmosphere (e.g. clouds, aerosols), and those at the Earth's surface. Shaded boxes represent products that require ancillary data from other sensors assumed to be in space at the time of EarthCARE. The approach used in EarthCARE is to measure all atmospheric components that are related to clouds, aerosols, water vapour and temperature and then determine the associated TOA radiation budget. The comparison between the determined and the measured TOA radiance will provide a further constraint. For these reasons, the accuracy required for the measurements in EarthCARE must be determined in terms of the error in the derived estimates of TOA flux.

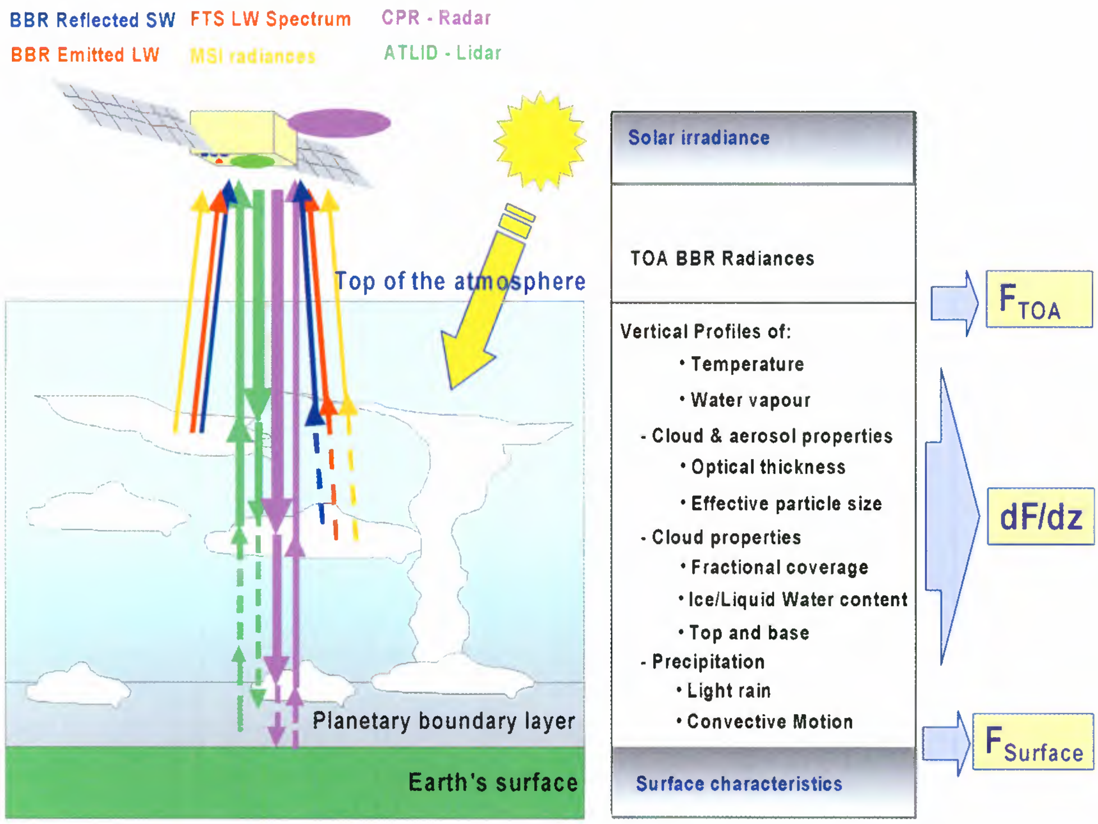

Figure 4.1: *The mission objectives of EarthCARE (F = radiative flux, dF/dz = vertical radiative flux gradient, SW = short-wave, LW = long-wave). The objectivel is to retrieve vertical profiles of cloud and aerosol characteristics, water vapour and temperature so as to determine radiative flux gradients within the atmosphere and fluxes at the Earth's surface, as well as to measure radiative fluxes at the top of the atmosphere. The left-hand part of the figure shows the atmospheric elements to be observed. Products required from EarthCARE are also shown (ancillary data from other sources are in shaded boxes).*

The global observations required to meet the EarthCARE objectives are listed in Chapter 3 and their accuracies and sensitivities are specified in Table 4.1 below. All are based upon the same requirement of a radiation flux target accuracy of ± 10 Wm^{-2}. The consequent instrument requirements will be discussed in Chapter 5.

The ability to detect the existence of clouds and aerosols at various vertical heights, which have a significant effect on radiative fluxes, needs to be specified. Brown et al. (1995) adopted the criterion that a radiatively significant cloud should produce a change in outgoing broad-band long-wave (LW) radiation or flux divergence, within the cloud layer, of greater than 10 Wm^{-2} and in surface downward LW radiation a change in flux of greater than 5 Wm^{-2}. They performed calculations with ice clouds at various heights in mid-latitude and tropical atmospheres, and deduced that it was necessary to detect cirrus ice clouds with an optical depth greater than 0.05 in the tropics and about 0.07 in the mid-latitudes. Assuming an effective radius of 20 μm for the ice crystals, this implies that the threshold of detectability should be an ice water path of about 1 gm^{-2} or, over a 1 km depth of cloud, an ice water content of 0.001 gm^{-3}.

The situation with liquid water clouds is rather different. Thin layers of water clouds such as strato-cumulus can have a large radiative effect. When compared to ice clouds, liquid water clouds consist of larger concentrations of smaller cloud droplets and also have higher water contents, so that their optical depths are generally much greater. For example, an adiabatic vertical profile of liquid water content increases typically by about 0.1 gm^{-3} per 100 m of cloud ascent, in which case a liquid water path (LWP) of 20 gm^{-2} would correspond to an adiabatic cloud 200 m deep with a mean liquid water content (LWC) of 0.1 gm^{-3}. These are very low values. However, to retain a sense of perspective, it should be noted that the SSM/I retrievals of LWP (which have been used so widely for deriving LWP cloud climatology) have a standard deviation of about 20 gm^{-2}.

The optical depth of a liquid water cloud at visible wavelengths is given by Slingo and Schrecker (1982) as:

$$\tau = \frac{3\mathrm{LWP}}{2r_e} \tag{4.1}$$

So, if the droplets in the cloud discussed above had an effective radius of 10 μm, the optical depth of the cloud would be 3. Water clouds with an optical depth of less than 1 can produce flux changes much larger than 10 Wm^{-2}. This would be produced by an adiabatic cloud with an LWP of about 7 gm^{-2}; that is a cloud 120 m deep with an average liquid water content of 0.06 gm^{-3}. However, strato-cumulus (Sc) clouds with optical depths smaller than 1 are usually not persistent. These optical depths are most often reached during the formation or dispersion of thicker clouds.

Regarding the accuracy of the cloud top and base, the studies of Brown et al. (1995) have also shown that a change in ice cloud top and base of 500 m resulted in a flux change of up to 10 Wm^{-2}. For water clouds at 300 K, the specification is slightly tighter: a change of 300 m, or about 2 K, leads to a change in IR blackbody radiation of 12 Wm^{-2}. These distances are comparable with the vertical resolution of current numerical models.

From the previous discussion, it is concluded that the threshold sensitivity to detect ice clouds with an optical depth of about 0.05 to 0.07 is about 0.001 gm^{-3} IWC for a kilometre deep layer of ice cloud. Brown et al. (1995) extended their calculations and showed that to detect a change in flux of 10 Wm^{-2} it is necessary to estimate the optical depth of mid-latitude ice clouds at 9.5 km height to an accuracy of a factor of two, but for cold tropical ice clouds at 16 km altitude an accuracy of +40/-30% is required. The

	Detectability Threshold	Accuracy
Vertically Resolved		
Cloud top/base ice liquid	n/a n/a	500 m 300 m
Ice water content (IWC)	0.001 gm^{-3}	+40 / -30%
Ice effective radius	n/a	+40 / -30%
Liquid water content and effective radius (no clouds above)	Optical depth 0.1	20%
Relative humidity	n/a	<30%
Temperature	n/a	<1.5 K
Integrated Variables		
Fractional Cloud cover Aerosol optical depth (for each 10 km distance in the horizontal)	5% 0.05	5% 10%
SW/LW TOA radiances	n/a	3 W $m^{-2}sr^{-1}$
Water Vapour		<10%

Table 4.1: *Accuracy of the observations required for EarthCARE geophysical products*

relationship of Stephens et al. (1990) between optical depth, ice water path (IWP), density ρ and effective radius (r_e) at visible wavelengths leads to the same fractional accuracy for the effective radius.

To derive the accuracy requirements for the water vapour and temperature profiles, a standard mid-latitude or tropical profile above a low-level cloud (stratocumulus) was used with 2 km deep slabs. This profile was perturbed by 30% in relative humidity and 1.5 K in temperature, giving a change of 2 Wm^{-2} per slab. For five slabs (10 km depth) this is well within our specification of total TOA 10 Wm^{-2}. These results (courtesy Piers Forster, University of Reading) were obtained using a narrow band radiation model with a resolution of 10 cm^{-1}.

4.3. Sampling and Orbit Requirements

The EarthCARE mission focuses on the quantification of interactions between clouds, aerosols and radiation. Determination of vertical profiles of cloud, aerosol and radiation field characteristics is absolutely essential for in-depth evaluation and improvement of numerical model representations (parameterisations) of the linked transformations of water and energy. This is important for reducing the still considerable range of uncertainty of climate projections, and improving the skill of medium-range weather forecasts.

To accomplish these goals, the EarthCARE package includes both active and passive instruments on a single platform, so that the footprints of these very different instruments are co-located. The different measurements then provide a maximum-synergy vertical slice of the atmosphere along the satellite track. Clouds are very variable in space and time, so when characterising a particular profile it is important that all sensors observe the same cloud. A typical multi-spectral imager in current use has a resolution of better than 1 km and, in an ideal system, the active instruments would provide a vertical profile within the same 1 km horizontal resolution. If the sensitivity specification of the active instruments requires a narrow nadir swath, then profile data would be available with an along-track resolution of 1 km. For isotropically distributed clouds, this would satisfy the requirement for fractional cloud cover to be observed to within 5% for a 50 km sized grid box.

Because of the relatively low altitude essential for obtaining maximum signal in the active instrument returns, the swaths of cross-track scanning (or imaging) instruments would necessarily be limited and gaps between successive orbital swaths would be inevitable. Consequently, EarthCARE will not provide samples covering the entire surface of the Earth and will not provide climatology in the usual sense. Rather, it will provide numerous samples of vertical profiles of clouds and aerosol properties constrained by TOA narrow-beamwidth radiance measurements. The samples of vertical slices will provide, optimally, the 'snapshots' needed of the state of the cloudy and aerosol-laden atmosphere.

Because the ultimate objective is to improve numerical circulation models used both for weather forecasting and for climate simulations, these measurements must be global. This imposes the choice of a (nearly) polar orbit, so as to be able to observe all climatic zones. With such a high inclination, rapid orbital drift is not available: one has the choice between a Sun-synchronous orbit and a slowly drifting orbit.

In a near-polar orbit, EarthCARE will observe all latitude zones with the exception of small polar 'caps', and so will provide good samples of all climate zones, with adequate distinction between different longitudinal sectors of continents and oceans as well. In this sense, an approach to climatology is possible. Indeed, considering the spatial coherence of large-scale weather systems, the lack of cross-track scanning does not reduce the number of independent samples at mid and high latitudes very much.

Thus, while using a snapshot approach, EarthCARE will also have a climatological dimension through three possible uses of the data:

- a purely statistical approach whereby data is classified according to geographical position

- classification according to atmospheric regimes, e.g. tropical cirrus anvils, mid-latitude depressions, etc.
- use of NWP or GCM with reliable (derived from EarthCARE) cloud parameterisation schemes.

Although a drifting orbit might eventually provide samples over all local times, it mixes diurnal and seasonal variations during a period which is too short to provide a true climatology. It also complicates spacecraft energy supply and thermal control. The drifting orbit, with variable solar angle, would also make both radiance-to-flux conversions of Broad-Band-Radiometer data and retrievals from the Multi-Spectral-Imager more complex and less reliable. Thus the choice of a Sun-synchronous orbit appears preferable, even though it obviously severely restricts the sampling of diurnal variations.

This may appear hard to reconcile with the objective of studying processes. However, it ensures comparability of measurements made on different days of a particular season or month, in a given latitude zone (or latitude-longitude area). Each 'snapshot' may be considered as a representative sample, at a given local time, of the range of situations to be encountered, in this sense providing an approach to a 'fixed-local-time' climatology. To follow the time evolution of a particular situation and process in detail, EarthCARE observations will have to be studied in conjunction with observations from a geostationary platform and/or (an equally geostationary) ground site. This situation is not peculiar to EarthCARE; it applies to any measurement made from a single satellite not in geostationary orbit.

With the choice of a polar Sun-synchronous orbit, the question of equatorial crossing time arises. Because MSI and BBR observations of reflected sunlight are crucial for characterising the cloud/aerosol layers and how they affect the SW forcings and feedbacks, near-terminator orbits must be avoided. A daytime equatorial crossing time not very far from local noon is preferable, especially for areas of the Earth where clouds undergo a diurnal cycle. However, although convective clouds over land are at their most active in the early afternoon, extended low-level oceanic cloud exhibits an early morning maximum. It is therefore impossible to define an optimal crossing time for the EarthCARE mission, aimed at sampling all climate zones.

In conclusion, a polar Sun-synchronous orbit with equatorial crossing time between 9:30 and 14:30 is suitable. In terms of mission duration, a two- to three-year lifetime would be required.

4.4 Data Delivery

The products that EarthCARE will deliver were listed in Chapter 3. In principle, due to the 'snapshot approach' used and its relation to cloud parameterisation, these products do not have any specific timing requirements. It is envisaged, however, that some of the EarthCARE products may be assimilated in NWP. For this purpose, this subset of data would be most valuable if available in near-real-time even if only on a best-effort basis.

5 Mission Elements

This chapter discusses the instruments required to achieve the objectives of EarthCARE. First the observational requirements are converted into specifications for each of the EarthCARE instruments, and then the use of these instruments, alone and in synergy, is discussed.

5.1 Overview

Reflecting the observational requirements in Chapter 4, the following elements are necessary to fulfil the mission objectives.

The instrument complement will consist of:

- A backscatter lidar (ATLID) to determine vertical profiles of cloud and aerosol physical parameters.
- A Cloud Profiling Radar (CPR) for the retrieval of the micro- and macroscopic properties of clouds.
- A Multi-Spectral Imager (MSI) to provide information on the horizontal structure of cloud and aerosol fields in support of the vertical profiles measured by the active instruments, as well as the inversion of the broadband radiometer data.
- A Broadband Radiometer (BBR) to measure short-wave (SW) and long-wave (LW) fluxes at the Top Of Atmosphere (TOA).
- A Fourier Transform Spectrometer (FTS) to provide spectrally resolved TOA LW fluxes and profiles of temperature and water vapour above clouds (and in clear air).

In synergy, the backscatter lidar, the cloud profiling radar and the multi-spectral imager will retrieve vertical profiles of aerosol and cloud physical parameters. In synergy, furthermore, the broadband radiometer and the FTS LW spectral radiances will provide (using MSI for cross-track horizontal inhomogeneities) validation constraints on the retrieved vertical profiles of atmospheric, cloud and aerosol physical parameters, through the derived TOA broadband fluxes and LW spectra.

5.2 Backscatter Lidar

5.2.1 Introduction

Backscatter lidars have been used for many years as ground-based and airborne instruments to analyse aerosol and cloud vertical structure and to determine their optical properties with high spatial resolution. The LITE (Lidar In-space Technology Experiment) mission onboard the Space Shuttle has further demonstrated that active remote sensing from space using a backscatter lidar system could bring unique information on the aerosol and cloud layer structure at the regional and global scale (Winker et al., 1996; Platt et al., 1994).

The data from the LITE mission in Figure 5.1 demonstrate that the lidar is able to detect targets over an enormous range of sizes from air molecules, through aerosols up to cloud particles. The weak blue backscattered signal in the figure is from the molecular backscatter; since the theoretical magnitude of this molecular return is known, this signal can be used to calibrate the lidar and also to quantify the attenuation occurring when the lidar beam passes through clouds. Aerosols are responsible for the regions coloured green, yellow and red in the lowest few km of the figure, demonstrating that the lidar can provide the vertical structure of the aerosol loading. Finally, the much more intense white returns are from the clouds. The lidar is able to define cloud top very accurately, as well as cloud base for those clouds that do not extinguish the signal. However, for thick clouds, the lidar signal can be completely extinguished and it is not possible to detect either the cloud base or any clouds at lower levels. Multiple scattering within the clouds can also be a problem as it alters the apparent cloud backscatter. This effect can be minimised by using very small lidar footprints.

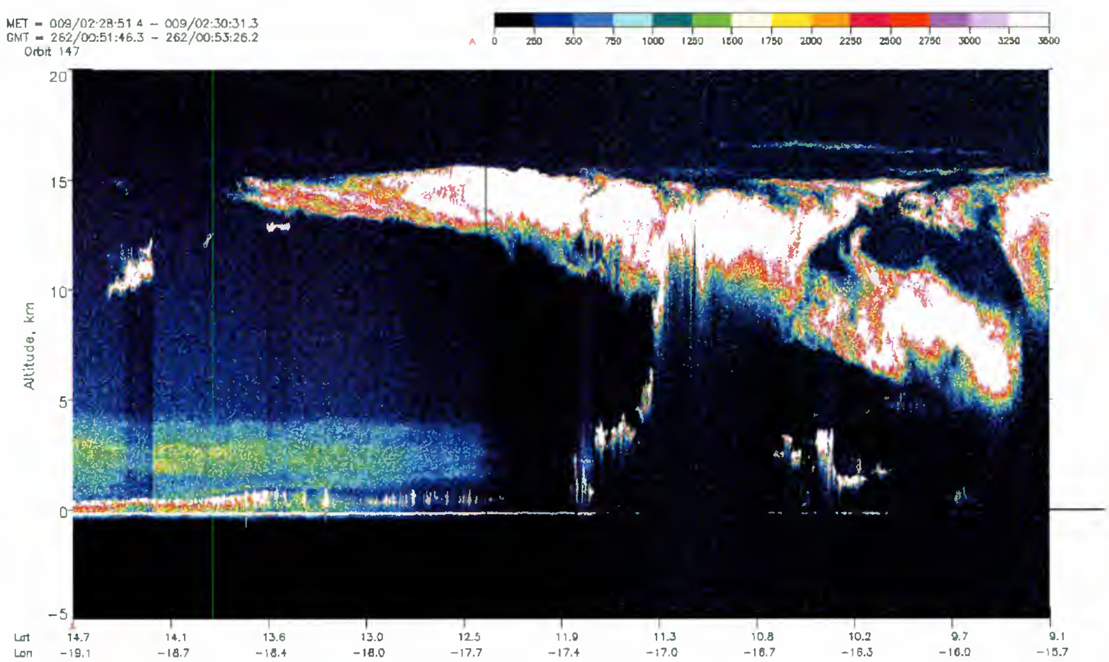

Figure 5.1: *2D lidar cross-section obtained during LITE mission showing the occurrence of clouds as intense backscattered lidar signals (in white), aerosols as moderate backscattered lidar signals (in green, yellow and red), or molecules as weak backscattered lidar signals (in blue) (after Winker et al.,1996).*

Threshold methods can be sufficient as a first approach for deriving the top and bottom of aerosol layers and thin clouds. However, for more quantitative analysis we need to consider how the observed backscatter at the satellite (β_{OBS}) is related to the actual backscatter coefficient (β_{TRUE}) of the target at range r after it has passed through a cloud or aerosol with an extinction coefficient (a):

$$\beta_{OBS}(r) = \frac{C\beta_{TRUE}(r)}{r^2}(1 + M(r))\exp\left(-2\int_0^r \alpha(r)dr\right) \qquad (5.1)$$

where C is a calibration constant for the lidar, the exponential term is the attenuation along the path and $M(r)$ expresses the increase in the incident radiation at range r due to multiple scattering, which becomes significant when the mean free path of the photons is much smaller than the dimensions of the lidar pulse. β the backscatter coefficient is measured in units of backscatter cross section per solid angle per unit length (m^{-1} sr^{-1}) and, for cloud particles, is approximately proportional to the cross sectional area. α is the attenuation coefficient in units of m^{-1}, and for clouds is approximately equal to twice the cross-sectional area. The ratio of α to β, the extinction to backscatter ratio, is known as the lidar ratio, S. Liquid cloud droplets are spherical and have a well defined value of S of about 18 sr, but ice particles can have different shapes and densities, and therefore S varies by a factor of four or so, typically ranging from about 15 to 60. Aerosol particles can vary in size, shape and chemical composition, so that S is even more variable.

Accordingly, quantitative interpretation of the observed backscatter, β_{OBS}, even in terms of a simple quantity used in radiative models such as optical depth, is not straightforward, and inferring the size, concentration and composition of the backscattering particles is even more difficult. Four factors contribute to this:

i) *Attenuation.* The lidar signal itself can be appreciably attenuated by ice clouds and often totally extinguished by liquid water clouds. This attenuation affects the measured backscatter (see Equation 5.1), but gate-by-gate forward correction algorithms are notoriously unstable and only a small initial calibration error causes them to fail.

ii) *Variable lidar ratio S(r).* In correcting for attenuation or deriving the optical depth from the measured backscatter, we need to know the lidar ratio, S. In ice clouds and aerosols the lidar ratio is variable and depends on particle size, shape and composition, and so it is very difficult to derive an extinction and optical depth from the measured backscatter.

iii) *Multiple scattering.* The component of the multiple scattering fraction *M(r)* that remains in the lidar beam leads to an unknown increase in the incident radiation and the delay introduced can lead to an apparent increase in range. These problems are minimised by using a small footprint.

iv) *Specular reflection.* Pristine ice crystals can fall with their major axes aligned horizontal and give a greatly enhanced backscatter for a nadir pointing lidar.

5.2.2 Proposed EarthCARE Implementation

The proposed lidar instrument for the EarthCARE mission will solve the lidar retrieval problems identified in the previous section by exploiting the following techniques:

i) ***Molecular Backscatter***

Rayleigh scattering is inversely proportional to the fourth power of the wavelength, and so EarthCARE will use a 355 nm wavelength lidar so that a significant molecular backscatter can be detected. The total lidar attenuation through the cloud/aerosol can thus be retrieved by comparing the observed Rayleigh signal at the UV wavelength with the theoretical prediction at that altitude. This total attenuation through the cloud provides a constraint to make the gate-by-gate attenuation correction algorithm stable and precise so that the true lidar backscatter can be derived. This can further be compared to the observed attenuation and the lidar ratio of the cloud/aerosol particles derived. This approach is used in the frame of the ESSP3-CENA mission.

ii) ***Mie Backscatter***

The Mie backscatter is measured at one of the channels of the lidar. This channel may either be the 1.06 μm channel of a dual-wavelength system or the Mie channel of a high spectral resolution system at 355 nm.

For the high spectral resolution lidar the use of the technology developed for the Atmospheric Dynamics Mission (ADM-Aeolus) would be of great benefit to EarthCARE. The ADM-Aeolus relies on using a high spectral resolution to discriminate the molecular backscatter (Rayleigh) and the aerosol and cloud particle returns (Mie scattering) at 355 nm. The molecular return has a Doppler width about two orders of magnitude larger than that of aerosol and cloud particles (a few m s^{-1}). Whereas the ADM mission detects shifts of 1 m s^{-1} in the mean value of the molecular return to derive line of sight winds, a variant of this system can be realised, which relies on separating the molecular and cloud/aerosol returns, by virtue of their very different spectral widths.

The technique has already been used at 532 nm by the ground-based NIES (National Institute of Environmental Studies) in Japan (Liu et al., 1999). Figure 5.2 displays vertical profiles through ice-clouds of the observed molecular and Mie backscatter, and range resolved derived values of extinction, true backscatter and lidar ratio. The technique uses the property that Mie and molecular returns are attenuated by the same amount.

The three stages of the retrieval are as follows:

1) the range resolved extinction coefficient is derived from the molecular backscatter, panel b
2) the ratio of the molecular and Mie returns is used to obtain the attenuation corrected profile of the true backscatter, panel c
3) the lidar ratio (extinction to backscatter) is obtained from 1) and 2) and is plotted in panel d

In this figure the lidar ratio in ice varies from 15 to 30 in a 2 km range; this magnitude is directly related to the crystal characteristics (habit, size).

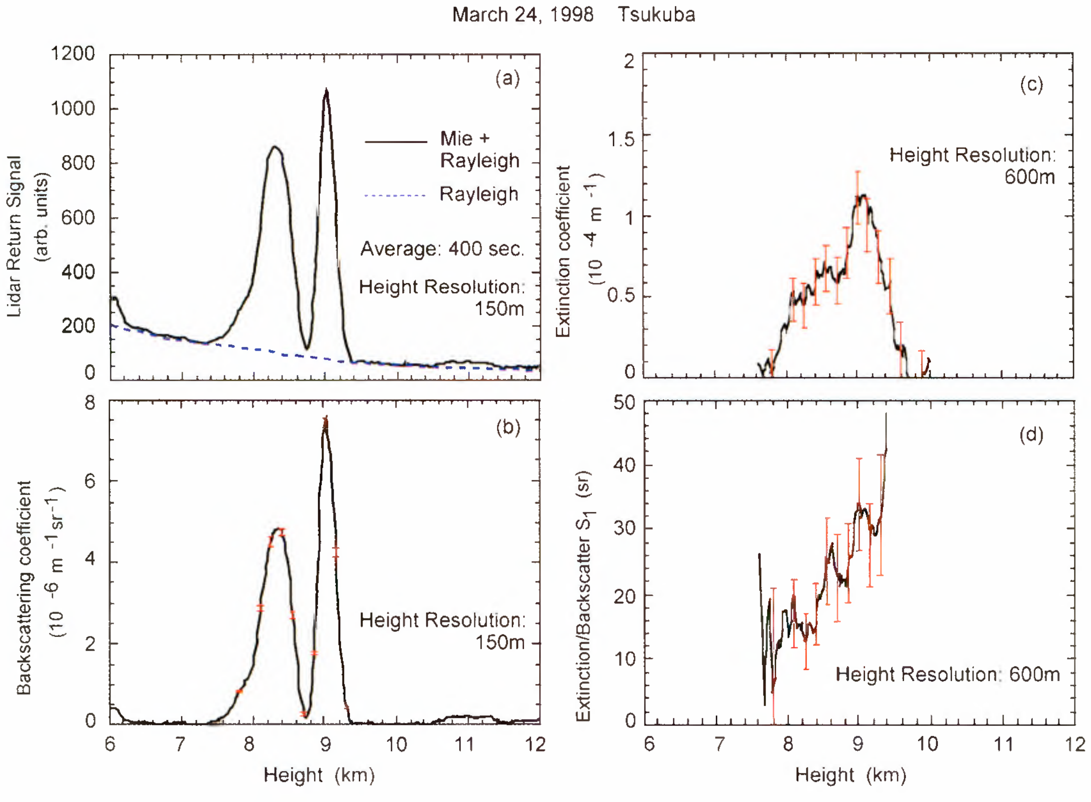

Figure 5.2: *High Spectral Resolution Lidar measurement at 532 nm (a), corrected backscatter coefficient (b), retrieved extinction coefficient (c) and retrieved extinction to backscatter coefficient (d). The vertical red bars represent the estimate error.*

Present indications are that for EarthCARE the molecular return should be detectable with a signal to noise ratio of at least 10 so that extinction coefficients can be obtained to an accuracy approaching 10% or 20% for thin clouds and aerosols. In this case the advantages of the spectrally resolved lidar technique are:

a) Direct measurement of the extinction coefficient at each gate.

b) The direct measurement of the extinction coefficient at each gate can then be used to provide a stable correction of the observed backscatter for attenuation, with none of the instabilities associated with forward gate-to-gate algorithms.

c) The ratio of the extinction to backscatter can then be derived directly at each gate. The magnitude of the ratio is directly related to the type of ice crystal present and the chemical composition of the aerosol.

For optically thicker clouds (but not thick enough to extinguish the signal) the isolation between the Mie and Rayleigh channels is being investigated as it may pose a problem. However, the difference in the Rayleigh channel, above and below the cloud/aerosol-layer still provides a measurement of the total layer attenuation that can be used, together with the Mie backscatter, to estimate the lidar ratio for the layer and therefore its particle characteristics.

iii) The multiple scattering contribution is minimised by use of a small lidar footprint (in the order of tens of metres).

iv) The lidar will be pointed by 2 degrees off nadir in the along-track direction, to avoid specular reflection, equivalent to a shift of 14 km or about 2 seconds. Ground-based observations (Thomas et al., 1990) at various zenith and off-zenith angles have confirmed that at this angle specular reflection is negligible.

v) ***Polarisation***

The implementation of a cross-polar receiver channel yields additional information on aerosol and cloud particle habits. Liquid water clouds generally (in the absence of appreciable multiple scattering) depolarise < 10% of the return, whereas the figure for ice clouds is higher and is dependent on crystal shape, thus providing additional information. The depolarisation ratio for aerosol particles also provides information on their shape.

The ability of a depolarisation lidar to identify the phase of the backscattering cloud particles and in particular the presence of thin super-cooled layers, is demonstrated in Figure 5.3, which shows backscatter and depolarisation data taken from the high flying ALEX lidar looking downwards. The extensive cloud – especially between 8 and 12 km – is confirmed as ice cloud by its high depolarisation ratio, but the thin layers of highly reflecting cloud between 6 and 8 km height are confirmed to be super-cooled liquid water by their virtually zero value of depolarisation ratio. Due to the size of the droplets, the

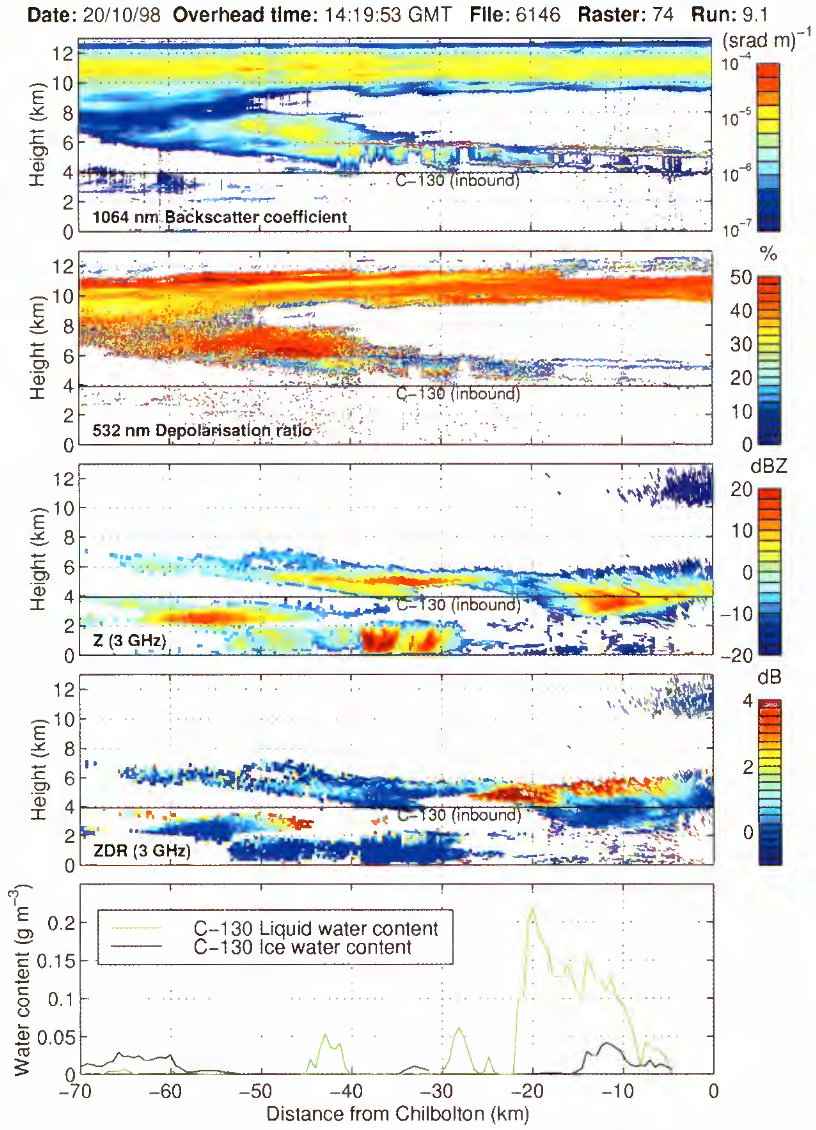

Figure 5.3: *Composite observations from 20 October 1998 during CLARE'98. Lidar backscatter at 1064 nm (top panel) and the depolarisation ratio at 532 nm (second panel) as measured by the ALEX lidar flying above 12 km onboard the DLR Falcon. The extensive ice clouds from 8–12 km have a moderate backscatter (top panel) but high depolarisation (second panel). Note the thin layers between 4 and 6 km height with a very high backscatter coefficient, but which show no depolarisation – confirming that these layers consist of supercooled water droplets. The third and fourth panels show the radar reflectivity and the differential reflectivity, respectively, as measured by the ground-based RAL Chilbolton radar at 3 GHz. The bottom panel shows the liquid and ice water content measured by the UK Met Office C-130 aircraft at an altitude of 4 km.*

radar cannot observe these layers, but a radar-lidar approach will also be able to identify them. As was discussed in Section 2.4 (iv) and Figures 2.16 and 2.17, we have reason to believe that these clouds are quite common and will have an important radiative impact, but are currently not represented in climate and forecasting models.

The combination outlined in i), ii) and v) means that for the first time it will be possible to derive an accurate measurement of aerosol optical and cloud depth and also provide an indication of their chemical composition and ice crystal habit.

The optical depth of an ice cloud is statistically related to the ice and water content because the former is the second moment of the size spectrum and the water content is the third moment. Figure 5.4 shows values of extinction coefficient and ice water content computed from a large data set of cirrus spectra obtained by aircraft. They show that, as expected there is only a small dependence on the mean size of the ice particle spectrum; however, a larger error of about 50% arises from the uncertainty in the density of the larger ice particles (not shown).

An even more powerful technique for retrieving IWC and ice particle size involves exploiting the synergy between the radar and lidar returns, together with the passive measurements as described in Section 5.8.

5.2.3 Required Sensitivity

Radiation computations show that if a radiatively significant scattering layer is to change the flux by more than 10 Wm^{-2} the optical depth in the visible must exceed 0.05. If we assume a lidar ratio of 50, as a worst case for an aerosol layer of depth 1 km, this means that the required sensitivity is a backscatter coefficient of 10^{-6} m^{-1} sr^{-1}. Because aerosol layers tend to be rather extensive, the required resolution would be 100 m in the vertical and 10 km in the horizontal. The lidar ratio of cloud particles can be as high as 50, but is usually somewhat lower, so the specification of 10^{-6} m^{-1} sr^{-1} would ensure that all radiatively significant clouds would also be detected.

The Rayleigh backscattered signal from molecules at 355 nm at ground level is about 8×10^{-6} m^{-1} sr^{-1} and decreases exponentially with height, with a scale height of 8 km where it will have fallen to about 3×10^{-6} m^{-1} sr^{-1}. For calibration purposes it is best to sample the high stratosphere because of the absence of aerosol particles, but in this case we can tolerate very long horizontal integration times. More difficult is the use of the molecular return to correct for the attenuation through clouds and aerosols over much shorter horizontal distances, ideally <10 km. The molecular backscatter at a height of 10 km should be estimated with an SNR of 10 for a horizontal integration of 10 km and 300 m vertical resolution.

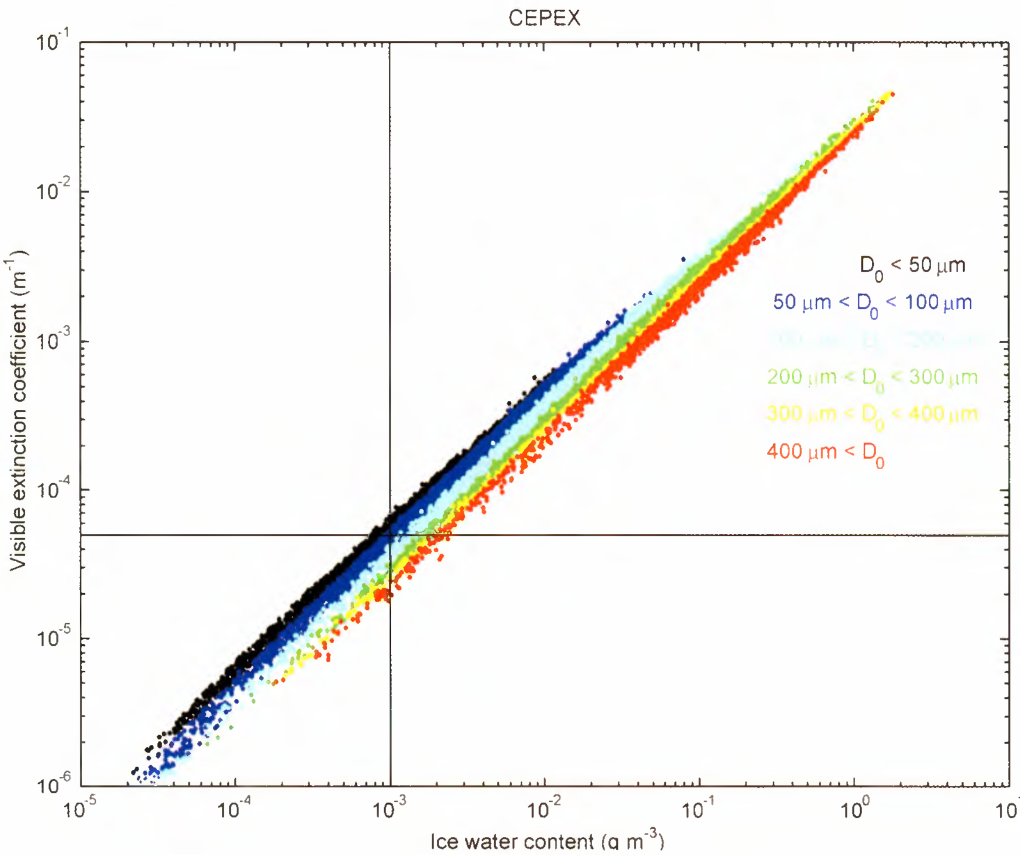

Figure 5.4: *Values of extinction coefficient and ice water content computed from the 12207 ice spectra in the CEPEX tropical cirrus data. Variability in ice density can introduce a 50% error. D_0 is the diameter that divides the size spectra into two equal volumes of ice. The two lines in the graph represent the requirements for IWC and extinction coefficient.*

For the Mie backscatter a sensitivity of 8×10^{-7} m^{-1} sr^{-1} would be required for a vertical resolution of 100 m, an integration length of 10 km and a signal to noise ratio of 2. To help in identifying particle habit a depolarisation capability would be required.

5.3 Cloud Profiling Radar

A 94 GHz cloud profiling radar has the unique property that it is able to penetrate ice clouds with negligible attenuation and provide a range-gated profile of cloud characteristics. During the past five years several of these radars have been operated from the ground and during airborne campaigns in Europe, Japan and the USA and have demonstrated their capability to reveal cloud properties. The reflectivity factor, Z, measured by the radar is proportional to $\int N(D)D^6dD$ where D is the size of the particles and N(D) is their concentration, and is expressed in units of mm^6 m^{-3} or more commonly in dBZ (=10 log Z) relative to a raindrop of size 1 mm in a cubic metre. Precipitation usually has Z values above 20 dBZ, but we are interested in cloud echoes, which are 50 dB below this level. Clearly aerosol particles (which the lidar can easily sense) are too small to be detected by the radar. For clouds, ice particles are generally larger than cloud droplets so the radar return from ice clouds is much larger than that from water clouds. The following is a discussion of the ability of the radar to detect various types of clouds as a function of sensitivity assuming a 500 m-gate length. This is compared with the required lidar performance. This analysis is based on fairly long term observations made with ground-based radar and lidar, together with extensive measurements within clouds made with instrumented aircraft.

5.3.1 Ice Clouds

The CEPEX data set constitutes one of the most complete *in-situ* measurements of ice particle size and concentration made in the important tropical cirrus over the Pacific warm pool. From these 12207 size-spectra, values of radar reflectivity factor and extinction coefficient have been calculated assuming the ice particle density (ρ in g cm^{-3}) as a function of ice particle diameter (D in mm) follows $\rho = 0.07\ D^{-1.1}$ (Brown et al., 1995). In Figure 5.5 the cumulative frequency distributions of the values

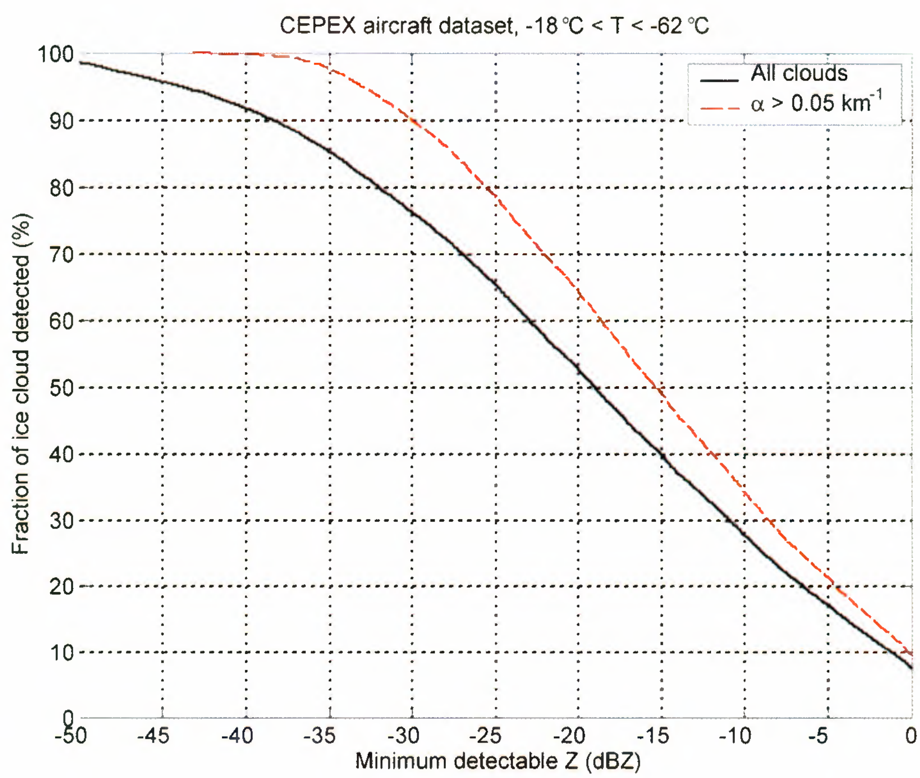

Figure 5.5: *Cumulative frequency of the detection probability of the tropical cirrus clouds in the CEPEX data set as a function of the radar sensitivity threshold. The red dashed line is for clouds with an optical depth exceeding 0.05 km^{-1}: the threshold value for radiatively significant clouds.*

of Z for all the spectra observed are displayed, and the frequency distribution for those spectra having an extinction coefficient exceeding 0.05 km^{-1}, the value deemed to be the threshold for radiative significance, is also shown. From the figure it can be seen that for a Z threshold of -20 dBZ, -25 dBZ, -30 dBZ, -35 dBZ and -38 dBZ the radar can detect, respectively, 52%, 65%, 77%, 85% and 90% of all clouds, and for radiatively significant clouds these figures rise to 65%, 78%, 90%, 98% and 99%. These cold tropical cirrus clouds are likely to be the most difficult to detect as they contain small crystals and values of Z in mid-latitude clouds, as demonstrated by the analysis of the EUCREX data set, tend to be rather higher. Accordingly, we conclude that a threshold of -35 dBZ will detect the overwhelming majority of radiatively significant ice clouds.

Cloud Base and Top

The radar will accurately measure the cloud top and base altitudes. A long series of ground-based comparisons confirms that the radar cloud base for ice clouds coincides with the optical cloud base as detected by lidar. Early suggestions that radar estimates of cloud base could be in error because of the presence of a few ice particles in fall streaks below the cloud base giving appreciable reflectivity appear to be exaggerated. A typical comparison of radar and lidar cloud base is shown in Figure 5.6 and the cloud bases derived from lidar and radar agree to better than 100 m. A crucial factor in whether the radar or lidar cloud base is lower is the absolute sensitivity of the two instruments and the size of the ice particles at the cloud base; if they are small then the limit is the radar sensitivity, but for larger particles the limit is the lidar sensitivity. The ground-based radar has a gate length of 60 m and a time resolution of 2 minutes with a sensitivity of -51 dBZ at 1 km height, falling to -31 dBZ at 10 km height, whereas the lidar has a gate length of 30 m with the same time resolution and a sensitivity of 2×10^{-7} sr^{-1} m^{-1}. The bottom panel in the figure shows the cloud bases derived when the sensitivities were degraded to -35 dBZ and 8×10^{-7} sr^{-1} m^{-1}; thresholds which might be expected for a spaceborne instrument. A statistical comparison of three months data of ice clouds confirmed that, using the full 'ground-based' sensitivity, 80% of the time cloud base agreed to within 200 m and 96% of the time to within 400 m. Using the sensitivities for spaceborne instruments, these values become 73% and 95%, respectively. The reason for the slightly degraded performance is that, although the sensitivity of the spaceborne radar is not very different to that of the ground-based radar, the spaceborne lidar threshold is a factor of four lower. This illustrates the rather surprising fact that the lidar sensitivity is the most important factor for providing accurate cloud base.

Radar Sensitivity

Analysis of the three-month period of the radar/lidar data set described in Figure 2.12 has revealed that the lidar frequently detects low-level water clouds that the radar cannot. However, it appears rare for the lidar to detect an ice cloud that is not seen by

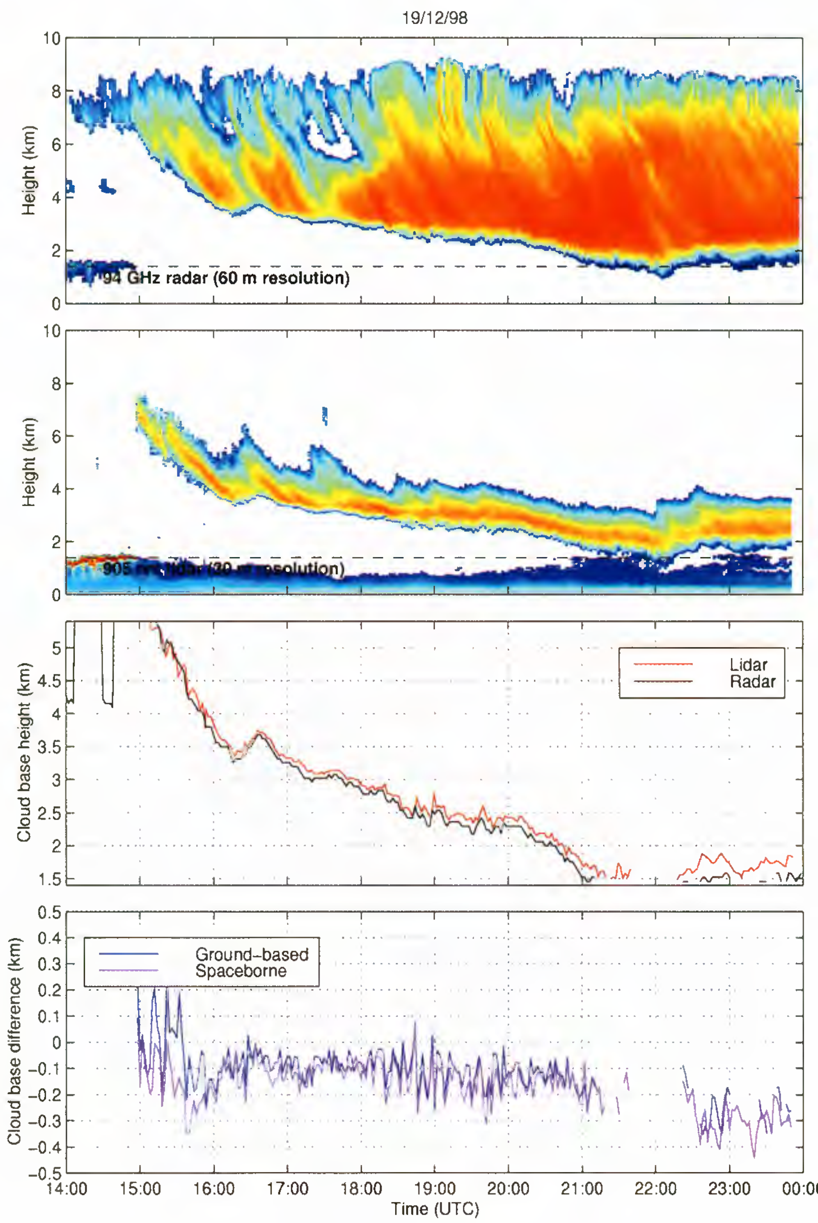

Figure 5.6: *An example of the comparison of radar and lidar cloud base. The top panel shows the 94 GHz reflectivity and the second the lidar backscatter coefficient. The third panel shows the cloud base heights from the two instruments using the full 'ground–based' sensitivities, and the last depicts the difference in cloud base height calculated assuming both ground-based and spaceborne instrument sensitivities.*

the radar. One day when this did occur is shown in Figure 5.7, where there are some super-cooled clouds at 6 km seen by the lidar but only intermittently by the radar (around 8:30 UTC). Aircraft penetrations have confirmed that super-cooled layers tend to form in thin layers that, because of the small droplet size, give a much large echo for the lidar than the radar. For the full 'ground-based' instrument sensitivities 3.9% of cold clouds (below 273 K) detected by the lidar in the entire three-month period were not seen by the radar. For the spaceborne sensitivity scenario this value drops to 2.1%. Again, the difference is because in degrading the data to the spaceborne scenario the lidar loses relatively more signal than the radar. These are very small fractions, but it is important to know how radiatively significant are such clouds missed by the radar. Estimating optical depth by converting the observed backscatter to an extinction coefficient and integrating up through the cloud, we find that only 1% of the clouds seen by the lidar but not seen by the radar have an optical depth of more than 0.05, the level deemed by Brown et al. to be radiatively significant. We conclude that a sensitivity of -35 dBZ is adequate for the radar to detect ice clouds but should be accompanied by a lidar of sensitivity better than 10^{-6} m^{-1} sr^{-1}.

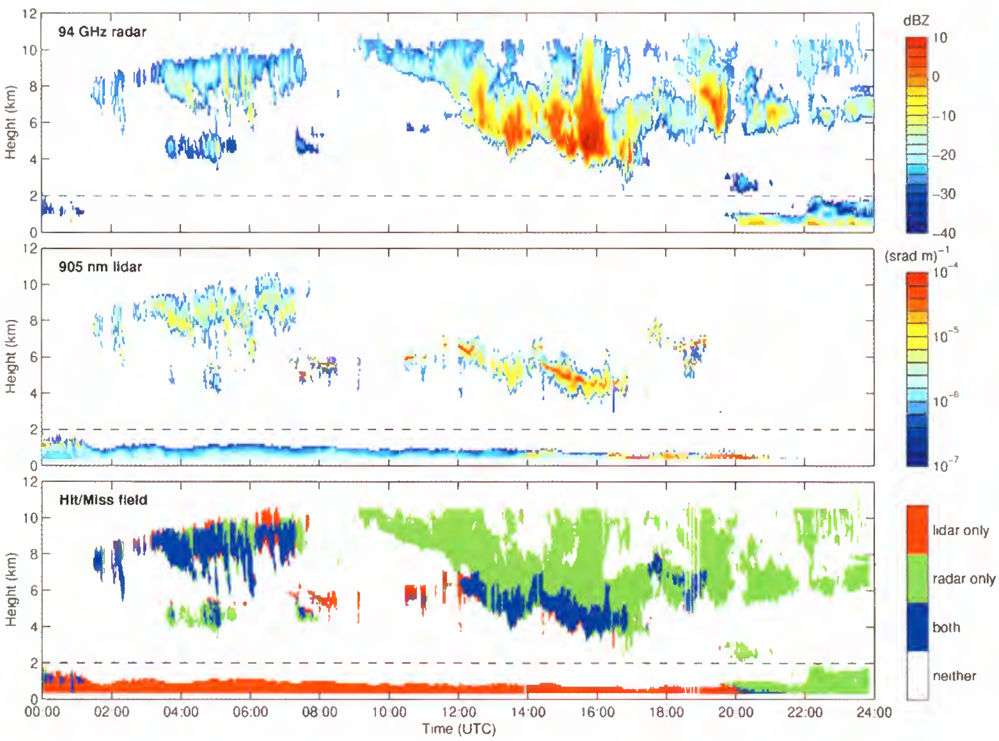

Figure 5.7: *Comparison of radar and lidar observations of cloud occurrence on 13 December 1998. The top panel shows the 94 GHz radar reflectivity, the second shows the lidar backscatter coefficient, and the third shows the 'Hit/Miss' field described in the text, for the full 'ground-based' scenario. The dashed line at 2 km indicates the minimum height at which one can be sure that the lidar is observing cloud and not aerosol.*

Ice Water Content

Section 4.2 established the requirement to measure the IWC down to 0.001 gm^{-3}. The radar sensitivity required to achieve this value of IWC needs to be defined. Figure 5.8 shows values of IWC and Z derived from the size spectra of the CEPEX dataset. It shows that there is some scatter in the relationship between Z and IWC even when D_0 is considered (as in Figure 5.4, D_0 is the diameter that divides the spectrum into two equal volumes of ice). Analysis of the data in the figure shows that for an individual observation of Z the value of IWC can be estimated to a factor of two and the mean value of Z for many observations should be accurate to about 30%. These errors can be considerably reduced if the data are also classified by temperature.

Figure 5.4 relates IWC to the extinction coefficient and shows that 0.05 km^{-1} (the level deemed to be radiatively significant) corresponds to an IWC detection threshold of 0.001 gm^{-3}. Figure 5.8 implies that to detect an IWC of 0.001 gm^{-3} a radar sensitivity of -35 dBZ is required.

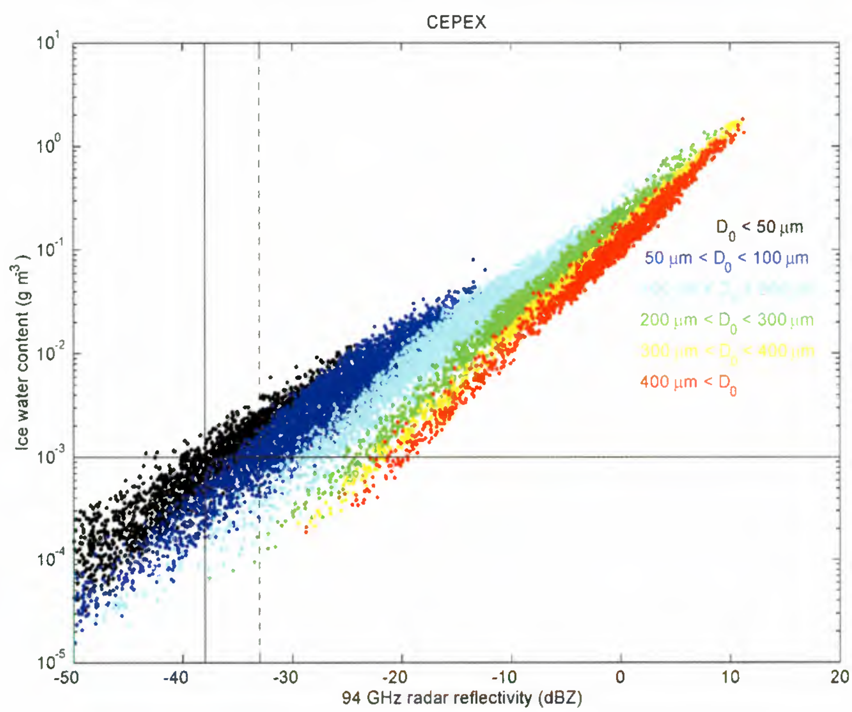

Figure 5.8: *As for Figure 5.4 but for calculated values of Z and Ice water Content (IWC) for the CEPEX dataset. The horizontal line in the figure shows the IWC threshold of 0.001 gm^{-3}. The two vertical lines denote radar sensitivities of –38 dBZ (10 km integration length) and –33 dBZ (1 km integration length).*

5.3.2 Water Clouds

Cloud Base and Top

The radar will measure thick water clouds. The thin water clouds are problematic with the present sensitivity. However, ground-based studies show that with a detection sensitivity of -35 dBZ at 1 km range the radar still detects 40% of the stratocumulus clouds seen by the lidar, but falls to 20% for a threshold of -25 dBZ. Of the clouds that are detected, about half contain occasional drizzle drops which often fall a few 100 m below the lidar cloud base. From a radiative point of view it is important to detect liquid clouds. For the stratocumulus cloud bases, which are not detected by the radar, we rely on the lidar (cloud top) and possible synergies with other instruments.

Sensitivity and Liquid Water Content

Further analysis of ground-based data showed that once the clouds are deeper than about 300 m they invariably contain occasional 50 μm diameter drizzle droplets that raise Z by more than 10 dB, so that they can be easily detected. This alleviates the detection problem and also means that the loss of signal associated with the attenuation in liquid water clouds (10 dB per km and per gm^{-3}) is no longer a problem. It does mean, however, that there is no direct link between Z and liquid water content of the liquid water clouds. Liquid water content can only be estimated using the radar and lidar in synergy with the passive instruments.

5.3.3 Precipitation

Detection and Measurement

One of the mission objectives is to evaluate the interactions of clouds and precipitation. To achieve this objective, it is necessary to detect whether a given cloud structure is precipitating and to estimate the precipitation rate. It should also be possible to provide reliable estimates of light precipitation of less than 0.1 mm hr^{-1} that are important for the evolution of clouds.

Convective Motion

Once a precipitating cloud has been detected, then the measurement of the Doppler velocity to an accuracy of 1m s^{-1} will be useful in separating stratiform from convective clouds. Current models have different parameterisation schemes for these clouds. The precise formulation of these precipitation schemes is presently a matter of some controversy and uncertainty.

5.3.4 Requirements for the Cloud Radar

Sensitivity

The analysis described above indicates that a sensitivity of -35 dBZ is required to detect the overwhelming majority of the cold tropical cirrus ice clouds which are radiatively significant, to provide accurate values for both the top and the base of ice clouds and to detect the vast majority of ice clouds which are seen by the lidar. This can be achieved using a 94 GHz radar with a pulse length of 3.3 μsec providing a range resolution of 500 m. A 2.5 m antenna and a 400 km orbit will give a footprint of about

600 m and for an along-track integration distance of 10 km, the sensitivity will be -36.7 dBZ for clouds at 2 km altitude in the tropics and -38 dBZ for ice clouds (at 10 km) with a radiometric accuracy of 1.7 dB. For a 1 km integration length the sensitivity is degraded by 5 dB (-33 dBZ corresponding to 95% of all radiatively significant ice clouds). The pulsed radar technique is straightforward and the above specifications are from previous studies carried out by both NASDA and ESA. CloudSat has a sensitivity for ice clouds of -27 dBZ, or about 10 dB (factor of ten) worse than for EarthCARE, and Figure 5.5 indicates it should detect only 83% of radiatively significant cirrus clouds.

Doppler

Implementation of conventional pulse-pair Doppler processing is difficult from a platform moving at 7 km s^{-1} because the Doppler broadening due to spacecraft movement leads to a very low value of correlation of successive pulse returns. The accuracy of the Doppler velocity estimate degrades exponentially as this correlation value falls, and so the performance depends crucially on having a radar pulse repetition frequency (PRF) which is as high as possible and a beamwidth, which is as narrow as possible. Studies have shown that with a 2.5 m antenna and a 10 km along-track integration, line-of-sight velocities can be estimated to better than 1 m s^{-1} provided that the reflectivity factor Z is above about -31 dBZ. This is for a PRF of about 6800 Hz (or an unambiguous range of 22 km that is sufficient to include all tropospheric clouds) and a variable PRF to accommodate changes in satellite height as it orbits the Earth.

It will be necessary to use surface return as a zero reference to correct for changes in satellite height as it orbits the Earth (maximum: ~20 m s^{-1} vertical velocity) and for the effect of off-nadir pointing errors. Figure 5.9, from the Japanese airborne cloud radar SPIDER, confirms that sea clutter provides a reliable zero reference to correct velocities to an accuracy of 0.1 m s^{-1}. Figure 5.10 shows the vertical velocity from liquid precipitating clouds.

Clearly, the technique requires further investigation and evaluation, particularly with respect to achievable PRF and use of surface return and pointing accuracy, but these studies and observations indicate the potential of the technique to provide unique data. There are indications, that with the cloud radar, 0.1 m s^{-1} accuracy can be achieved for Z > -17 dBZ, equivalent to 53% of tropical cirrus. Global data on vertical velocities would be extremely valuable:

i) Characterise convective up-draughts. Only a small amount of information from a limited number of field projects on the scales of up-draughts in convective clouds is available. Correct representation of such structures is a key element in the representation of the processes occurring over the Pacific warm pool. An accuracy of 1m s^{-1} would be useful.

ii) Detection of velocities to an accuracy of 0.5 m s^{-1} would enable the presence of drizzle to be detected. The production of drizzle is an important parameter influencing the lifetime and break-up of stratocumulus cloud decks.

iii) Current GCMs have an ice sedimentation velocity that is given by a simple function of ice water content. This parameterisation is crucial as the terminal velocity of the ice particles is the factor that determines the lifetime of cirrus clouds and the overall level of cloudiness predicted by models in the tropics. The velocities would be ideally needed to an accuracy of 0.1m s^{-1}.

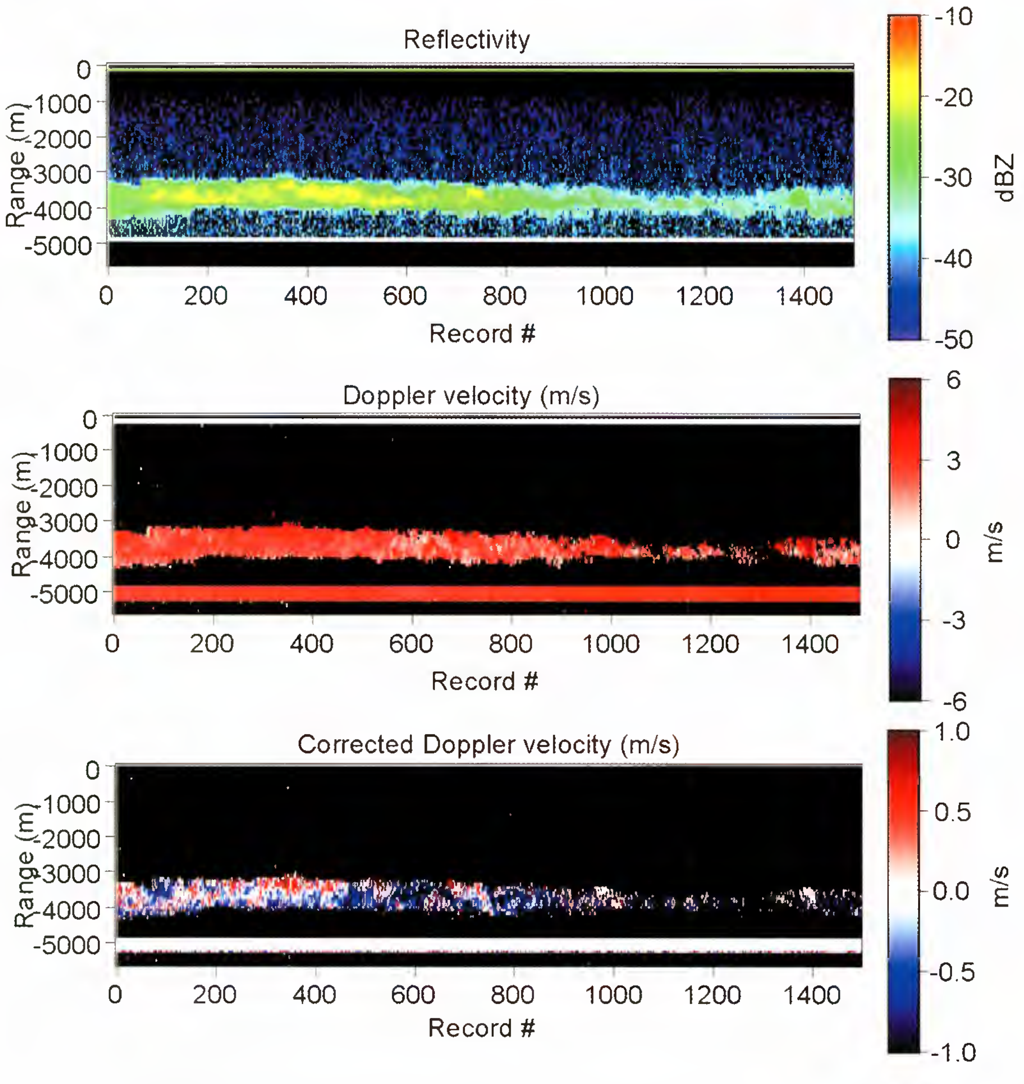

Figure 5.9: *An example of Doppler measurement of terminal velocity for liquid water cloud drops carried out by a down looking airborne 95 GHz radar. The top panel displays the reflectivity (dBZ) for a liquid cloud taken from a 25 km long flight path at 5000 m height. The white line at -5000 m corresponds to the sea surface echo. The middle panel shows the Doppler velocity in the radial direction. An off-nadir incidence angle causes a Doppler velocity offset of about 3 m* s^{-1}*. The bottom panel shows the cloud drop vertical velocity after subtracting the surface Doppler velocity.*

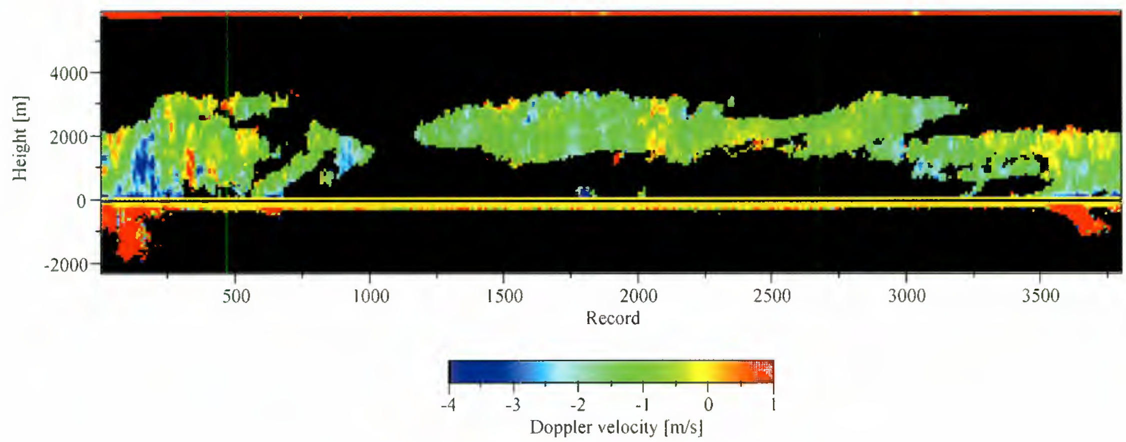

Figure 5.10: *Vertical velocity in liquid precipitating clouds measured by the airborne SPIDER along a 90 km path. The yellow line corresponds to the sea surface Doppler return.*

5.4 Fourier Transform Spectrometer

This instrument, a compact version of the IMG instrument flown on the ADEOS satellite in 1996, operating from 5.6 to 25 m with an unapodised resolution of 0.5 cm^{-1}, is optimised to provide a radiant constraint for evaluating the long-wave flux from the cloud/aerosol/water vapour laden atmosphere as well as for retrieving above cloud vertical profiles of temperature (to < 1.5 K) and water vapour (to better than 20–30% for 5 layers below the tropopause). This should be compared with the current ECMWF model humidity errors of about 50% in the mid troposphere. In addition, water and ice clouds can be distinguished, and the infrared emissivity and effective radius of ice crystals can be estimated. Spectral measurement of the outgoing radiance is an excellent tool for the assessment of general circulation model performance since it provides spectral signatures reflecting GCM processes that are simply not available from the spectrally integrated information. As recently demonstrated, a time series of the spectrally resolved IR fluxes may provide a fingerprint of anthropogenic radiative change (Harries et al. 2001). The footprint required for the FTS should be of 10 km so that the FTS measurements can be used in conjunction with the broadband radiometer.

Figure 5.11 shows an example of the height (km) versus wave number (cm^{-1}) cross section of the modelled net infrared radiative flux for cases of clear sky and thick cirrus layer located at 10 km height. The energy near the Earth's surface escapes to space mainly from the atmospheric window region located near 10 µm (1000 cm^{-1}). Existence of a cloud layer significantly modifies the Earth's radiative energy budget at various wavelengths, not only at the top of the atmosphere but also at various heights down to the Earth's surface. A thick cirrus traps, for example, the up-welling radiation from near the surface – yielding a larger contribution of radiative cooling in the upper atmosphere occurring at broader spectral range than that in clear sky condition.

Inversion of spectrally resolved infrared radiative flux obtained by FTS yields the vertical profile of the temperature and water vapour above the cloud layer, from which the vertical net flux profile and the radiative heating profile can be derived at several levels of the atmosphere above the cloud layer.

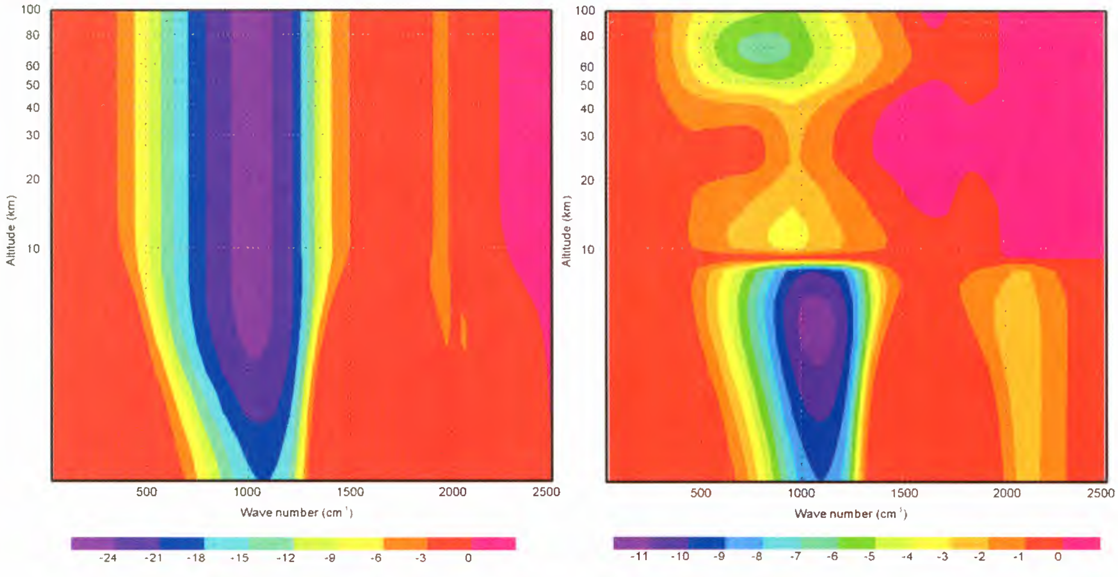

Figure 5.11: *A cross-section of height (km) versus wave number (cm^{-1}) of the net infrared radiative flux for cases of clear sky (left) and thick cirrus layer at 10 km height (right). The cloud layer significantly modifies the Earth's radiative energy budget at various wavelengths, not only at the top of the atmosphere but also at various heights and at the Earth's surface.*

5.5. Multi-Spectral Imager

A Multi-Spectral Imager (MSI) with a footprint of 500 m and 150 km swath operating at 660 nm, 865 nm, 1.6 μm, 2.2 μm, 8.7 μm, 10.8 μm and 11.8 μm will provide a broader view of the clouds being sensed by the narrow swath active radar and lidar. The wider swath of the multi spectral imager will also provide information on the cloud variability within one model grid cell.

To understand and interpret the measurements by the BBR and the active instruments the 'context' of the measurements should be identified. The Multi-Spectral Imager is intended to provide information on the horizontal variability of the atmospheric conditions and to identify atmospheric components. Quantitative analysis of the measured reflected sunlight yields information on the optical properties of the clouds and aerosols under study, while thermal infrared measurements yield information on temperature and infrared emissivity.

The use of Multi-Spectral Imager data in the characterisation of cloud and aerosol properties is well established. There are many algorithms developed for the retrieval of cloud properties from similar instruments: AVHRR (Kriebel et al., 1989; Derrien et al., 1993), ATSR (Watts, 1996), GOES and Meteosat (Minnis and Harrison, 1984; Rossow and Garder, 1993).

The cloud reflectance at a wavelength of 660 nm is a measure of the cloud optical depth. After assuming some cloud microphysical properties, this is then related to other cloud properties like LWP. This channel is also used to determine cloud cover fraction in daytime.

The reflectances in the 1.6 μm and 2.2 μm channels show dependence on the variation of the effective cloud droplet radius. The reflectance in this band gives an indication of the particle size. It can be shown that the reflectance increases with decreasing cloud droplet size. Results similar to those at 1.6 μm can be obtained using the 3.7 μm channel (Nakajima and Nakajima, 1995), but this channel is more difficult to handle due to the overlapping solar and terrestrial spectra and their corresponding low radiances.

Due to an increase in absorption for ice at 1.6 μm, the reflectance decreases. So, for optically thick ice clouds the reflectance in the 1.6 μm channel will be smaller than at 660 nm. This makes it possible to distinguish between ice and water clouds. This channel can be used to derive the optical thickness and effective particle size of cirrus clouds (Wielicki et al., 1990). It can also be used to detect clouds over snow.

For semi-transparent clouds, the temperature difference between the 10.8 and 11.8 μm channels is used to distinguish between ice and water clouds ('split window technique'). The amplitude of the temperature difference is related to the cloud optical depth in the infrared. The absolute value of the temperatures is used to derive the cloud top temperature (in the case of optically thick clouds). Ackerman et al. (1998) suggest using the combination of 8.7 and 11.8 μm which has a larger sensitivity for the detection of ice-clouds. However, there might be an ambiguity in the interpretation of the data in the case of multiple layered clouds (combinations of ice and water clouds). Furthermore, the emissivity of the land surface at 8.7 μm is very variable. These factors complicate the analysis if only the 8.7 and 11.8 μm channels are available. For this reason it is proposed to use all three IR channels (8.7, 10.8 and 11.8 μm) for EarthCARE. These three channels can then be used to retrieve the cloud top temperature, optical thickness and effective radius (King et al., 1992).

It is expected that information on the following cloud parameters can be derived from the Multi-Spectral Imager data: cloud cover fraction, optical thickness, effective emissivity, top temperature and liquid water column. Also for aerosols there are a number of algorithms developed for multi-spectral imagers like MODIS (King et al., 1992) and AVHRR (Durkee et al., 1991; Husar et al., 1997; Veefkind, 1999; Higurashi et al., 2000). It should be stressed that these retrievals are based on idealised models of clouds and aerosols involving several assumptions (Nakajima and Higurashi, 1998).

The MSI will in addition supply qualitative information in the first phase of interpretation of EarthCARE measurements and, due to its spatial resolution being comparable to the resolution of the active sensors, quantify the variability within the footprint of the BBR.

The cloud products described above can be retrieved from a Multi-Spectral Imager with six channels as specified in Table 5.2. The anticipated spatial resolution is 0.5×0.5 km^2. The Multi-Spectral Imager will have a swath of at least 75 km to both sides across track (150 km total).

Band 1:	0.649– 0.669 μm (VIS)
Band 2:	0.855– 0.875 μm (NIR)
Band 3	1.58–1.64μm (SWIR 1)
Band 4:	2.15–2.25 μm (SWIR 2
Band 5:	8.3–9.4 μm (TIR 1)
Band 6:	10.4–11.3 μm (TIR 2)
Band 7:	11.4–12.3 μm (TIR 3)

Table 5.2: *Channel Specifications of the Multi-Spectral Imager*

For the bands 1, 2, 3 and 4, the dynamic range of the channels ranges from 0.05 and 1.3 at a Sun zenith angle of 15 deg., at which a SNR of 200 will be obtained. The radiometric stability will be better than 1% of the estimated reflectance value over one year, and the absolute accuracy will be better than 10% of the estimated reflectance.

For bands 5, 6 and 7 the absolute radiometric accuracy will be better than 1 K at 300 K. The radiometric stability will be better than 0.3 K over one year.

5.6 Broadband Radiometer

The Broadband Radiometer (BBR) will measure reflected short-wave (SW) and emitted long-wave (LW) radiation from the Vertical Atmospheric Column (VAC) observed by the active instruments (lidar and radar) onboard EarthCARE. Specifically, the BBR will provide calibrated measurements for the determination of 'unfiltered' broadband radiances $\int L_\lambda d\lambda$ emergent at the TOA. The SW signal will be integrated from 0.2 to 4.0 μm; the LW from 4.0 to at least 50 μm.

EarthCARE science focuses on combining data from active and passive instruments to obtain vertical profiles along the satellite track. This leads to a requirement for absolutely calibrated broadband radiance measurements with spatial resolution of 10 km, compatible with the smaller footprints of the active instruments, along the satellite track. Scientific data users also need to be able to determine integrated broadband SW and LW fluxes and radiances compatible with general circulation model products over model-grid-scales of order 50 km at nadir. Essentially contiguous along-track sampling is needed with extension outside the BBR footprint using synergy with MSI data.

Instantaneous broadband flux determinations require information on the anisotropy of the radiance field emerging from the atmosphere, and this will be obtained by making measurements off nadir but along the track, with a viewing zenith angle close to 55 deg. Together with the nadir measurements, the off-nadir views will provide nearly simultaneous ($\Delta t < 100$ s) measured samples of the anisotropy of the reflected SW and emitted LW radiance fields from the observed along-track atmospheric volumes. These will provide a check on the applicability of the angular model chosen on the basis of cloud Multi-Spectral Imager data and used both for the unfiltering process and for the radiance-to-flux conversion.

The BBR measurements of broadband SW and LW radiances emerging from the VAC can be used in two different ways:

1) The principal use of BBR data in EarthCARE will be to constrain the derivations of vertical profiles of ERB components within the atmosphere and the vertical radiative flux divergence profiles. The important point is that computed energy fluxes depend not only on the physical property retrievals but also on additional necessary but only partially validated hypotheses regarding angular and spectral properties of the VAC. The BBR measurements provide a constraint independent of these hypotheses. Such an integral constraint, although not information-rich, provides a firm 'anchor' to the flux divergence calculation. To have confidence in the latter, it is necessary, although unfortunately not sufficient, to show that the calculated TOA radiances agree with those observed by the BBR.

2) In 'traditional' determinations of TOA radiation budget components, as for example in the ERBE, ScaRaB and CERES missions, SW and LW radiances are converted into values of upward instantaneous radiation fluxes. A spectral correction algorithm specific to the EarthCARE BBR using MSI, FTS and lidar data on the nadir scene will provide excellent unfiltered radiances, and ERBE or possibly advanced CERES algorithms and angular models can then convert the radiances into instantaneous fluxes. These will be obtained only along the satellite track. Other satellites will be used to monitor cloud and atmospheric properties, and will in particular include multi-spectral imagers with spatial resolution and spectral channels comparable to those of the EarthCARE MSI. Scientific teams at NOAA as well as in Europe have

produced ERB estimates using narrowband AVHRR data as well as geostationary satellite data; similarly, estimates based on the narrowband channels of ScaRaB have been compared with the truly simultaneous collocated broadband measurements. On EarthCARE, the broadband radiances measured by the BBR can be systematically compared with simultaneous collocated estimates of broadband radiances based on the EarthCARE MSI narrowband data, and for the LW on the FTS data. This will help to 'tune' the algorithms for estimating TOA SW and LW fluxes from narrowband data, and the success of such algorithms will help to define the limits of confidence that can be placed on ERB monitoring based on narrowband measurements from the operational weather satellites. In addition, analysis of the lidar-radar data on the observed VAC should improve understanding of the cases where the BBR measurements show that the estimates of ERB components using narrowband data are wrong.

The principal BBR instrument characteristics applicable to the EarthCARE mission requirements can be summarised as follows.

The BBR will measure broadband SW and LW radiances emerging at TOA from the VAC, both from nadir and from two directions forward and backward on the satellite track with viewing zenith angle close to 55°. The BBR nadir view will be collocated with the footprints of radar, lidar, Fourier Transform infrared Spectrometer (FTS), and the central footprint of the Multi-Spectral cloud Imager (MSI), and the forward and backward views must include atmospheric volumes also observed along the satellite track by the other EarthCARE instruments.

The BBR footprint will be of the order of 10 km, as will be the FTS footprint. Although the BBR and FTS footprints remain significantly larger than the active instrument and MSI footprints, their fields of view are small enough to yield valuable data on heterogeneous cloud fields whenever the scale of heterogeneity is of order 10 km or larger, this scale also corresponding roughly to the vertical extent of the troposphere. Note that smaller-scale heterogeneity is in any case difficult to treat because of the fully three-dimensional character of radiative transfer in such cases.

The basic BBR-specific products, provided for individual 10 km pixels, will be absolutely calibrated unfiltered SW and LW radiances emerging from the VAC to zenith and at viewing zenith angle 55° (both forward and backward).

In addition, TOA SW and LW fluxes, averaged horizontally over 50 km along-track, will be estimated on the basis of the BBR nadir and off-nadir pixels together with the near-nadir off-track MSI pixels These integrated products will be provided together with statistics of the BBR along-track variability and MSI cross-track and along-track variability on the 50 km scale. The observations off-nadir will allow estimation of instantaneous fluxes with 10 Wm^{-2} accuracy, and will allow assessment of the

Parameter		Mission requirement
Channels	SW LW	SW = 0.2 to 4.0 μm LW = 4 to >50 μm
Dynamic range	SW LW	0 to 450 $Wm^{-2}sr^{-1}$ 0 to 130 $Wm^{-2}sr^{-1}$
Absolute accuracy	SW, LW	<3 $Wm^{-2}sr^{-1}$
Viewing zenith angles	0°(nadir) 55°	Co-registered with FTS, lidar, radar FOV Along track, off nadir both aft and fore
Instantaneous field of view (single pixel: scale 1 area)	All channels All views	≈10 km
Sampling distance	All channels	Contiguous

Table 5.3: *Summary of the requirements for the broad-band radiometer*

reliability of the fluxes derived using standard angular models which, being only valid in a statistical sense, cannot promise such accuracy for instantaneous values. Other EarthCARE products, notably the vertical profiles of the radiative fluxes, depend on combining the BBR TOA products outlined above with calculations using retrieved atmospheric and cloud properties based on the other passive and active instruments on board.

5.7 Complementary Data From Other Sources

For the analysis and processing of EarthCARE data, other existing and available data sources can also be used, if applicable. First of all, data from other satellites can be used to assess additional information on the scenes. Furthermore, the output from state-of-the-art Numerical Weather models (NWP) can be incorporated in the analysis and the processing of the data.

The Meteosat series of geostationary satellites will be replaced by its successor, the Meteosat Second Generation (MSG). The latter's package of instruments includes the moderate-resolution SEVIRI imager and the Earth-radiation-budget radiometer GERB.

The SEVIRI imager will have a spatial resolution of 2.5×2.5 km^2 sub-satellite and a temporal resolution of 15 minutes. The 12 wavelength channels largely overlap with the channels of the EarthCARE imager (see Section 5.5). The high time resolution and sampling provides unique information on the temporal development of the cloud fields, which are observed by EarthCARE only once. The spatial variability and additional spectral information may be used as an additional source of information in the analysis of EarthCARE data. EUMETSAT has organised the development of retrieval algorithms and the data processing at so-called Satellite Application Facilities (SAFs).

The Climate SAF is strongly oriented towards the retrieval of cloud and radiation parameters from the SEVIRI instrument. The analysis of EarthCARE data will profit from the experience and infrastructure that is being developed in this group, but there is also a large interest in using EarthCARE data for the validation of the Climate SAF products.

The GERB instrument observes the TOA broadband SW and LW radiances in the direction of Meteosat every 15 minutes, i.e. for essentially all positions of the Sun in the areas observed. The spatial resolution is 48 km (sub-satellite) and a temporal resolution is 15 min. The instrument has a short-wave channel (0.35–4.0 μm) and a long-wave channel (4.0–30.0 μm). The large FOV of the GERB instrument makes this information very useful for the analysis of the larger scale phenomena.

The data from high-resolution imagers on polar satellites (AVHRR, ATSR, EOS AM/PM...) can be used to study the characteristics of the larger scale cloud fields. It is to be expected that coincident sampling of these imagers and EarthCARE will rarely occur. However, the large similarity between these instruments and the multi-spectral EarthCARE imager makes it possible to exploit the already existing know-how on the analysis of this data. However, the EarthCARE measurements of the vertical atmospheric column will also allow the validation of retrievals from multi-spectral imagers.

The advanced assimilation procedures of present-day numerical weather forecast models result in high-quality analysis fields. In the state-of-the-art 3DVAR and 4D-Var assimilation procedures, data from different sources are used and combined with the first guess. All available observations like radiosondes, 2-metre temperatures, surface humidity, winds, etc., are taken into account. The assimilation procedures therefore result in analysed fields of atmospheric parameters, which give the best possible description of the actual atmosphere. These fields will clearly be an excellent and important additional source of information to be used in the analysis of the EarthCARE data. For example, information of NWP fields can be used for the following topics:

- atmospheric temperature profiles in the synergy algorithms to estimate LWP from cloud geometry information and the assumption of sub-adiabatic profiles
- surface temperatures to set thresholds in retrieval algorithms for Multi-Spectral Imager data.

5.8 Synergy at Platform Level

The major mission goal, to provide information on the three-dimensional structure of radiative flux divergence fields, can only be fully met by exploiting the synergy of the data from the active instruments with those from the passive ones.

In this section we discuss the different synergies that exist between the EarthCARE instruments. The first sub-section starts by discussing the possible impact that different footprints of and samplings by each of the instruments may have on the synergetic retrievals. The following sub-sections discuss each of the main streams of retrieval namely: ice clouds, water clouds, aerosols, aerosol-cloud interaction and the radiative fluxes. Note that precipitation products as well as temperature and water vapour

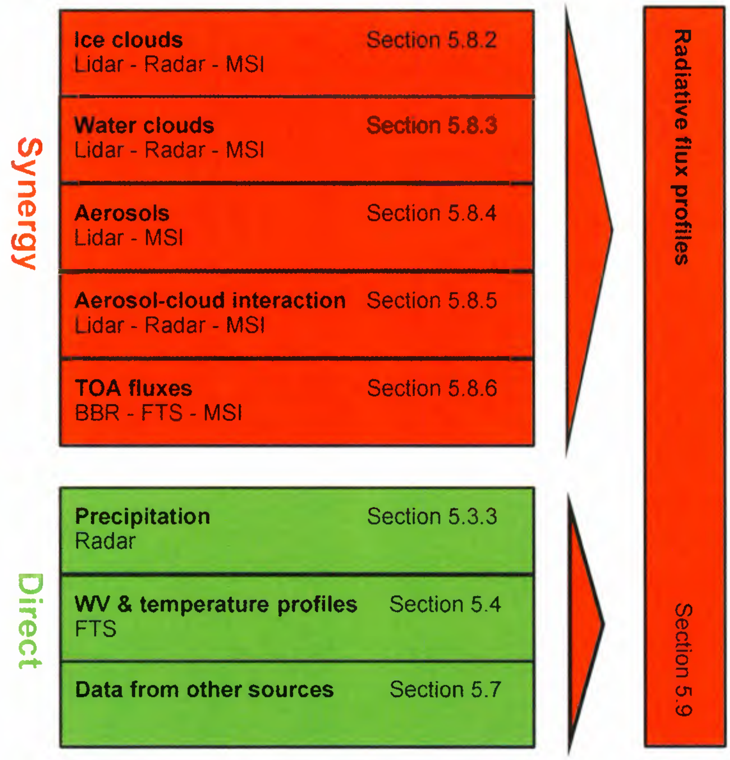

Figure 5.12: *The synergies between EarthCARE instruments and retrieval streams*

profiles will be mainly obtained directly from the cloud radar and the FTS, as illustrated in Figure 5.12.

5.8.1 Footprints, Co-location and Sampling

The EarthCARE instruments have the following sampling characteristics:

i) *Lidar*: An along-track linear row of footprints each around 30 m in size and separated by 70 m.

ii) *Radar:* A footprint of around 700 m with along-track integration of 10 km for maximum sensitivity but available at 1 km integration length with a 5 dB lower sensitivity (the lidar is pointed 2 degrees off-nadir along-track and the radar foot print is co-located with the lidar 2 seconds later).

iii) *FTS*: 10 km footprint every 10 km along-track.

iv) *Imager*: 500 m footprint with 150 km swath.

v) *Broadband radiometer*: 10 km footprint every 10 km.

Clouds are variable in space and so we now consider the effect of these different instrument footprints on the retrievals. The variability of ice clouds can be gauged from high-resolution lidar studies. Van den Heuvel et al. (2000) analysed 105 data points of the ELITE lidar ice cloud data set obtained with 18 m resolution flying under the LITE Shuttle mission and found that the power spectrum was well behaved and proportional to k^{-2} over the range 10 km down to 30 m (where k is the spatial wave number). Additional airborne and ground-based lidar data were analysed, extending the range down to 8.5 m and confirmed the spectral characteristics. Figure 5.13 shows an example of the high spatial resolution lidar data used. The aircraft flights were randomly directed with respect to the wind, and show no evidence of non-isotropic behaviour with respect to wind direction over these distance scales. Figure 5.14 shows a typical member of a large ensemble of 2D cloud fields generated with the spectral characteristic k^{-2}. The drastic changes over a distance of 3 km are obvious, whereas over a distance of 500 m changes are very much smaller. The next step is to sample the

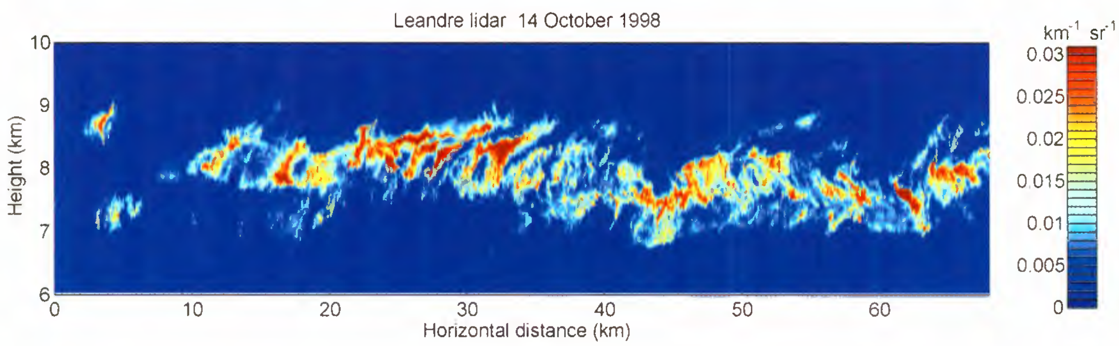

Figure 5.13: *Backscatter coefficient of a cirrus cloud, measured by the airborne 532 nm Leandre lidar during the CLARE'98 campaign with a 8.5 m resolution. The power spectrum of these data has a slope of -2.04.*

ensemble of the cloud fields with the footprints of the various instruments to quantify any errors introduced by the sampling.

Co-location and Footprint

Starting with the radar and lidar we first consider the effect of an across track separation of the footprints such as could occur if the instruments were embarked upon different platforms. Flying the radar and lidar footprints (100 m for the lidar as in the Earth

Radiation Mission – ERM) over an ensemble of cloud scenes as shown in Figure 5.14 and calculating the radar and lidar returns for a 10 km along-track integration, we find that the mean RMS error in the ratio of the returns for a 3 km across track separation is 70%, falling to 50% at 2 km, 25% at 1 km and only 5% for no across track separation. Since ice particle diameter is derived from the fourth or third root of the radar-lidar backscatter ratio, a 3 km separation is unacceptable, but 1 km or less is satisfactory. The 5% RMS error for the identical tracks arises because of the different footprint sizes of the radar and lidar.

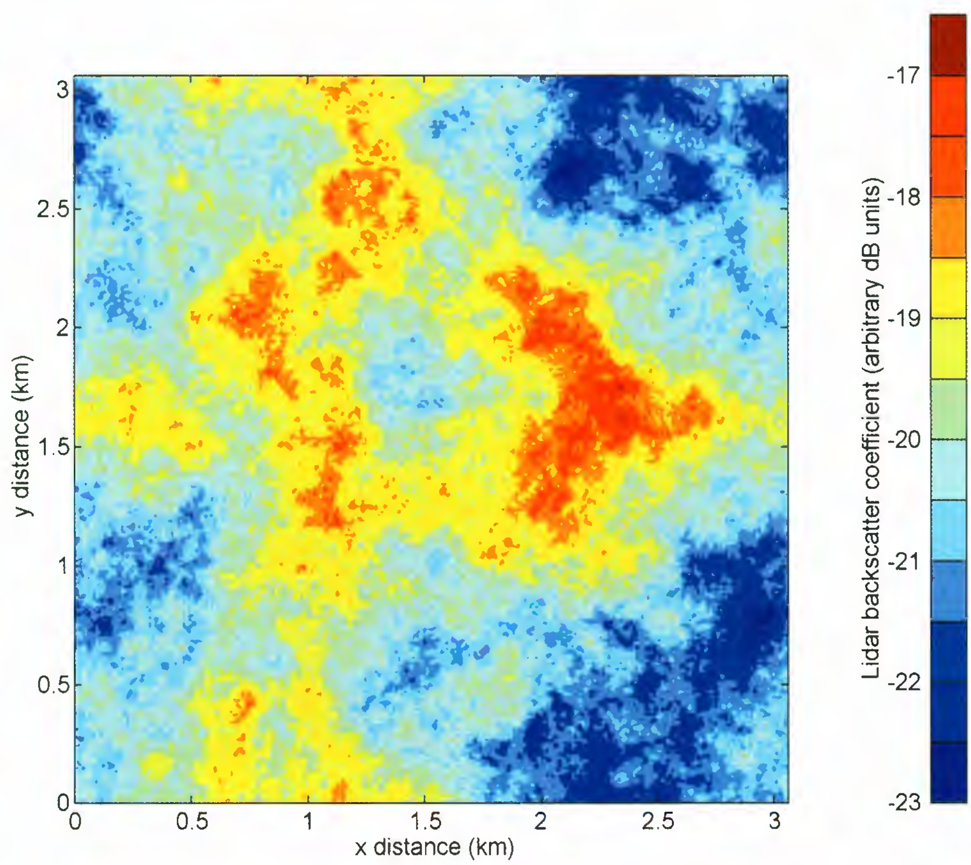

Figure 5.14: *A typical member of the ensemble of 2-D cloud structures having a k^{-2} spectrum, where k is the wave number. Note the drastic changes of Z or backscatter for separations greater than 3 km, but very little change over 500 m.*

Lidar Footprint

Examining the effect of footprint size further, a series of computations have been carried out with the footprints in Figure 5.15. In this case, only a 0.1 second integration, or a distance of 700 m, is considered, and lidar spots of 6 m or 30 m. Firstly, we compare the return from the 700 m diameter Gaussian footprint of the radar with the ten lidar footprints in a line along the major axis of the radar footprint with each lidar spot separated by 70 m. The RMS errors of the difference between the lidar and radar

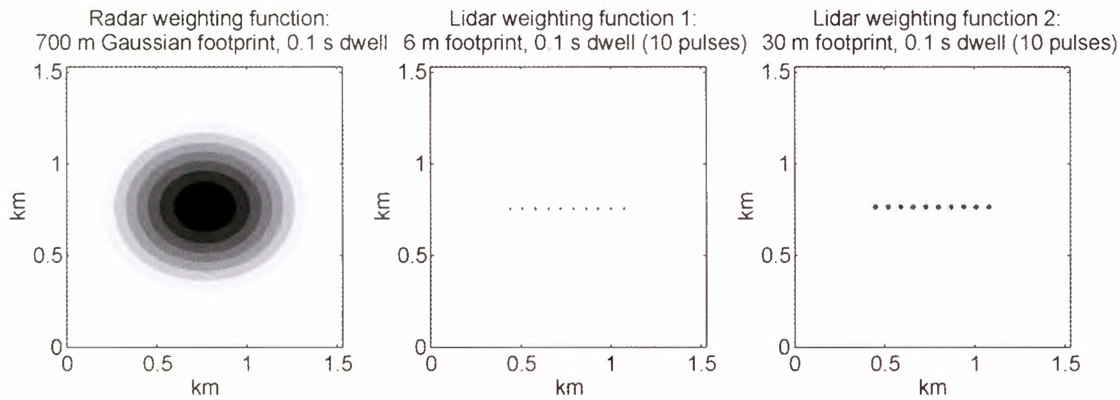

Figure 5.15: *The different sizes of radar and lidar footprints used to examine the error introduced on the retrieved signal by the sampling.*

backscattering for the 6 and 30 m lidar spots are virtually identical at only 8%. For reference, when considering a lidar footprint of 100 m, the RMS error between radar and lidar backscatter is 7%. If we consider the difference in the lidar backscatter from the ten footprints of 6 m and those of 30 m then the difference is only 2.2%. Thus, nearly all of the difference between the radar and lidar stems from the fact that the lidar does not sample the region to each side of its narrow swath, which the radar does sample. Simply defocussing the lidar from a 6 m to a 30 m footprint does nothing to remedy this problem and the error is almost exactly the same. It might be argued that there would be occasional wild points, when a cloud boundary happens to occur between the various footprints, but the statistics are well behaved. Figure 5.16 shows the histogram of the differences in dB between the radar backscatter and the lidar signal from the ten 30 m footprints; the difference between the radar and lidar signal exceeds 1 dB (25%) for less than 1% of the time. When comparing the signals from ten 6 m and ten 30 m footprints the mean difference was 2.2%, but the difference exceeded 7% for only 0.5% of the time.

These are all very small figures so it seems that the row of 6 m lidar spots separated by 70 m provides as good a sample as a row of 30 m spots; the smaller spot can have some advantages in that the lidar would be more sensitive and there would be less multiple scattering.

Conclusion

It can be concluded that for ice clouds the k^{-2} spectral behaviour results in an unacceptable sampling mismatch for radar/lidar backscatter comparisons when footprints are separated by more than around 1 to 2 km, but there is very little structure on the sub-km scale. Accordingly, the imager data, on a scale of 500 m can also be considered to be sampling the same ice cloud as the lidar and radar. When comparing the radar/lidar data with those obtained with the 10 km resolution of the FTS and BBR,

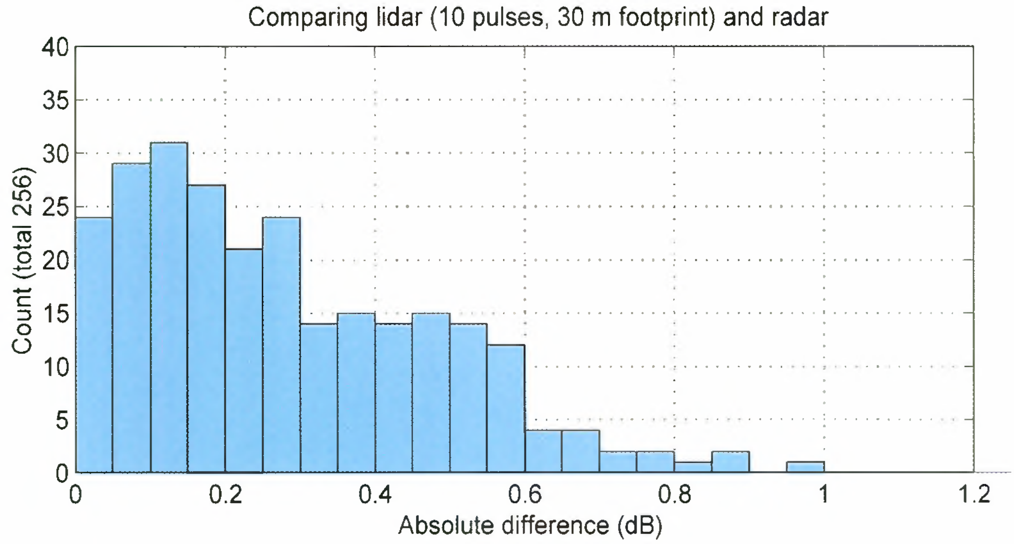

Figure 5.16: *The ratio (in dB) of the backscatter from the 700 m footprint and the backscatter from a row of 30 m lidar footprints for the ensemble of cloud structures shown in Figure 5.14.*

it will be necessary to consider the homogeneity of the imager pixels over the 10 km scale.

Water clouds, such as stratocumulus, have a similar k^{-2} or $k^{-5/3}$ structure, but for such clouds we are not relying on exploiting radar/lidar synergy, as the radar will fail to detect most stratocumulus. Instead the lidar attenuation will be used, together with the ratio of the reflectances observed by the imager, to improve droplet size and liquid water path retrievals. In this case, we are considering the agreement of the row of lidar spots with the 500 m-imager pixel. For ice clouds this should not pose a problem, but further studies are needed to confirm this for stratocumulus. The aerosol retrievals will involve the lidar accompanied on occasions by the imager, but these fields are expected to be much more homogeneous than clouds.

5.8.2 Ice Clouds

Radar and lidar have the potential to provide estimates of cloud particle size, but to do so the footprints of the two instruments must be co-located. Such information is extremely valuable:

- as a direct validation of effective radius used when representing clouds in models,
- when combined with radar reflectivity, it will enable the IWC to be estimated to an accuracy of about 30–40%. Radar reflectivity alone provides an accuracy of a factor of two, although knowledge of temperature improves this considerably.

The sensitivities of the lidar and radar onboard EarthCARE are well matched for simultaneously detecting radiatively significant cirrus clouds. The sensitivity margin available for the lidar ensures that the cirrus clouds will still be detected even when there is some attenuation of the lidar signal.

The combined use of the radar and lidar backscatter is a powerful technique for ice clouds. Essentially, the radar return for solid ice particles is proportional to D^6, whereas the lidar backscatter varies approximately as D^2, so the ratio of the radar to the lidar backscatter should vary as D^4. The fourth power dependence leads to a robust retrieval, a 100% error in the estimate of the radar-lidar backscatter ratio leading to a 20% error in retrieved size. A 20% error in size when combined with the absolute value of Z, is sufficient for deriving IWC to 30–40%. Intrieri et al., (1993) demonstrate the principle of the technique, but assumed that all cloud particles were solid ice spheres and limited the lidar retrievals to an optical depth of one. More recently, Mace et al. (1998) have repeated this exercise but assumed a more realistic variation of ice particle density with size.

However, neither of these two papers has tackled the lidar attenuation aspect rigorously. The ice clouds, which are of most relevance from a radiative point of view, have an optical depth in the range 0.1 up to about 3. Once the optical depth becomes larger than 0.2 or 0.3 then a simple gate-by-gate correction, for the lidar backscatter, becomes chronically unstable.

New techniques are described in literature (Donovan and Van Lammeren, 2001b; Donovan et al., 2001; Okamoto et al., 2000; Tinel et al., 2000) which overcome these difficulties and lead to an improved accurate and stable retrieval that relies on the coincident radar return to provide the constraint for the lidar attenuation retrieval. Essentially, the value of Z for the radar provides a first guess at the total lidar attenuation as well as the attenuation at each gate. Alternatively this could be achieved by using the molecular return from the spectrally resolved lidar backscatter.

As proposed by Donovan et al. (2001), the first guess for the lidar attenuation based on Z is then used in an iterative manner with the lidar retrieval to provide a consistent retrieval for both the lidar and radar. The technique is stable for both ground-based and airborne lidar and radar.

To account for multiple scattering effects, an inversion is performed first assuming no multiple scattering, then the retrieved extinction profile and particle sizes are used to estimate the multiple scattering contribution (to 3rd or 4th order). Once the multiple scattering contribution has been estimated as a function of range from the lidar, the single scattered power can be estimated. When this is done, an inversion is performed on the estimated single-scatter signal. The multiple scattering contribution is re-estimated as before and another inversion is then performed. The process is repeated until the estimated single-scatter power profile has converged. This effect is expected to be small in the case of EarthCARE due to the small lidar footprint.

Figure 5.17 (panel b) shows the results of the application of this technique to the measurements performed by the lidar and radar (Figure 5.17, panel a). These data were collected during the CLARE'98 campaign (CLARE'98) using the Leandre lidar and the Kestrel 94 GHz radar on board the ARAT aircraft. The lilac horizontal line indicates the flight path altitude of the UK Met Office C-130 aircraft collecting *in-situ* data with a number of sensors.

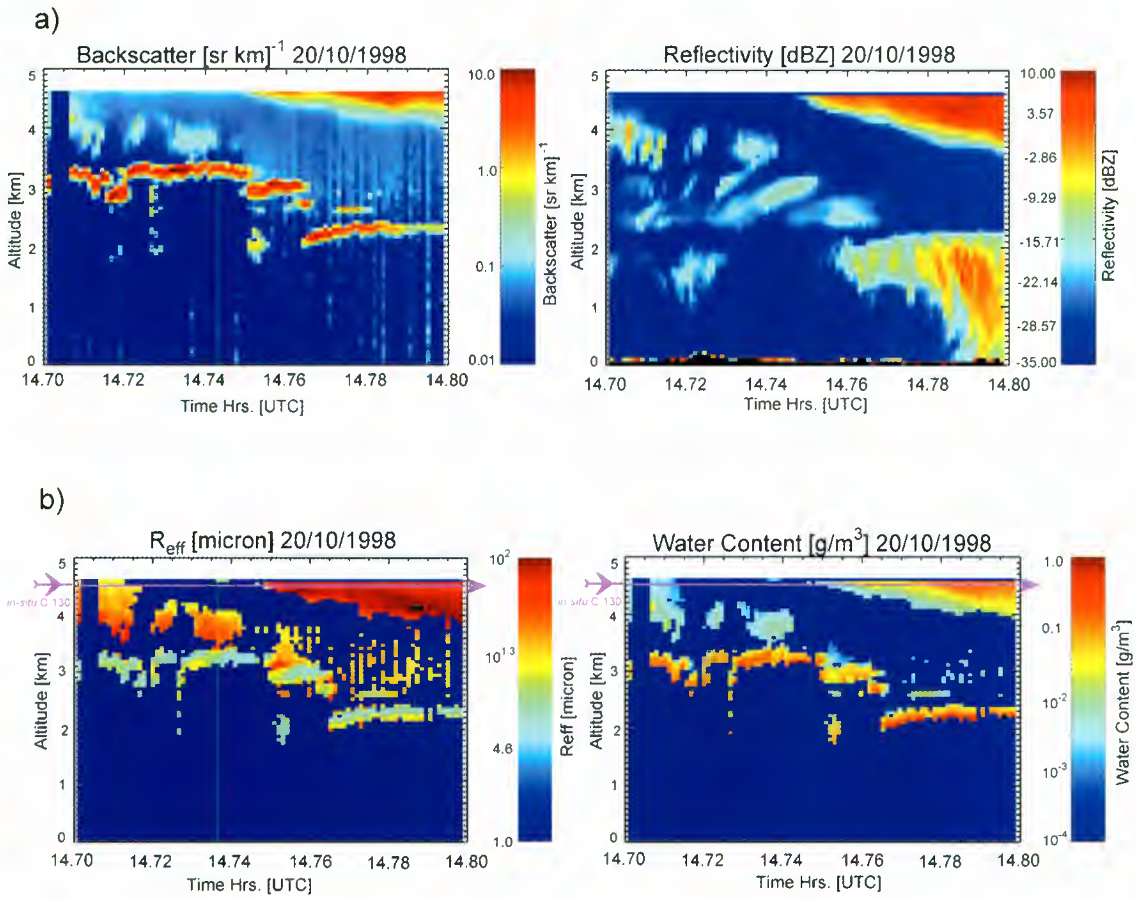

Figure 5.17: *Lidar and radar measurements (panel a) and derived cloud parameters (panel b) for 18 April 1996. Panel a) shows: left, the lidar backscatter and right, radar reflectivity. Panel b) shows: left, the retrieved effective radius and right, the ice water content. In panel b) the flight path of the in-situ measurements is also plotted (for additional information see Figure 5.18).*

Figure 5.18 shows a comparison between the *in-situ* measured and retrieved values. It shows the IWC and effective radius (R_{eff}) inferred from the 2D probe *in-situ* measurements and the lidar/radar retrievals. For the ice crystals the complex poly-crystal model of Mitchel et al. (1996) was used.

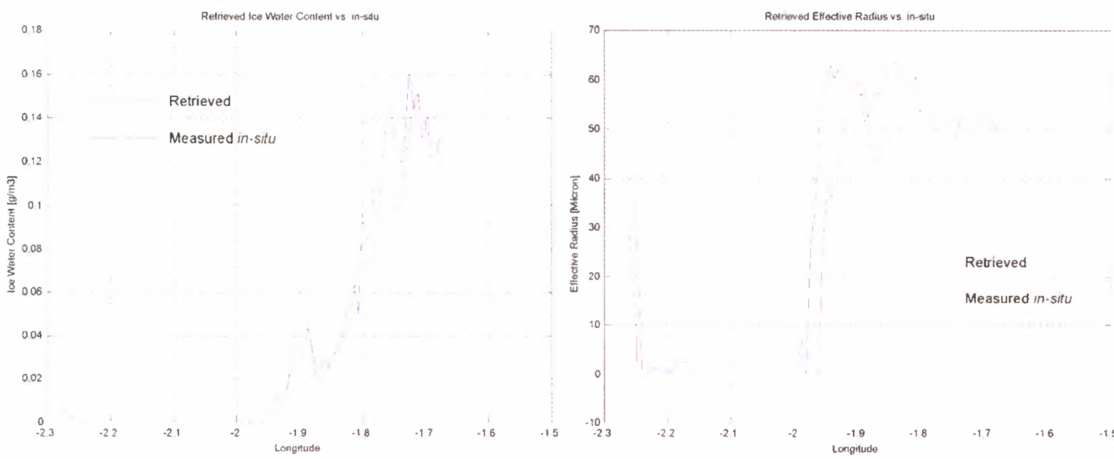

Figure 5.18: *Comparison of lidar-radar retrievals with the in-situ 2D probe measurements.*

Due to the different speeds of the ARAT and the C-130 aircraft, the distance between the two varied during the flight. Figure 5.18 is therefore plotted in terms of geographical coordinates to ensure the quasi-co-location of the measurements. The conversion from time to geographical coordinates was performed using the aircraft navigational aids.

Figure 5.19 shows the relative error between measured *in-situ* and retrieved ice water content as a function of aircraft separation. The impact of the measurement separation on the retrievals can be assessed from these data. The red graph shows the aircraft separation while the blue one shows the relative error in IWC, both as a function of time. Note that for an error better than 40%, the separation between measurements has to be less than 2 km.

The particle size as derived from the lidar radar algorithm, the lidar derived extinction – backscatter ratio and the lidar depolarisation ratio all provide information on the ice particle habits. The full potential of these unique data is currently being explored.

The synergy between the two active instruments as discussed above is very important, as it will allow the retrieval of vertical profiles of ice particle size and ice water content. Many other synergies are also considered which involve the passive multi-channel imager. The cloud top height inferred from the radar and lidar can be used with the IR brightness temperature. The difference can be interpreted in terms of size and optical depth and compared to the values retrieved in the visible and from the radar and lidar.

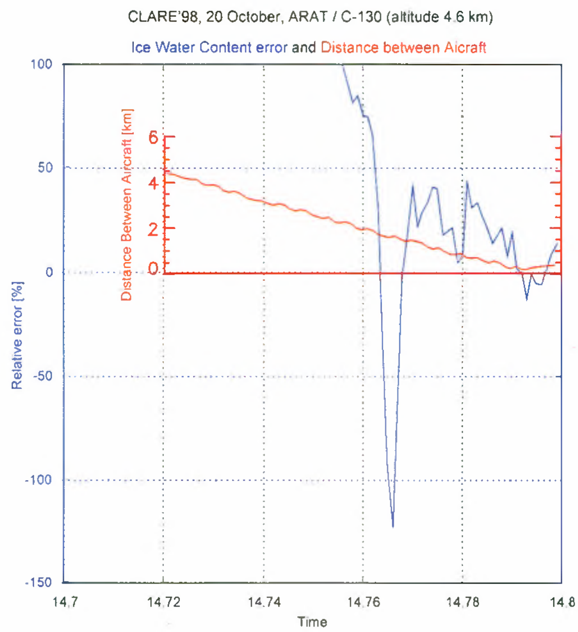

Figure 5.19: *Relative error between the retrieved and the in-situ measured ice water content (blue line and axis). The distance between aircraft (redline and axis) is also displayed for reference. The very high error just before 14.76 is due to a cloud edge effect. Note that the error in the retrieved IWC is less than 40% only for an aircraft separation of less than 2 km.*

Any differences in the optical depths should be consistent with the inferred ice particle size.

5.8.3 Water Clouds

A number of algorithms have the potential to be useful for the retrieval of water cloud properties. The following approaches will be used:

The lidar will be able to accurately measure the cloud base and top of optically thin clouds ($\tau<5$). On the other hand it is possible to estimate the cloud base height for optically and geometrically thick water clouds from the CPR observations. If only one of the active sensors detects the water cloud this provides information on the limits of the cloud optical depth.

The cloud emissivity can be derived from combining information on cloud altitude, atmospheric temperature at that altitude and underlying surface and observed cloud temperature (from MSI). Van Lammeren and Feijt (1997) have demonstrated that an exponential relationship between emissivity and liquid water path (LWP), for emissivities smaller than 1, can be used successfully for ground-based as well as for space based measurements (LITE). However, many restrictions apply in the retrieval of accurate emissivity values from space. It is planned to establish the applicability of this method for EarthCARE. The FTS will provide the temperature and water vapour profiles above the cloud. For this algorithm to be reliable, the cloud has to be unbroken on the scale of the imager pixel size.

The MSI optical channels can be used to derive the total cloud optical depth (provided that there are no ice clouds above). This optical depth can be used to estimate the total Liquid Water Path (LWP). Together with the cloud top height (measured by the lidar and/or radar) and the assumption of an adiabatic LWC profile, the cloud base height and the absolute LWC profile can be derived (Pelon et al., 2000). The effective cloud particle radius near the cloud top is also retrieved from the MSI. There is an ambiguity, however, in the derived size caused by a height variation of the quantities. This ambiguity is recognised to generate a further uncertainty in the statistics of cloud microphysical structure that are important for cloud formation processes and cloud-aerosol interaction. Profiling of the effective cloud particle size can provide a measurement for the height correction of the particle size obtained from the MSI.

5.8.4 Aerosols

The global distribution of aerosols has been studied mostly by passive remote sensing techniques. Three-dimensional aerosol distribution can be derived on global scale from combined imager and lidar data as the lidar-derived extinction cross section profile of aerosols is analysed simultaneously with the horizontal distribution of aerosol optical thickness from the passive remote sensing. For example, climatologies of the optical depth of aerosols over the ocean have been derived from the AVHRR imager. The lidar backscatter provides additional information on the vertical profile of extinction of the aerosols. The height-resolved extinction from the lidar should, when integrated, be consistent with the optical depth inferred from the imager. The nadir-looking configuration of the lidar will not result in serious difficulty for such a construction of the three-dimensional structure of aerosols, because the aerosol distribution tends to have persistent correlation over a distance of the order of 10 km, as seen in Figure 2.18.

It has been recognised that the effective aerosol particle size or particle size index known as the Ångström exponent can be used to identify the aerosol origin. Sulphate aerosols, which are dominantly emitted from anthropogenic sources, are classified as small particles, whereas mineral dust particles and sea salt particles are identified as large particles. Carbonaceous aerosols are observed as both small and large particles. Global distribution of such a particle size index is of enormous benefit for studying the direct and indirect effect of aerosols as well as for studying the trans-boundary transportation of anthropogenic aerosols. The two-channel algorithm of passive satellite-borne radiometers has suggested the characteristic distribution of anthropogenic small particles (Nakajima and Higurashi, 1998; Goloub et al., 1999). The technique of estimating the effective particle size from the high resolution lidar (Liu et al., 1999) will provide a unique and independent information to validate the effective radius information from the passive imager to improve the global map of the aerosol particle size. This improvement is especially important for calculating the column aerosol particle number, which is difficult to derive from the two-channel method with an imager, but is important for studying the aerosol-cloud interaction phenomenon (Andreae et al., 1995).

Lidar signals provide a strong constraint for aerosol optical thickness from the passive remote sensing technique. The derivation of aerosol signature tends to have serious errors due to causes, which are difficult to eliminate from the passive remote sensing technique, because the aerosol optical thickness is typically as small as 0.1. Cloud screening and degradation of the sensor sensitivity can cause serious degradation in the accuracy of the derived optical thickness. Lidar data analysis will provide a more solid base of cloud screening for pixels to be analysed by the imager.

Model assimilation of the active and passive remote sensing data will promise a significantly better result for the three-dimensional aerosol distribution retrieval including microphysics.

5.8.5 Aerosol-Cloud Interaction

Optical thickness and effective particle size radius (or Ångström exponent in the case of aerosol) retrieved from the imager are further used to study the cloud and aerosol interaction. Figure 5.20 shows an example of comparison of aerosol and cloud microphysical structure. There are characteristic similarities and differences between the aerosol and cloud fields. In terms of global mean statistics, a negative correlation between the cloud effective particle radius and the aerosol optical thickness was reported by Wetzel and Stowe (1999). Nakajima et al. (2001) show negative correlation between cloud effective radius and the column aerosol particle number and the opposite correlation (positive) between the optical thickness and the column aerosol particle number (see Figure 2.19).

Particle size profiles of aerosols and clouds are also derived respectively from the lidar data and the synergetic analysis of the lidar and cloud radar data. Such vertical profiling information is fundamental to validate the correlations derived from the imager because the imager cannot measure the effective height of the cloud-aerosol interaction.

5.8.6 TOA Fluxes

The broadband radiometer (BBR) determinations of radiative fluxes are relatively direct, but for sufficient accuracy, synergy with other measurements is important. Because of departures from spectral flatness of the BBR channels, an unfiltering process is necessary, using MSI data together with the spectra obtained by the FTS in the LW domain. Conversion of unfiltered broadband radiances into TOA fluxes can proceed, both for the nadir and the off-nadir views, using standard or new angular distribution models (and especially the BRDF in the SW domain), chosen according to

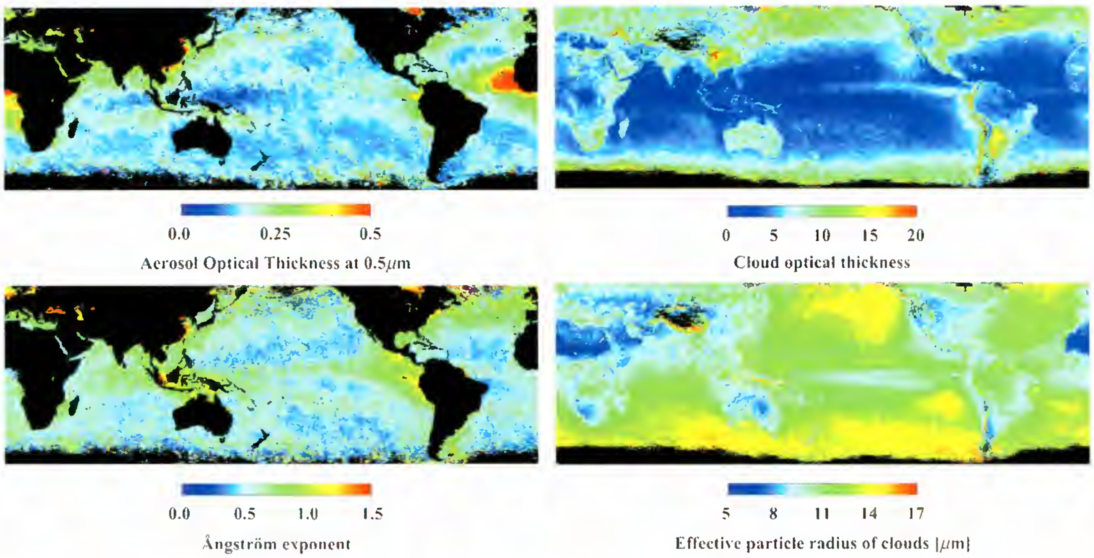

Figure 5.20: *Retrievals of the microphysical signature of aerosols and clouds from AVHRR. Aerosol optical thickness and Ångström exponent, and low-cloud optical thickness and effective particle radius, mean values for four months (January, April. July and October 1990). There are similarities and differences in the spatial patterns of the microphysical parameters.*

the cloud scene types determined using the MSI data. The three flux determinations corresponding to the three BBR views of each 10 km footprint can then be combined in an optimal estimate together with a figure of confidence depending both on the agreement between the three determinations and the horizontal inhomogeneity derived from MSI data. It should be emphasised that for instantaneous as opposed to monthly mean fluxes, the target accuracy of 10 Wm^{-2} is only achievable using such multi-angular views. The estimates of broadband TOA fluxes on the 50 km scale will use synergy between these BBR determinations and estimates using narrow-to-broadband conversion of MSI radiances both cross- and along-track within the larger area, inasmuch as the BBR only observes the central 10 km along-track. Again the MSI data will be used to calculate a figure of confidence in the flux determinations.

5.9 Synergy – Radiative Flux Profiles

Correct simulation of broadband radiative fluxes at the top of the atmosphere is a necessary but definitely not sufficient condition for validation of climate models, because vertical profiles of atmospheric and cloud properties can yield practically identical values, i.e. one can get the right answer for the wrong reasons. To be physically correct, climate simulations must reproduce the coupled energy and water fluxes in the atmosphere, and one may evaluate this with reference to the vertical profiles of radiative flux, i.e. vertical flux divergence. EarthCARE focuses on correct retrievals of vertical profiles of relevant atmospheric physical properties, including in particular the vertical profiles of cloud and aerosol properties known to play a crucial role in vertical flux divergence. The different components of the EarthCARE payload, separately and especially in synergy, provide simultaneous collocated retrievals of these properties, in particular within and below optically thick cloud layers where passive observations provide little vertically resolved information.

The top-level synergy of EarthCARE concerns the vertical heating profile as determined by the divergence of radiative flux. One physically consistent way to determine the vertical profiles of broadband radiative fluxes is to apply the equations of radiative transfer to the vertical profiles of atmospheric, cloud, and aerosol physical properties. Crude retrievals of such profiles have long been available using passive measurements as in ISCCP, and indeed these have been used to estimate vertical flux profiles from TOA down to the surface. Significant improvement can be made using narrower bands and higher resolution as in CERES, but estimates of flux divergence remain excessively uncertain. EarthCARE will provide a quantum jump in the accuracy of the retrievals of vertical profiles of aerosol and cloud physical properties, with particular attention to cloud ice. Consistency in the determination of vertical heating profiles will be ensured by: (i) referring accuracy requirements for all instruments to the WCRP 10 Wm^{-2} target accuracy; and (ii) having simultaneity and collocation of data of the different instruments guaranteed by construction.

At this stage, it is not clear whether methods exploiting inverse or adjoint modelling, using the BBR data together with MSI, FTS, lidar and radar data, can be developed to extract the best possible retrieval of VAC properties including the radiative fluxes and flux divergence. It may be that the best approach will be one of forward radiative transfer modelling using the properties retrieved from MSI, FTS, lidar and radar, and comparison of computed versus observed TOA LW and SW radiances.

5.10 Conclusions

An instrument complement to address the objectives of EarthCARE has been defined. It consists of:

- Lidar
- Cloud radar
- Fourier Transform Spectrometer
- Multi-Spectral Imager
- Broadband Radiometer.

With the above instruments, with the specifications discussed in this chapter, it will be possible to deliver the following radiatively consistent products:

- Cloud boundaries (top and base), even of multi-layer clouds, and consequently height-resolved fractional cloud cover and cloud overlap
- Vertical profiles of ice water content and ice particle size
- Vertical profiles of liquid water content
- The occurrence of layers of super-cooled cloud
- Sub-grid scale (1 km) fluctuations in cloud properties.
- Detection of precipitation and estimation of light precipitation
- Detection and measurement of convective motions
- Detection of aerosol layers, estimates of their visible optical depth and the depth of the boundary layer.
- Short-wave (SW) and long-wave (LW) radiances at TOA
- Water vapour and temperature profiles above clouds (and in clear air)
- Spectrally resolved top of the atmosphere LW radiances.

6 System Concept

6.1 Overview

A major innovation of the EarthCARE mission is the inclusion of both active and passive instruments together on a single platform. The mission will measure, in a radiatively consistent manner (better than 10 Wm^{-2}), all contributing atmospheric elements, as well as the Top-Of-Atmosphere (TOA) radiances, and consequently allow for the complete determination of the radiative flux structure.

The EarthCARE system concept is summarised in Figure 6.1, which lists all the constituent elements of the mission and their main parameters. These have been derived from the observation and performance requirements established in previous chapters. Emphasis has been placed on achieving maximum synergy between the elements.

The system elements as presented in this chapter have been jointly prepared by ESA, NASDA and CRL on the basis of two concurrent studies by European industrial consortia and further industrial studies in Japan for the cloud radar (CPR), the Fourier Transform Spectrometer (FTS) and the H-IIA launch vehicle.

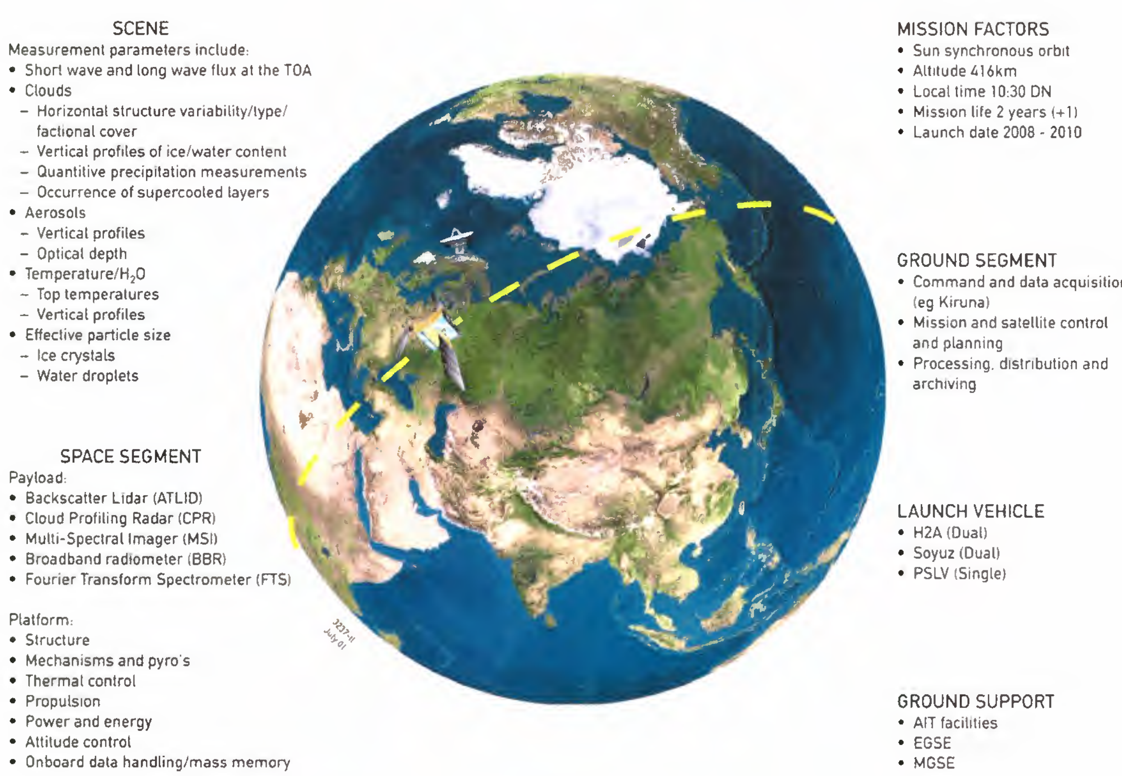

Figure 6.1: *EarthCARE system overview showing the key mission parameters.*

6.2 EarthCARE Payload

The EarthCARE payload is composed of two active and three passive instruments:

- An ATmospheric LIDar (ATLID)
- A Cloud Profiling Radar (CPR)
- A Fourier Transform Spectrometer (FTS)
- A Multi-Spectral Imager (MSI)
- A BroadBand Radiometer (BBR)

This instrument suite has been optimised to provide co-located samples of the state of the atmosphere along track. To this end, the centres of the instrument footprints will therefore be located as closely together as possible to ensure good co-registration. For the MSI, which provides a swath of 150 km, this refers to the nadir pixel.

Whilst all observations should be made in the nadir direction, there are system design considerations requiring different observation angles. The lidar needs to be pointed slightly off nadir to avoid specular reflection. Some of the MSI channels, which are obtained by means of in-field separation in the detector planes, will also be offset from nadir. One of the two spectral bands of the FTS will be pointed forwards as a result of the instrument design concept. Lastly, the forward and backward views of the BBR are offset by rather large angles for optimisation of the radiance-to-flux conversion process. Even with these technological constraints the observations are co-registered in the space-time domain, fulfilling the co-location specifications arising from the synergy requirements, through the design of the satellite system.

The relative locations of the instrument footprints are depicted in Figure 6.2. The centre of the lidar telescope line-of-sight has been selected as the reference; it is shown projected to true nadir. The BBR and FTS pixels are not shown, for clarity. Their size is much larger than that of the other instruments, thereby relaxing their alignment requirements.

A lidar-radar co-registration requirement of 350 m (goal: 200 m) has been formulated under the assumption that the two footprints (650 m and 20 m, respectively) should always overlap. The same requirement has been set for the MSI pixels, again assuming that the spatial offset of the non-nadir looking channels will result in an acceptable temporal offset. The initial assessment of the satellite design implications has shown that even the stricter requirement can be met.

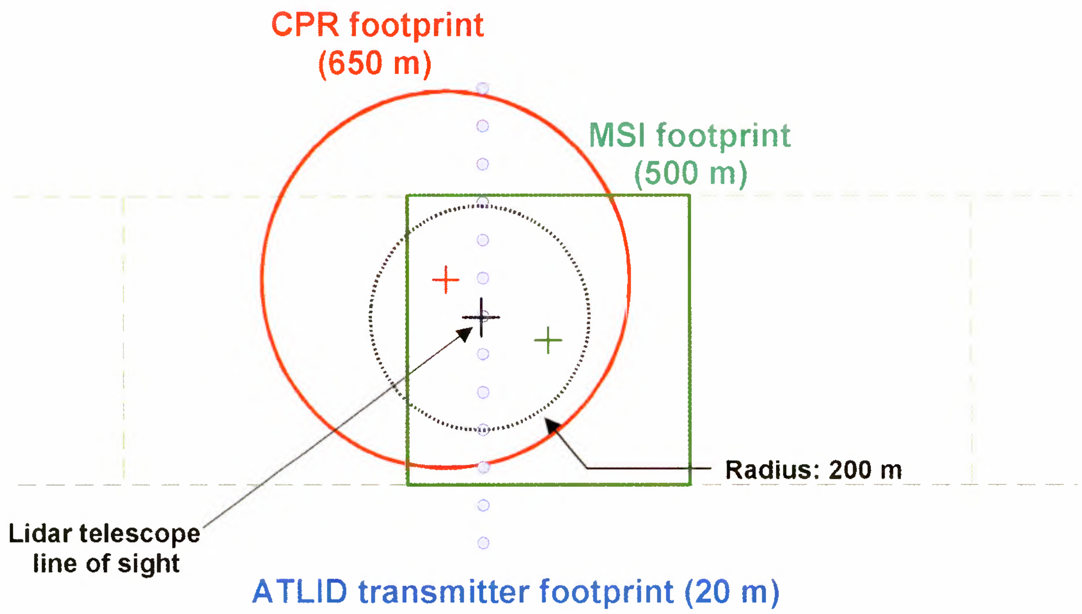

Figure 6.2: *EarthCARE instrument footprints. The lidar telescope's line of sight, projected to nadir is used a reference, the dashed circle representing the alignment error between the centres of the MSI's nadir pixel and the CPR's footprint.*

6.2.1 The Atmospheric Lidar (ATLID)

Instrument Objectives

ATLID is required to measure vertical profiles of optically thin cloud and aerosol layers, as well as the altitude of cloud boundaries. In addition it will discriminate the molecular backscatter (Rayleigh) from the aerosol and cloud particle returns (Mie). ATLID is designed to provide, with high resolution and accuracy, vertical sounding of the atmosphere from the ground up to 20 km altitude with 100 m vertical resolution.

Instrument Description

A single wavelength lidar with a High-Spectral Resolution (HSR) receiver separating Rayleigh (molecular) and Mie (cloud and aerosol particles) backscatter returns has been selected as the baseline. The selected wavelength is 355 nm. This wavelength allows relatively high pulse energy to be used without infringing on eye safety. This results in a small footprint of around 20 m, minimising the receiver telescope field of view and the solar background noise. An additional cross-polarisation channel is implemented.

Two concepts with similar performances have been proposed in the industrial pre-Phase-A studies. The main differences between the two concepts lie in the instrument architecture (monostatic/bistatic) and the detection chain.

A dual wavelength concept (355 nm/1064 nm) has also been investigated but has proved to be less efficient than the HSR concept.

Overview

Except for the instrument architecture, the instrument configuration proposed in both studies is very similar. The mechanical design is based on a decoupling between the optical structure and the main structure. The optical structure accommodates all elements that are critical with respect to alignment and stability, i.e. the optical bench, the telescope, the optical hardware and the laser chain bench. The main structure maintains the whole instrument and ensures the interface with the satellite. It also provides a load path between the service module and the CPR. The overall instrument configuration of one of the proposed concepts is depicted in Figure 6.3.

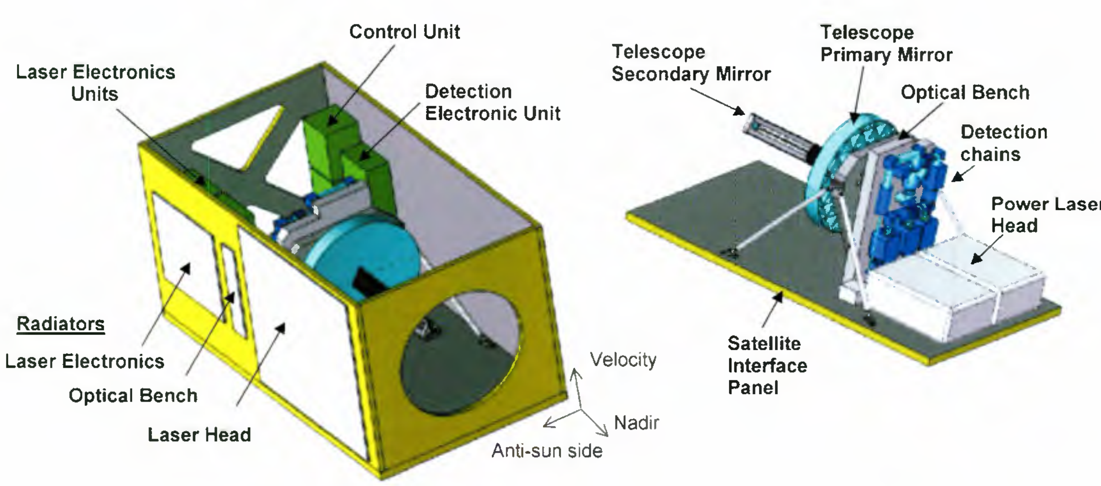

Figure 6.3*: ATLID instrument configuration (monostatic architecture). The units with critical alignment requirements are mounted on an isolated optical bench; the outer structure is designed as a load path for the CPR.*

The instrument is split into thermal blocks (decoupled from each other) where thermal constraints are similar. This leads to the following five thermal blocks:

1. Laser head
2. Optical bench

3. Telescope
4. Detection electronics
5. Laser power supply unit.

The laser head is the main contributor to the total power to be dissipated. A heat dissipation of up to 200 W is required with a specific temperature regulation (25°C ±1°C) of the laser head interface. The laser head is thermally insulated from instrument and platform via electrically conductive and thermally insulating washers and MLI blankets. Fluid loop heat pipes link the laser head cold plate to the radiator with a minimum temperature drop.

Transmitter

The HSR receiver requires a single frequency laser, whose line width is narrow compared to the frequency broadening due to Rayleigh scattering. An injection-seeded oscillator is then necessary. It is proposed to reuse the Aeolus/ADM type laser, ALADIN, which is a single frequency and tripled Ng:Yag laser. Compared to the ALADIN laser, the main difference is the lower energy required, which will allow a simplification of the laser design (17...35 mJ for ATLID compared to 150 mJ for ALADIN).

The laser passes through a beam expander to adapt the laser divergence to the required transmitter divergence. In the case of the bistatic configuration, active control of the laser transmitter pointing is foreseen, in the form a of tip/tilt mirror implemented before the beam expander.

Two laser heads are implemented for cold redundancy.

Receiver

The telescope is of a Cassegrain-like design with a real focal plane in which a field stop is located. The working principle of the transmitter and receiver for the monostatic configuration is depicted in Figure 6.4. A similar implementation of the receiver part is proposed for the bistatic configuration with slight differences with regard to the background filtering. The collected backscattered energy passes through the quarter-wave plate. Parallel and cross-polarisations are separated by the polarisation beam splitter. An interference filter rejects most of the background energy. After having gone through the field stop, the beam is filtered by the first Fabry-Pérot etalon. Mie and Rayleigh contributions are then separated by the HSR Fabry-Pérot etalon and imaged on their respective detection unit.

The detection chains aim at acquiring and processing the very low flux of UV photons in the three channels. For this reason, the detector must be able to work in photo-counting mode. Candidate detectors are the Accumulation CCD (ACCD) and

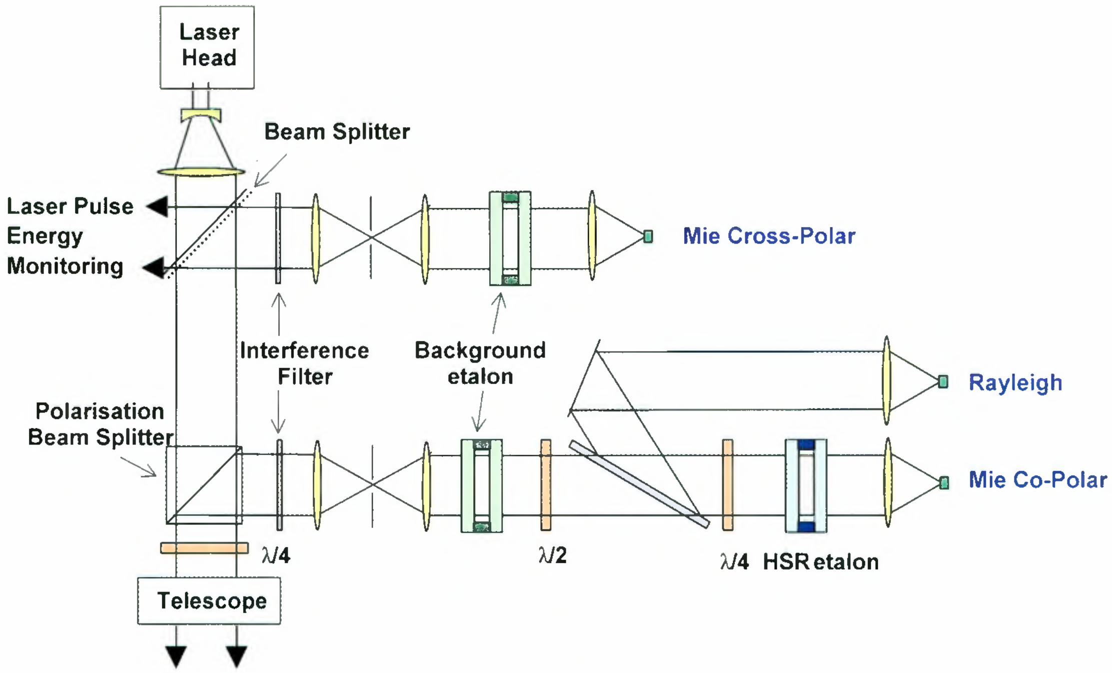

Figure 6.4: *ATLID receiver detection working principle (monostatic configuration); the background etalon together with the interference filter suppresses most of the background radiation. The HSR etalon separates the Mie and Rayleigh contributions.*

Photomultiplier Tube (PMT). Both detectors will benefit from ALADIN development activities.

The main characteristics of the instrument are given in Table 6.1.

Parameter	Unit	Concept A	Concept B
Architecture	-	Monostatic	Bistatic
Transmitter			
Pulse energy emitted at working wavelength	mJ	17	35
Pulse Repetition Frequency	Hz	100	70
Duty cycle	%	100	100
Spectral line width (FWHM)	MHz	< 30	< 30
Laser divergence, after beam expander	µrad	49	65
Receiver			
Telescope diameter	m	0.6	0.7
Background etalon (FWHM)	pm	46	38
HSR etalon (FWHM)	pm	0.52	0.21
Detector	-	ACCD	PMT

Table 6.1: *ATLID technical requirements*

Instrument Performance

The instrument performance is presented in Figure 6.5. The signal to noise ratio (SNR) is displayed as a function of altitude for both the Mie and Rayleigh signals. The simulation assumed daytime and a 1 km thick sub visible cirrus at 10 km altitude over a dense cloud deck (panel a) and aerosol over ocean (panel b). The full vertical resolution of 100 m is considered for the Mie channel, while data are accumulated in the vertical direction over 300 m for the Rayleigh channel. A horizontal integration length of 10 km is assumed for both channels. The requirements (SNR_{Mie}=2, $SNR_{Rayleigh}$=10) are met with good margins.

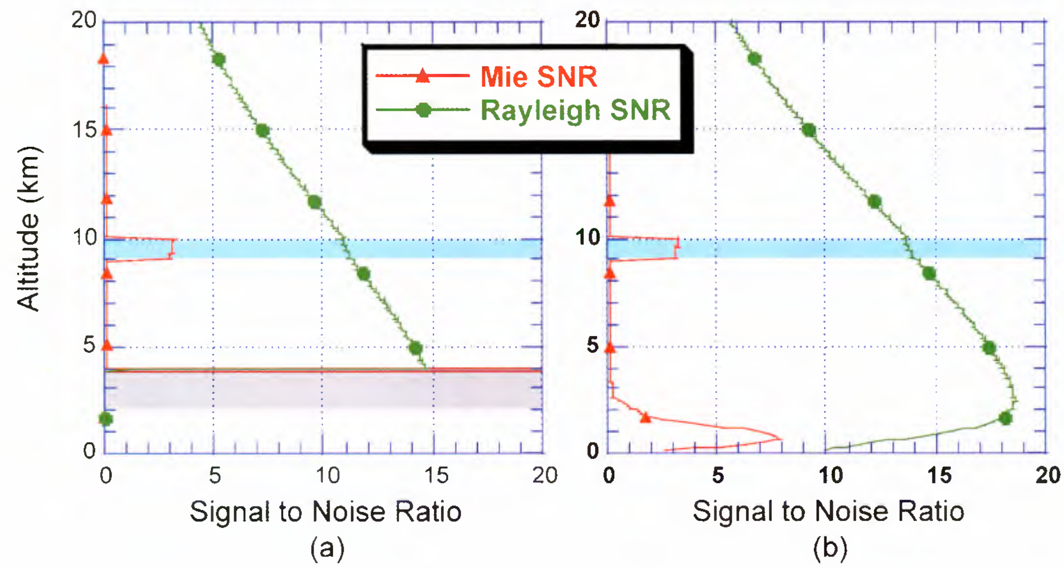

Figure 6.5: *ATLID signal to noise ratio as a function of altitude. A cirrus at 10 km (shown in light blue) is considered above (a) a very thick cloud (in grey) at 4 km and (b) above sea. The cirrus backscatter and extinction coefficients are* $\beta = 8\times10^{-7}\ m^{-1}\ sr^{-1}$ *and* $\alpha = 2\times10^{-5}\ m^{-1}$*, respectively. Vertical sampling is 100 m for both the Mie and Rayleigh curves. The requirement is a SNR of 2 for the Mie signal in the cirrus and an SNR of 10 for the Rayleigh.*

Instrument Development Status

The selected configuration benefits from the heritage of previous studies on ATLID and ALADIN pre-developments. For instance, the baseline laser is close to the ALADIN single frequency diode-pumped UV laser breadboard. Both ACCD and PMT with enhanced detection efficiency are in advanced stages of pre-development for ALADIN and can be adapted for the EarthCARE application. Fabry-Pérot etalons have been developed for the ATLID study as well as for the ALADIN pre-development.

6.2.2 Cloud Profiling Radar (CPR)

Instrument Objectives

The objective of the Cloud Profiling Radar (CPR) is to provide vertical profiles of cloud structures along the sub-satellite track. A unique feature of the CPR is the emission of microwave pulses that penetrate deep into lower cloud layers, which cannot be viewed by passive optical sensors or reached by the lidar. The CPR for EarthCARE is designed to attain a high sensitivity. In addition, a unique concept of Doppler measurement is newly introduced in this programme.

Instrument Description

Table 6.2 presents a summary of the CPR design.

Frequency	94.05 GHz
Polarisation	Linear or circular
Transmitter power	1800 W (peak)
Radar beam pointing	Fixed vertical (nadir)
Vertical range	-0.5 to 20 km
Vertical resolution	500 m
Horizontal resolution	~ 650 m across and 1 km along-track
Dynamic range of radar reflectivity factor	-38 dBZ to ≥ +30 dBZ (10 km integration)
Antenna aperture size	≤ 2.5 m diameter
Antenna beam footprint size	~650 m
Doppler measurement accuracy	≤ 1 m/s for cloud vertical motion

Table 6.2: *CPR design parameters.*

The lowest measurement altitude extends to -0.5 km in order to permit the use of surface backscatter for calibration purposes.

500 m vertical resolution corresponds to a 3.3 ms transmit pulse length. The effective vertical resolution, defined as the half-power width of the impulse response function, is 385 m. An optional mode with a higher vertical resolution (270 m effective), but with a degraded sensitivity (-35 dBZ), is also possible.

Along-track echo summation (integration) raises the radar sensitivity for clouds effectively. On-board echo summation is performed over a distance of 1 km (= along-track sampling). An integration distance of 10 km results in a sensitivity of better than -38 dBZ defined at the 10 km height without taking into account atmospheric attenuation.

An innovative feature of the CPR is the Doppler measurement of cloud particles. A principle of Doppler radar measurement is detection of the phase difference between echo signals from two consecutive radar pulses provided that the correlation between them is sufficiently high. The accuracy in Doppler velocity in the radial direction expected here is better than 1 m s^{-1}. A correction technique is proposed which uses the Doppler velocity estimate of the surface back-scatter as a zero-Doppler reference in order to cancel biases caused by variations in satellite attitude and altitude.

The system block diagram of the CPR is shown in Figure 6.6. The instrument consists of the following subsystems:

- The antenna reflector and antenna feed subsystem including a diplexer (circulator).
- The radio frequency (RF) subsystem including high power amplifiers (EIK: Extended Interaction Klystron), low noise amplifiers and redundancy switches.
- Frequency converter subsystem containing up- and down-conversion chains, pulse generator and frequency generator.
- The signal processing subsystem containing both logarithmic intensity detection and additional signal phase detection for the pulse-pair processing in the Doppler mode.

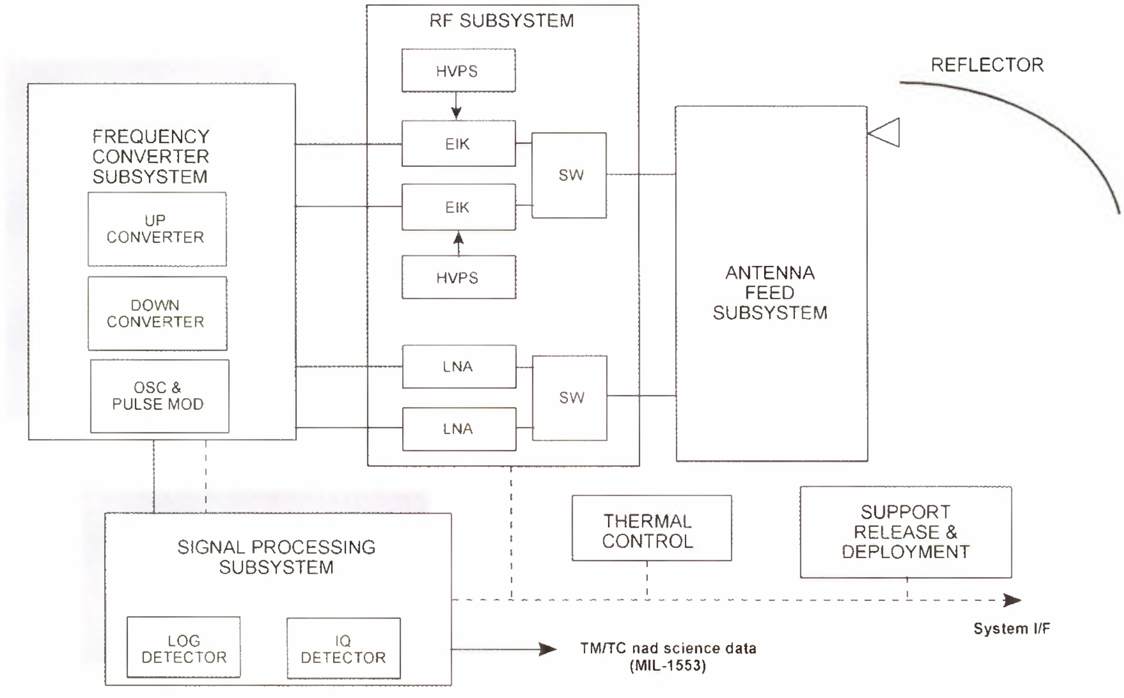

Figure. 6.6: *CPR block diagram showing all subsystems and the redundancy concept.*

Instrument Performance

The performance of the CPR is summarised in Table 6.3. The sensitivity estimate as a function of altitude is given for a single cloud layer under two types of model-atmospheres: Mean Annual Tropic and Summer Mid-Latitude.

Performance Parameter	Value		
Vertical resolution	500 m (385 m effective)		
Radiometric resolution	$\leq$ 1.44 dB		
Total radiometric accuracy	$\leq$ 1.7 dB		
Sensitivity [dBZ]	**Altitude [km]**	**Mean Annual Tropic atmosphere**	**Summer Mid-Latitude atmosphere**
	0.5	-34.8	-35.9
	1.0	-35.5	-36.2
	2.0	-36.7	-37.0
	4.0	-37.6	-37.7
	6.0	-37.9	-37.9
	8.0	-38.0	-38.0
	10.0	-38.0	-38.0
Doppler estimation accuracy	$\leq$ 1m/s for $Z \geq$ -31 dBZ		

Table 6.3: *Summary of CPR performance. The sensitivity is defined as the radar reflectivity factor for which the total radiomeric accuracy of 1.7 dB is achieved for an integration distance of 10 km.*

Instrument Development Status

The 94 GHz high power transmitter (EIK) for space use is being developed in Canada for CloudSat. For EarthCARE, a lifetime of more than three years needs to be achieved. Efforts in improving the EIK efficiency, which will bring longer lifetime, have been initiated to meet the EarthCARE requirements. A life test programme for cathode qualification has already started, and the feasibility of a high voltage pulsed power supply (HVPS) has been demonstrated.

As a part of a risk-retirement programme, the antenna feed and transmitter subsystems are being developed. The reflector with an aperture size of 2.5 m operating at millimetre wavelength also requires close attention. The reflector deployment concept and mechanisms are being studied.

6.2.3 The Fourier Transform Spectrometer (FTS)

Instrument Objectives

The FTS will provide spectrally resolved TOA LW fluxes and profiles of temperature and water vapour above clouds and in clear air.

Instrument Description

The EarthCARE FTS (Fourier Transform Spectrometer) instrument is a 4-port, L-arm dual pendulum type Michelson interferometer using corner cube mirrors. The Optical Path Difference (OPD) is 2 cm and the nominal unapodised spectral resolution is 0.5 cm^{-1}. The interferogram scan interval is 1.3 s. The interferometer beam diameter is 30 mm to provide high optical throughput. The sampling laser is a temperature stabilised solid state laser (1.55 μm).

Figure 6.7 shows the optical layout of the FTS.

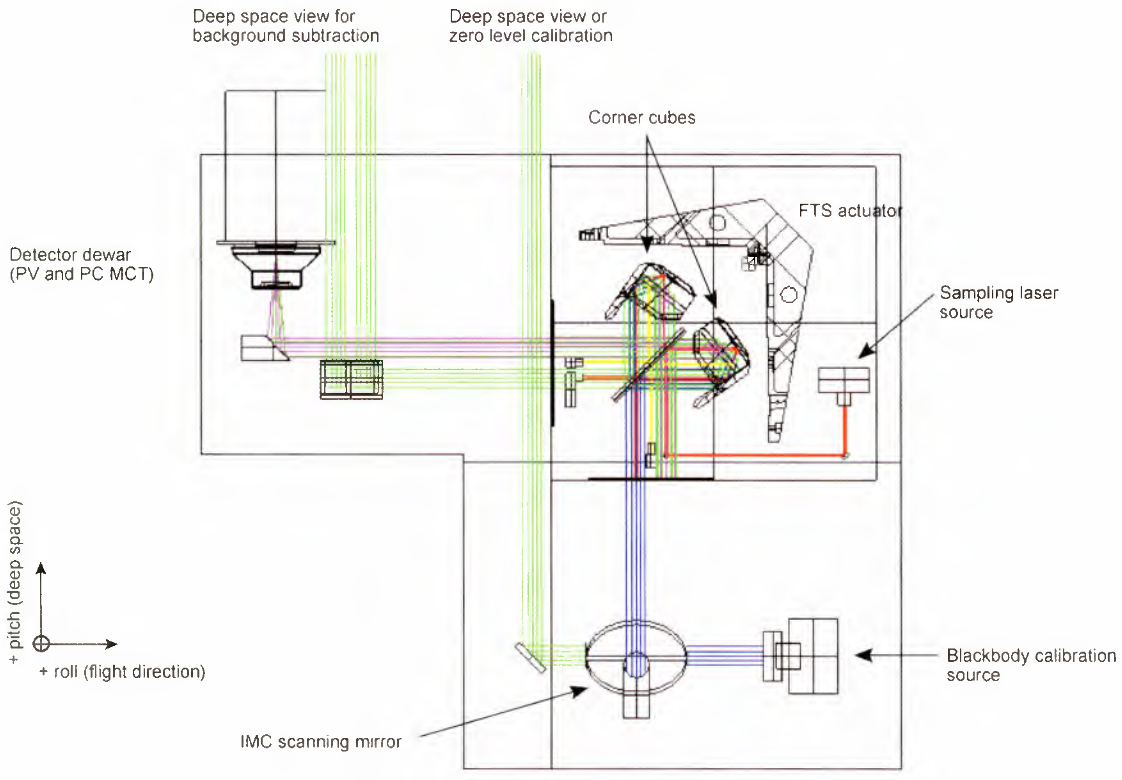

Figure 6.7: *Optical layout of the FTS instrument. The optical paths for the deep space views (background subtraction and zero level calibration) are shown in green. The Earth view is perpendicular to the drawing.*

The FTS has two bands, one for the 5.7 μm to 15 μm spectral range (Band 1), and another covering the 15 μm to 25 μm spectral range (Band 2). Band 1 will use a photo-voltaic HgCgTe (PV-MCT) detector for better linearity of the detector response. Band 2 will use a photo-conductive HgCdTe (PC-MCT) detector since no PV-MCT detector is available above 16 μm. Both detectors require cooling to 70 to 80 K using a Pulse Tube Cooler.

Using the 4-port design, the background emission from the FTS optics is subtracted (nadir signal – deep space signal), which will increase the signal dynamic range. Calibration will be performed both viewing deep space and a room temperature blackbody, because the two input ports for the nadir and the deep space view are not identical.

An Image Motion Compensation (IMC) mirror is used to cancel out the satellite velocity for the minimum scene variation requirement (1% in area during one interferogram scan). The scene variation due to the Earth's rotation (across track direction) will be cancelled out by the proper yaw manoeuvring of the satellite.

Band 2 looks at 20 km ahead of Band 1 which is looking towards nadir. The observation time difference, of 2.6 s, between Band 1 and 2 is small and negligible. The calibration scans (deep space and blackbody) will be acquired every 100 interferograms. Calibration will be performed separately for the two directions of the interferogram scans. At the beginning of the operation, a white light source (W lamp) is switched on for a short time and the centre burst position is determined for the diode laser sampling. After the centre burst determination, the FTS will operate continuously.

The main characteristics of the instrument are given in Table 6.4.

Instrument Performance

The instrument performance is presented in Table 6.5.

Instrument Development Status

This FTS design has a strong heritage from GCOM-A1/SOFIS (EM manufacturing stage) and ADEOS/IMG (1996–1997). A similar optical and mechanical design has been applied successfully both to SOFIS and SciSAT/ACE-FTS (Canada). Key issues required for the radiometric accuracy, such as calibration, instrument stability, onboard blackbody, and detector non-linearity correction, were already addressed for the IMG. Critical components, such as beam splitter, MCT detectors, 1.55 μm diode laser, FTS mechanical design and 70 K cooler, have already been evaluated and designed as engineering or flight models.

FTS Configuration	4-port interferometer. L-Arm Dual Pendulum with corner cube mirrors
Optical Path Difference, Spectral Resolution	± 2.0 cm, 0.5 cm^{-1} unapodized spectral resolution
Beam Diameter	30 mm circular
Band Configuration	Band 1: 5.7 μm-15 μm Band 2: 15 μm-25 μm
Detectors	Band 1: PV-MCT Band 2: PC-MCT
Interferogram Scan	1.3 second per interferogram Full both sides against centre burst, one-way Reverse scan used for observation of the next IFOV
Zero Path Difference Detection	White light using W lamp with cold redundancy
Sampling Reference Laser	1.55 μm diode laser with cold redundancy, < 10^{-5} μm stability. InGa detector
Beam Splitter	KBr (or CsI)

Table 6.4: *FTS design parameters.*

Wavelength (μm)	**NESR (μW/cm^2/sr/cm^{-1})**	**NEΔT @ 300 K (K)**	**SNR**
25	0.062	0.63	213
23	0.063	0.57	220
20	0.067	0.52	221
17	0.073	0.48	210
15	0.017	0.10	900
12	0.020	0.11	650
10	0.023	0.15	425
8	0.029	0.25	201
6	0.035	0.70	53

Table 6.5: *NESR and NEΔT performance of the FTS. The sudden change at 15 μm is due to the change of detector.*

6.2.4 Multi-Spectral Imager (MSI)

Instrument Objectives

The MSI is designed to provide images of the visible ('reflectance') and infra-red ('emitted') bands in support of the active instruments. It will provide scientific products for clouds and aerosols as well as the contextual information of the cloud and aerosol layers. The MSI will also be used for the calibration of the BBR. The instrument will look at nadir with a spatial resolution of 500 m and a swath width of 150 km.

Instrument Description

The instrument makes use of the push-broom concept, with three independent cameras, operating in the VNIR, SWIR and TIR bands. The spectral bands are in-field separated and defined by filters located in front of the detector arrays. The bands are listed in Table 6.6 and Figure 6.8 depicts the optical arrangement. The in-field separation principle implies that not all bands are registered at nadir at the same time. The resulting time difference is of the order of a few seconds, during which the state of the observed volume of atmosphere is considered not to change significantly. This registration principle entails some distortion at the extremes of the swath due to the rotation of the Earth. This effect is compensated at satellite level by the application of a yaw steering law, which will suitably offset the line of flight from the ground track.

Band	Spectral range(μm)	Comments
1	0.649-0.669	VIS
2	0.855-0875	NIR
3	1.580-1.640	SWIR 1
4	2.150-2.250	SWIR 2
5	8.3-9.4	TIR 1
6	10.4-11.3	TIR 2
7	11.4-12.3	TIR 3

Table 6.6: *MSI spectral bands.*

The VIS/NIR detectors are of the Si CCD type, whereas a cooled MCT array will be used for the SWIR bands. Uncooled micro-bolometers, which are under development now, will be employed as TIR detectors. The detectors will be complemented by front-end electronics containing the read-out electronics, pre-amplifiers and analogue-to-digital converters.

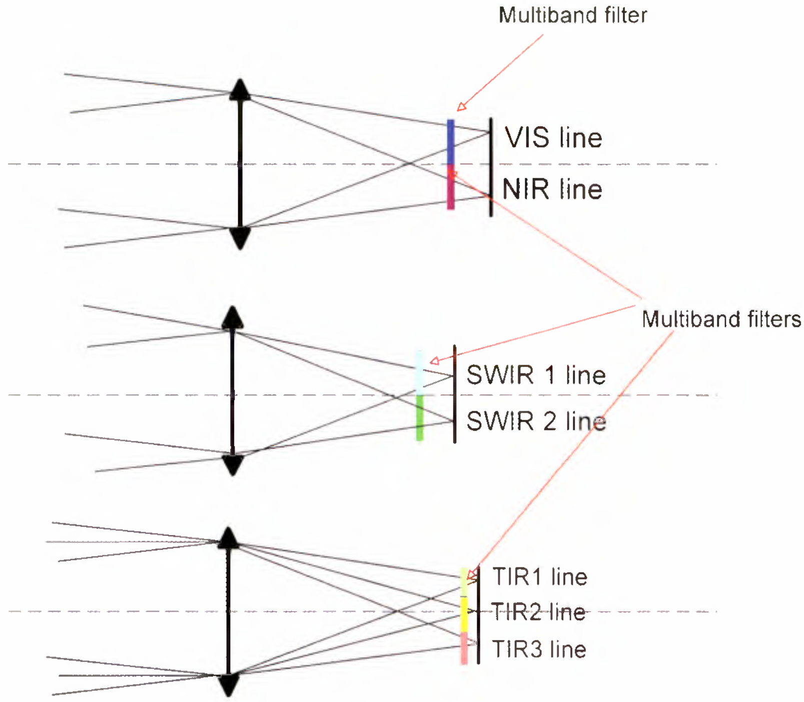

Figure 6.8: *MSI Spectral Band Configuration. All bands are in-field separated; dedicated cameras are used for the VNIR, SWIR and TIR spectral bands.*

Calibration is essential for meeting the radiometric performance requirements; a two-point method is foreseen for all channels. For the VIS/NIR and SWIR this will be done by means of a solar diffuser and a dark signal provided by the inside of the calibration mechanism. For the TIR bands this will be achieved by means of a cold space view and a blackbody.

The MSI consists of a single box containing all optical, electronic and mechanical elements. The fields-of-view need to be tightly controlled to ensure unobstructed Earth, Sun and deep space views. In addition, sufficiently large radiator areas must be available for heat dissipation and to provide a stable environment for the SWIR and TIR detectors.

The functional diagram of the MSI is shown in Figure 6.9.

Instrument Performance

The radiometric performance of the MSI is listed in Table 6.7.

Instrument Development Status

The instrument as such does not have a documented heritage. However, its various elements are either well known or the subject of detailed development. This applies in particular to the SWIR and TIR focal plane detectors. The results obtained so far confirm the basic assumptions and thus provide confidence for the listed performance parameters to be met.

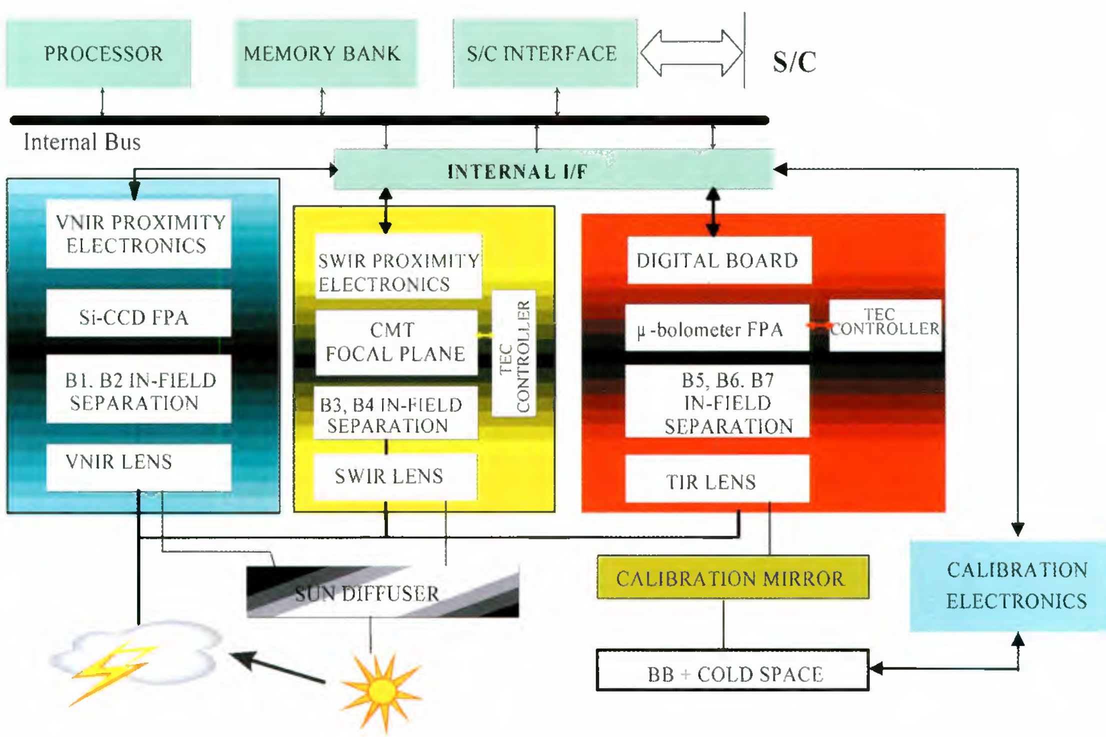

Figure 6.9: *MSI functional diagram; the three cameras are shown together with the calibration sources and the data processing electronics.*

Band	Specification	Performance	Comment
VIS	200 (400)	290	$\rho = 1$
NIR	200 (400)	280	$\rho = 1$
SWIR 1	200	290	$\rho = 1$
SWIR 2	200	280	$\rho = 1$
TIR 1	0.25 K	0.15 K	T = 293 K
TIR 2	0.25 K	0.18 K	T = 293 K
TIR 3	0.25 K	0.2 K	T = 293 K

Table 6.7: *MSI radiometric performance; Signal to noise performance is reported for the VIS, NIR, SWIR bands and NEΔT performance for the TIR bands.*

6.2.5 Broadband Radiometer (BBR)

Instrument Objectives

The BBR will provide estimates of the reflected short-wave (SW, 0.2–4 μm) and emitted long-wave (LW, 4–50 μm) fluxes at the top of the atmosphere (TOA).

Instrument Description

Whilst the instrument provides estimates of SW and LW radiance, the conversion to flux is performed analytically by means of the three along-track views. Furthermore, data supplied by the MSI will be used for calibration. The forward and backward views cover the scene with a zenith angle of 55 degrees, which is equivalent to an offset between the three telescopes of 50 degrees. The optical design provides for equal pixel sizes (10 km by 10 km) for all three views. There is no across-track swath.

The instrument is a two-channel radiometer, in which the LW channel is obtained by subtracting the SW component from a channel covering the complete spectral range. Dedicated telescopes are used for all views. They are mounted together in one block, allowing them to be moved also towards an internal black body simulator and external views for calibration. A channel selector revolves around the telescopes to modulate the incoming flux (as the detectors are only sensitive to alternating signals), and to generate the two spectral channels. The instrument configuration is shown in Figure 6.10.

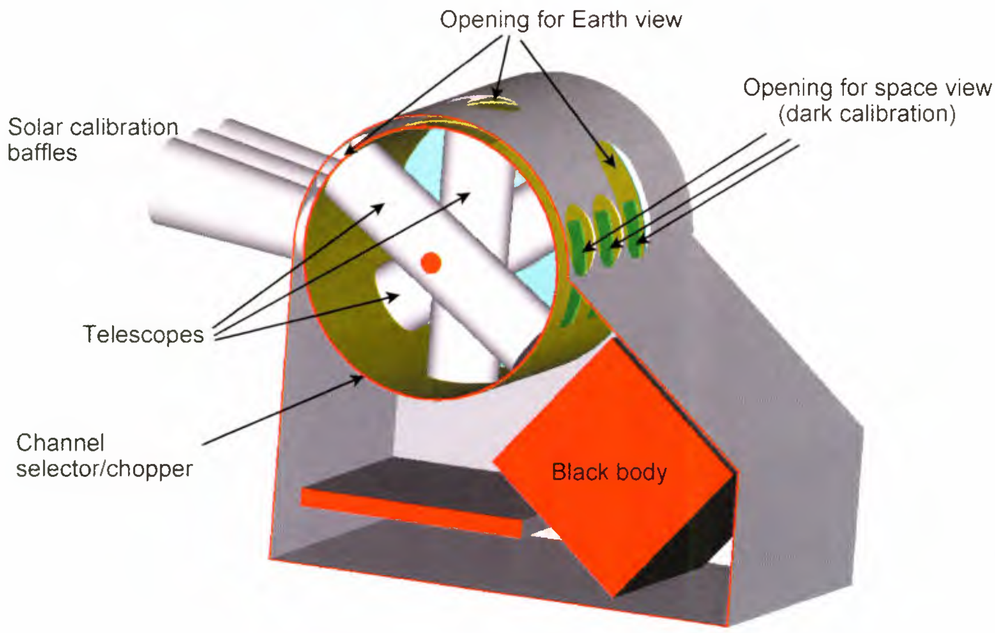

Figure 6.10: *BBR configuration. The three telescopes view the Earth in three different along-track directions: nadir, forward and backward. The channel selector is used to modulate the input flux of the pyro-electric detectors.*

Instrument Performance

Instrument performance is constituted by three contributions, i.e. the instrument proper, the scene identification or 'unfiltering' and the radiance to flux (mean case) conversion errors. They are listed in Table 6.8.

Error Contribution	**Flux Wm^{-2}**
Instrument	7.2
Unfiltering	2.6
Flux Conversion	4.0
Total (1σ)	8.7

Table 6.8: *BBR performance.*

Instrument Development Status

The BBR draws on the SCARAB heritage and development activities for the French-Indian Megha-Tropiques mission, as well as ERM.

6.3 Mission Profile

6.3.1 Orbit

The observation requirements call for a Sun-synchronous orbit and allow a rather wide range of node crossing times. Furthermore, there is no requirement for a specific orbit repeat cycle, other than a general preference for low repeat cycles to minimise the time between satellite passes during ground validation campaigns.

The orbit altitude is selected to be as low as possible in order to optimise the performance of the active instruments, compatible with the limitations on the propellant supply for orbit maintenance. The launch will take place in either 2008 or 2010. The worst case is constituted by the latter as it coincides with the maximum of the solar cycle. An altitude in the range 416–432 km has been identified as the best compromise.

A descending node crossing time of 10:30 hrs. has been selected for compatibility with the proposed companion satellite (GCOM-B1) in a dual launch scenario, as outlined in Section 6.5.

As a dual launch into low Earth orbit implies rather similar orbit characteristics for the two spacecraft, an insertion concept specific to this mission has been developed. *A priori*, the node crossing times should be very similar, otherwise a plane change manoeuvre would be necessary, requiring either a substantial amount of fuel or a long time using the natural precession of the orbit. The GCOM-B1 node crossing time of 10:30 hrs is perfectly acceptable for EarthCARE. Although both satellites will fly in Sun-synchronous orbits, their altitudes are different and thus also the orbit inclinations. Both satellites will be placed into an elliptical transfer orbit with an apogee at the proposed GCOM-B1 altitude (803 km) and a perigee at the EarthCARE altitude. Each satellite will then circularise its orbit individually. EarthCARE will also perform the necessary inclination change.

6.3.2 Communication Scenario

The communication scenario is based on a two-band concept with an S-band link for low-rate telemetry and telecommand transmissions and an X-band link for down-linking the science and housekeeping data. The aggregate instrument data rate is about 1 Mbit/s.

Assuming only four passes are used, a recorder capacity of 64 Gbit is required. Data accumulated during 7 orbits must be stored onboard, as they are not visible by the ground station.

6.3.3 Lifetime

Mission life is mainly determined by the propellant needed to maintain the orbit. The observation requirements call for a minimum of two years of in-orbit operations. Another year has been added to cater for commissioning and contingency operations. The predicted total velocity change for a mission during the solar maximum is of the order of 420 m s^{-1}.

6.4 Satellite Design

6.4.1 Configuration

The satellite configuration is constrained by the accommodation of the instruments, which all require an unobstructed Earth view. In some cases, deep space and occasional Sun views are also necessary for instrument calibration. The two active instruments with their rather high masses and volumes clearly drive the concept. Furthermore, sufficiently large areas need to be made available for the radiators to dissipate instrument heat.

For EarthCARE a distinction between service module and payload module does not appear justified. Therefore, a stacked configuration has been selected as a result of trade-offs covering mass, instrument accommodation and also assembly/integration considerations. Structural deformations resulting from manufacturing tolerances and in-orbit environment are minimised, as the load paths between the instruments are rather short. This will result in the co-registration requirements outlined in Section 6.2 to be met without resorting to complex design and manufacturing techniques.

The overall deployed configuration is shown in Figure 6.11.

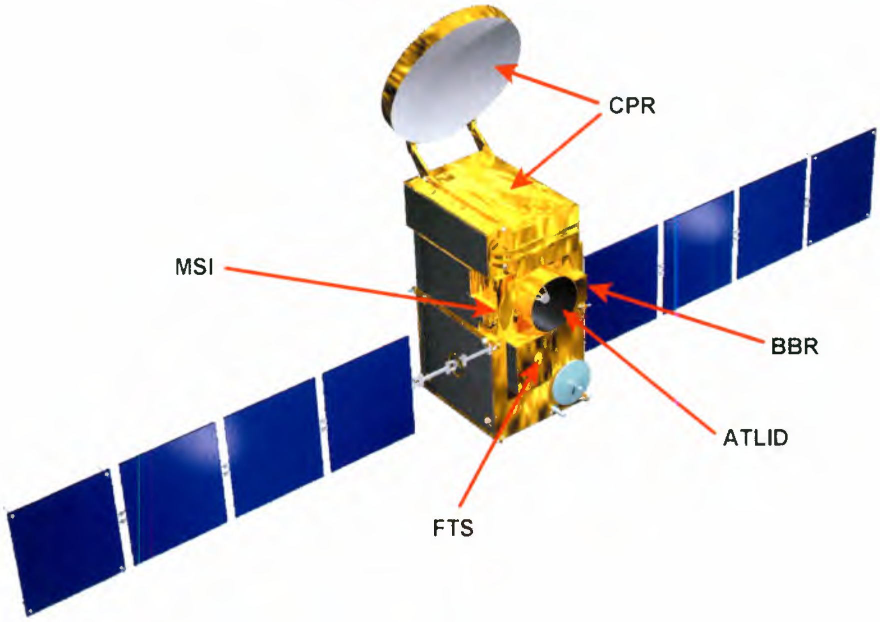

Figure 6.11: *EarthCARE configuration. The active instruments are accommodated on top of the service module, the passive ones on the nadir panels of the lidar and the service module.*

The service module interfaces with the launch vehicle in the anti-flight direction. It carries the two deployable solar array wings, the communication antennas and the FTS. The star trackers are mounted on the zenith panel. The lidar is mounted on its top panel and also supports the radar. In this way a short and stiff load path results, minimising inter-instrument alignment errors. The imager is accommodated on the anti-Sun side and the broadband radiometer on the nadir side. This concept respects all field-of-view requirements and also provides sufficient radiator area for thermal control.

The electrical architecture is depicted in Figure 6.12. It makes use of existing subsystem concepts.

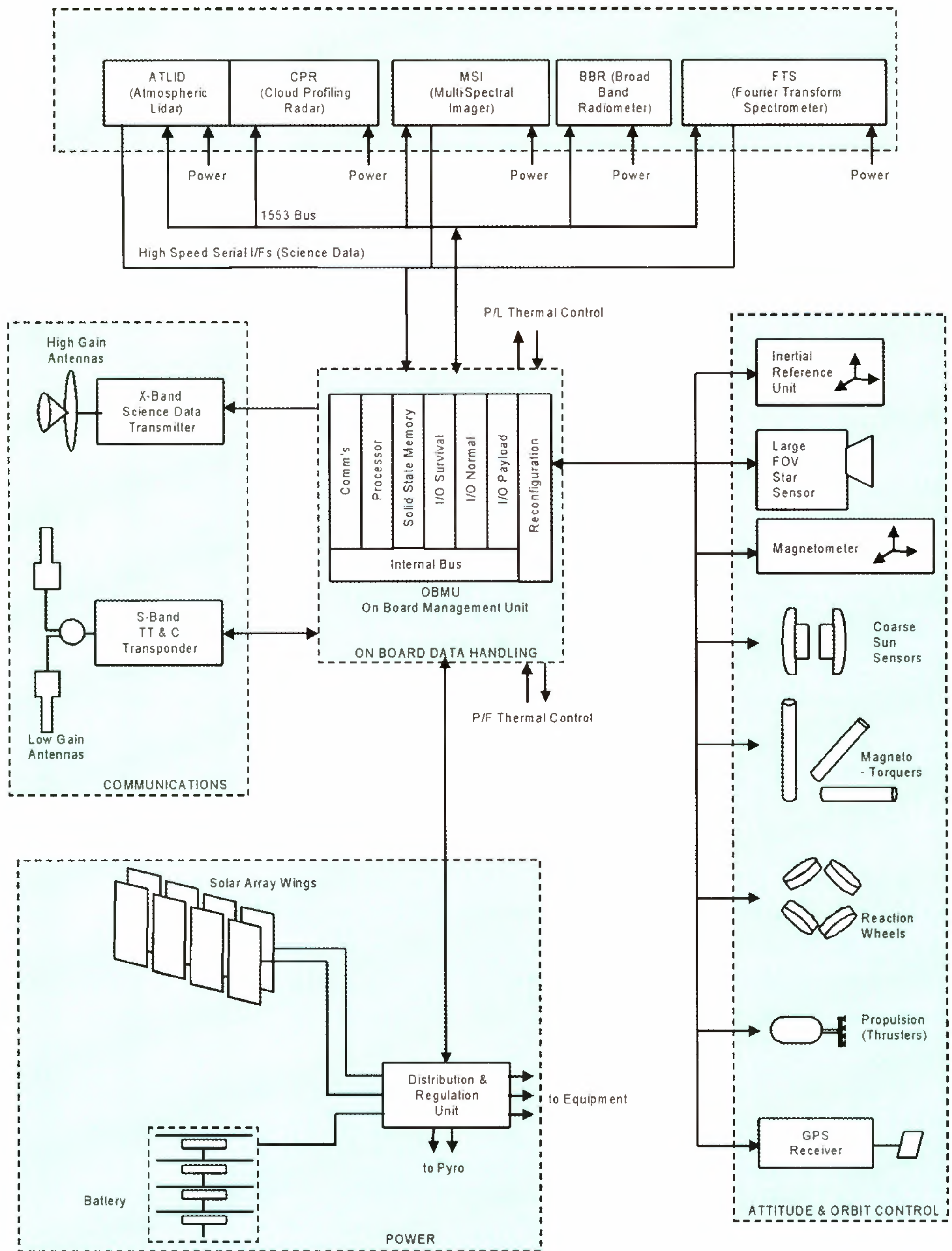

Figure 6.12: *EarthCARE electrical architecture; a centralised concept has been selected with standard data buses for subsystem control and data acquisition and distribution.*

6.4.2 Satellite Subsystems

The satellite structure consists essentially of three parts, i.e. the service module, the lidar and the radar. They are to a large degree independent, but the stiffness of the assembly must be compatible with the static and dynamic environment. Note that the lidar supports the CPR; its structure has therefore to be sized for these loads. Its optical bench is mechanically decoupled to maintain good alignment.

The service module is built around a central cylinder, which provides the primary load path with the launch vehicle. The propellant tank is housed inside. Shear walls and outer panels constitute the interface to the lidar and provide accommodation for the avionics units.

The thermal control subsystem is of a conventional passive design incorporating multi-layer insulation, paint and heaters where and when applicable. Analysis has shown that all units will be kept within reasonable temperature limits.

The envisaged propulsion system is a conventional mono-propellant system. Its design is mainly driven by the orbit injection and maintenance requirements, which require a tank of at least 420 litres. There is sufficient volume available inside the central cylinder to accommodate a tank volume of up to 600 litres. The thruster configuration consists of four 2 Newton units.

The attitude and orbit control subsystem is comprised of the sensors (star cameras, coarse Sun sensor, magnetometers, gyros and a GNSS receiver) and the actuators (reaction wheels, magneto-torquers and the thrusters). The thrusters are not employed for attitude control.

Earth pointing is maintained during nominal operations by the reaction wheels arranged in a tetrahedral configuration; they are de-saturated by a set of magneto-torquers. The information provided by the sensors is used to control the actuators during all operation modes from injection, to orbit control and maintenance to safe mode. The actuators are sized for worst case failures and disturbance torques.

Satellite yaw steering will be used to minimise co-registration errors of the multi-spectral imager.

The OBMU comprises all data management functions, including the processing of telemetry and telecommand data, acquisition and storage of science data, data routing to the communications subsystem and the control of all subsystems. The solid state data recorder, with an end-of-life capacity of 64 Gbit is also part of the OBMU.

The power subsystem is sized for a mainbus power of 1200 W, which translates into a solar array output requirement of 2500 W to cater for battery charging. The array area is to be kept as small as possible, to minimise drag which implies the use of high-efficiency solar cells. GaAs cells have been baselined. A derivative of an existing solar array with an area of about 9.5 m^2 will be used. Lithium-ion battery cells will be used. A capacity of 3780 Wh is necessary to limit the depth-of-discharge to 20% thereby ensuring adequate cycle life. An unregulated main bus system is foreseen, the parameters of which will be optimised for the proposed energy storage concept. All power system functions are centralised in the Distribution and Regulation Unit (DRU) which interfaces directly with the OBMU for the control of all electrical loads.

6.4.3 Resource Budgets

The mass and power budgets are given in Table 6.9. These data have been derived from the instrument and subsystem estimates. Global allocations have been made for system margins.

		Mass (kg)		Power (W)
Instrument		565		735
Lidar	235		250	
Radar	230		300	
Imager	15		45	
Broadband Radiometer	15		20	
Fourier Transform Spectrometer	70		120	
Service Module		415		280
Margin (~20%)		200		185
Satellite dry mass		1180		
Propellant		420		
Total		1600		1200

Table 6.9: *EarthCARE mass and power budgets.*

The propellant budget is shown in Table 6.10. It reflects the assumptions presented in section 6.4 concerning the launch concept and the orbit maintenance requirements.

	Velocity Increment (m/s)	Propellant Mass (kg)
Injection error	30	20
Inclination change	125	87
Circular orbit	105	73
Altitude maintenance	420	240
		420

Table 6.10: *EarthCARE velocity increment and propellant budget.*

The data rate budget is given in Table 6.11; it reflects the instrument baseline designs as described in Section 6.4.

	Data Rate (kbit/s)
Lidar	255
Radar	50
Imager	370
Broadband Radiometer	20
Fourier Transform Spectrometer	320
Total	1015

Table 6.11: *EarthCARE data-rate budget.*

6.5 Launch Vehicle

The Japanese H-IIA launch vehicle has been identified as the baseline option for the joint EarthCARE pre-Phase-A mission study. Its large fairing, which easily accommodates the EarthCARE satellite, renders it well-suited for this mission. A dual launch scenario, together with the Japanese GCOM-B1 satellite is foreseen, thus making optimum use of the available lift capability.

6.6 Ground Segment

A generic concept has been selected for the EarthCARE ground segment consisting of a Mission Operations and Satellite Control Element (MSCE), a Command and Data Acquisition Element (CDAE), a Processing and Archiving Element (PAE) and a Science Data Centre (SDC). It is expected to make full use of the Agency's existing assets. The block diagram of this concept is shown in Figure 6.13.

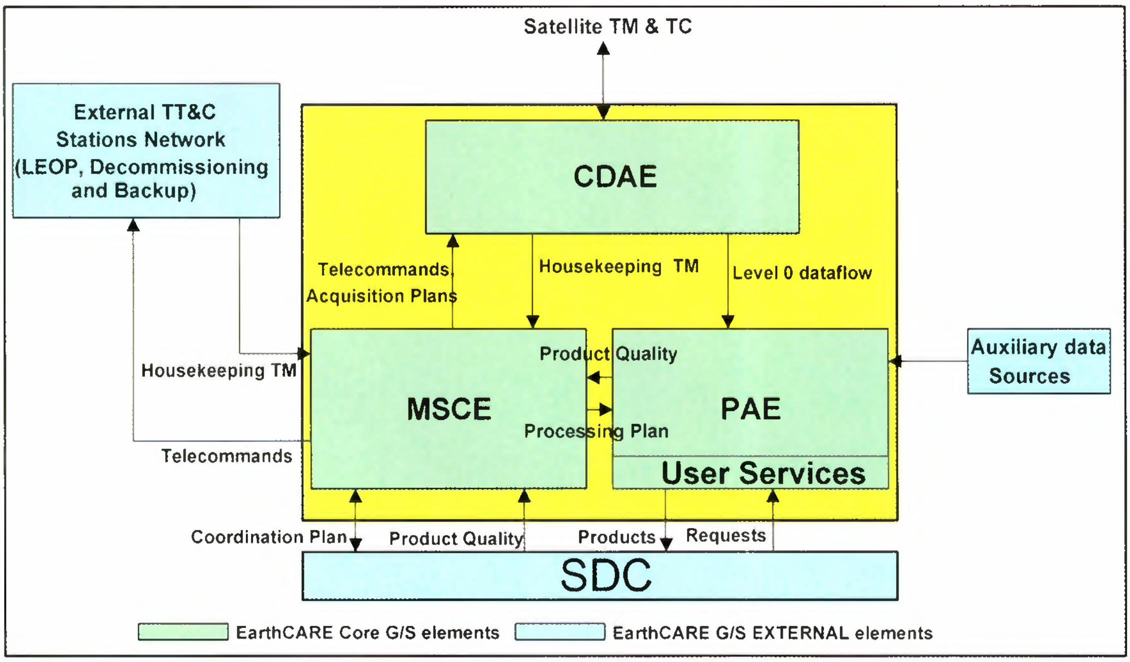

Figure 6.13: *EarthCARE ground segment concept, which reuses elements from other ESA missions.*

7 Programmatics

7.1 Introduction

Section 7.2 presents the technical maturity, the heritage and the risk areas for the concepts developed in the pre-Phase-A studies. Section 7.3 presents the envisaged international cooperation for EarthCARE and the related missions, both approved and planned. EarthCARE's contribution to enhancing the Earth observation capabilities and its application potential are outlined in Section 7.4.

7.2 Technical Maturity, Critical Areas and Risk

The technical maturity of the EarthCARE mission is consistent with a launch in 2008. The modular system design allows for the parallel development of instruments, platform and ground segment. Various past and on-going activities to pre-develop instruments and to validate related technologies provide strong confidence in the possibility to keep the number of instrument models to a minimum during the development phase. Some of these activities, e.g. for ATLID, span more than 10 years of pre-development effort. For the platform, strong heritage exists from the on-going Earth Explorers and other missions.

Table 7.1 summarises the main aspects of the implementation and the heritage of key payload elements.

The devices listed are not considered to present high development risks. Either space, military or commercial heritage exists, or dedicated development activities are in progress and expected to be completed before Phase C/D. At satellite development level the number of instruments to be embarked will require a well-planned development effort. The ground segment can be built upon the existing infrastructure developed for ERS and Envisat.

7.3 International Cooperation and Related Missions

Because of its expected role in collecting key information to understand the global climate and its change, EarthCARE is clearly of global interest and can play a major role in the international effort to further our understanding of atmospheric processes.

EarthCARE will be realised through an extensive cooperation between ESA, NASDA and CRL covering both technical and scientific areas. The benefits of this cooperation for the mission include:

- enhanced scientific return
- complementary user communities

- possibility to use the best technologies available in Europe and Japan
- strongly reduced costs for each Agency.

These benefits, already noted during earlier discussions in the framework of the ERM and ATMOS-B1, have been further substantiated during preparatory activities of EarthCARE. The cooperation scenario provides confidence that the financial constraints of the Earth Explorer programme will be met.

Element		Implementation	Heritage
ATLID			
	Laser	Nd:YAG, tripled	Aeolus
	Fabry-Pérot etalon		ATLID, Aeolus
	Thermal control	Fluid loop heat pipe	Stentor
CPR			
	Antenna	2.5 m diam., CFRP (Carbon Fibre Reinforced Plastic)	Communication satellites
	High Power Amplifier	EIK	Military, CloudSat
	Modulator		Breadboard completed
FTS			
	Interferometer	L-arm dual pendulum with corner cube mirrors	SOFIS
	Detector	PV-MCT, PC-MCT	SOFIS, IMG
	Cooler	Pulse tube cooler	SOFIS
MSI			
	SWIR detector	Cooled MCT	Development in progress
	TIR detector	Micro-bolometers	Development in progress
BBR			
	Instrument concept	Three-telescope concept	SCARAB

Table 7.1: *Main aspects of the implementation and the heritage of key payload elements*

For the technical implementation, ESA is currently expected to contribute the platform, the ground segment and three instruments, namely ATLID, BBR and MSI, while NASDA and CRL are currently expected to contribute two instruments, namely CPR and FTS, and the launch. For the latter the identified baseline is to launch EarthCARE with a dual-launch using the H-IIA launcher, the co-passenger being the proposed

Japanese GCOM-B1 mission. Back-up alternatives have also been identified. The cooperation scenario will be consolidated during the joint Phase-A of the mission.

ESSP3-CENA (carrying a lidar) and CloudSat (carrying a cloud radar) are planned to be launched in the first half of 2004. These two missions, with expected lifetimes of 3 years, will provide a useful first step for the determination of the vertical profiles of aerosol and clouds. However they will not be able to provide the necessary closure of the Earth's energy budget required by climate and weather prediction systems. From this point of view, the timing of the ESSP3-CENA, CloudSat and EarthCARE missions will be very favourable.

EarthCARE will provide the cloud feedback constraints essential for an improved climate change prediction before the end of the reference period of the Kyoto protocol.

7.4 Enhancement of Capabilities and Potential for Applications

EarthCARE will be the result of a long development effort by Europe, Japan and Canada on novel lidar and radar technologies. The instruments embarked on EarthCARE are all expected to have an operational potential in future weather and climate monitoring missions.

The enhanced understanding of processes involving clouds and aerosols provided by EarthCARE will pave the way to improved exploitation of the data from geostationary and polar imagers/sounders of future meteorological systems. In this respect, the algorithm development and data assimilation work in support of EarthCARE will also contribute to such an improvement.

References

3D-CLARE, 1999: Three-Dimensional Cloud-Aerosol-Radiation Budget Experiment, Proposal of ATMOS-B1 Mission, ATMOS-B1 Team, CEOS, Earth Science and Technology Forum, Earth Science & Technology Organization, 99P0A1-D011.

Ackerman S.A., C.C. Moeller, K.I. Strabala, H.E. Gerber, L.E. Gumley, W.P. Menzel, and S-C. Tsay, 1998: Retrieval of effective microphysical properties of clouds: A wave cloud case study, *Geophys. Res. Lett.*, 25, No. 8, 1121-1124.

Andreae, M.O., W. Elbert, and S.J. de Mora, 1995: Biogenic sulfur emissions and aerosols over the tropical South Atlantic 3. Atmospheric Dimethylsulfide, aerosols and cloud condensation nuclei, *J. Geophys. Res.*, 100, 11,335-11, 356.

Arking, A. 1991: The radiative effects of clouds and their impact on climate. *Bull. Amer. Meteor. Soc.*, 71, 795-813.

Barkstrom B. R., E. F. Harrison, G. L. Smith, R. Green, J. Kibler, R. D. Cess, and the ERBE Science Team, 1989: Earth Radiation Budget Experiment (ERBE) archival and April 1985 results. *Bull. Amer. Meteor. Soc.*, 70, 1254-1262.

Brown, P.R.A., A.J. Illingworth, A.J. Heymsfield, G.M. McFarquhar, K.A. Browning, and M. Gosset, 1995: The Role of Spaceborne Millimetre-Wave Radar in the Global Monitoring of Ice Cloud, *J. Appl. Meteor.*, 34, 2346-2366

Cess, R.D., G.L. Potter, J.-P. Blanchet, G.J Boer, A.D. DelGenio, M. Deque, V. Dymnikov, V. Galin, W.L. Gates, S.J. Ghan, J.T. Kiehl, A.A. Lacis, H. Le Treut, Z.-X. Li, Z.-X. Liang, B.J. McAvaney, V.P. Meleshko, J.F.B. Mitchell, J.-J. Morcrette, D.A. Randall, L. Rikus, E. Roekner, J.-F. Royer, U. Schlese, D.A. Scheinin, A. Slingo, A.P. Sokolov, K.E. Taylor, W.M. Washington, R.T. Wetherald, I. Yagai, and M.-H. Zhang, 1990: Intercomparison and interpretation of climate feedback processes in 19 general circulation models. *J. Geophys. Res.*, 95, 16601-16615

Cess, R.D., M.H. Zhang, W.J. Ingram, G.L. Potter, V. Alekseev, H.W. Barker, E. Cohen-Solal, R.A. Colman, D.A. Dazlich, A.D. Del Genio, M.R. Dix, V. Dymnikov, M. Esch, L.D. Fowler, J.R. Fraser, V. Galin, W.L. Gates, J.J. Jack, J.T. Kiehl, H. Le Treut, K. K.-W. Lo, B.J. McAvaney, V.P. Meleshko, J.-J. Morcrette, D.A. Randall, E. Roeckner, J.-F. Royer, M.E. Schlesinger, P.V. Sporyshev, B. Timbal, E.M. Volodin, K.E. Taylor, W. Wang, and R.T. Wetherald, 1996: Cloud feedback in atmospheric general circulation models: An update. *J. Geophys. Res.*, 101D, 12791-12794.

Chahine, M.T., 1992: The hydrological cycle and its influence on climate, *Nature*, 359, 373-380

CLARE'98: CLARE – Cloud lidar and radar experiment, *ESA Contract No. 12957/98/NL/GD*

Derrien, M., B. Farki, L. Harang, H. LeGleau, A. Noyalet, D. Pochic and A. Sairouni, 1993: Automatic cloud detection applied to NOAA-11/AVHRR imagery, *Rem. Sens. Environ.*, 46, 246-267

Donovan, D.P. and A.C.A.P. van Lammeren, 2001a: First Ice-Cloud effective particle size parameterization based on combined lidar and radar data, submitted to *Geophys. Res. Lett.*

Donovan, D.P. and A.C.A.P. van Lammeren, 2001b: Cloud effective particle size water content profile retrievals using combined lidar and radar observations. Part I: Theory and simulations. Accepted for publication in Journal of Geophysical Research, Atmospheres.

Donovan, D.P., A.C.A.P. van Lammeren, R.J. Hogan, H.W.J. Russchenberg, A. Apituley, P. Francis, J. Testud, J. Pelon. M. Quante and J. Goddard, 2001. Cloud effective particle size water content profile retrievals using combined lidar and radar observations. Part II: Comparison with IR radiometer and in-situ measurements of ice clouds. Accepted for publication in Journal of Geophysical Research, Atmospheres.

Durkee, P.A., F. Pfeil, E. Frost and R. Shema, 1991: Global analysis of aerosol particle characteristics, *Atmos. Environ.*, 25A, 2457-2471.

Duvel, J. Ph., M. Viollier, P. Raberanto, R. Kandel, M. Haeffelin, L.A. Pakhomov, V.A. Golovko, J. Mueller, R. Stuhlmann, and the International ScaRaB Scientific Working Group, 2001: The ScaRaB-RESURS Earth radiation budget dataset and first results. *Bull. Amer. Meteor. Soc.*, in press.

European Space Agency,1998: The Science and Research Elements of ESA's Living Planet Programme, ESA SP-1227, 105pp.

Feichter, 2000: Atmospheric chemistry and aerosol dynamics. Numerical Modeling of the Global Atmosphere in the Climate System. Edited by P. Mote and A. O'Neill, 353-374

Fouquart, Y., J. C. Buriez, M. Herman, and R. S. Kandel, 1990: The influence of clouds on radiation: a climate-modeling perspective. *Rev. Geophys.*, 28, 145-166.

Geleyn, J.-F. and A. Hollingsworth, 1979 : An economical analytical method for the computation of the interaction between scattering and line absorption in radiation, *Beitr. Phys. Atmos.*, 52, 1-16

Goloub, P., D. Tanré, J.L. Deuzé, M. Herman, A. Marchand, and F. M. Bréon, 1999: Validation of the first algorithm applied for deriving the aerosol properties over the ocean using the POLDER/ADEOS measurements. *IEEE Trans. Geosci. Remote Sensing*, 37 , 1586-1596.

Han, Q., W. B. Rossow, and A.A. Lacis, 1994: Near-global survey of effective droplet radii in liquid water clouds using ISCCP data. *J. Climate*, 7, 465-497.

Hansen, J., M. Sato, R. Ruedy, A. Lacis, and V. Oinas 2000: Global warming in the 21st century: and alternative scenario. *Proc. Natl. Acad. Sci.*, 97, 9875-9880

Harries, J. E., Helen E. Brindley, Pretty J. Sagoo, Richard J. Bantges , 2001, Increases in greenhouse forcing inferred from the outgoing longwave radiation spectra of the Earth in 1970 and 1997, *Nature* 410, 355 - 357 (15 March 2001)

Hess, P. Keopke, and I. Schult, 1998: Optical properties of aerosols and clouds : the software package OPAC. *Bull. Amer. Meteor. Soc.*, 79, 831-844

Heuvel, J. C. van den , M. L. Driesenaar and R. J. L. Lerou, Fractal Properties and denoising of lidar signals from cirrus, J Geophys Res, 105, 3975-3982, 2000.

Heymsfield, A.J. and L.J. Donner, 1990: A scheme for parameterisating ice cloud water content in general circulation models, *J. Atmos. Sci.*, 47, 1865-1877.

Higurashi, A., T. Nakajima, B. N. Holben, A. Smirnov, R. Frouin, B. Chatenet, 2000: A study of global aerosol optical climatology with two channel AVHRR remote sensing, *J. Climate*, 13, 2011-2027.

Hogan R.J., and A.J. Illingworth, 2000: Deriving cloud overlap statistics from radar. Quart. *J. Roy. Meteor. Soc.*, 126, 2903-2909

Hogan R.J., C. Jakob, A.J. Illingworth, 2001: Comparison of ECMWF winter -season cloud fraction with radar-derived values. *J Appl. Met.*, 40, 513-525.

House, F. B., A. Gruber, G. E. Hunt, and A. T. Mecherikunnel, 1986: History of satellite missions and measurements of the Earth Radiation Budget. *Rev. Geophys.*, 24, 357–377.

Husar, R.B., J.M. Prospero, and L.L. Stowe, 1997: Characterisation of tropospheric aerosols over the oceans with the NOAA advanced very high resolution radiometer optical thickness operational product, *J. Geophys. Res.*, 102 (D14), 16, 889-16, 909

Intrieri J.M., G.L. Stephens, W.L. Eberhard, and T. Uttal, 1993: A method for determining cirrus cloud particle size using lidar and radar backscatter technique, *J. Appl. Meteor.*, 32, 1074-1082.

IPCC, 2001. Intergovernmental Panel on Climate Change, Third Assessment Report, WG I Climate Change 2001: The Scientific Basis, Summary for Policy Makers.

IPCC TS, 2001, Intergovernmental Panel on Climate Change, Third Assessment Report, WG II Climate Change 2001: Impacts, Adaptation and Vulnerability, Technical Summary

Jacobson, M. Z. 2001: Strong radiative heating due to the mixing state of black carbon in atmospheric aerosols. *Nature*, 409, 695-697.

Jakob, C., 1995: The impact of the new cloud scheme on ECMWF's Integrated Forecasting System (IFS). Proceedings of ECMWF/GEWEX Workshop on Modelling, Validation and Assimilation of clouds, November 1994, ECMWF, Reading (U.K.), 277-294.

Janiskova, M., 2001: Preparatory studies for the use of observations from the Earth Radiation Mission in Numerical Weather Prediction, ECMWF Contract Rep. to ESA, *Cnt. 13151/98/NL/GD*

Kandel R., M. Viollier, P. Raberanto, J. Ph. Duvel, L.A. Pakhomov, V.A. Golovko, A.P. Trishchenko, J. Mueller, E. Raschke, R. Stuhlmann, and the International ScaRaB Scientific Working Group (ISSWG) 1998:. The ScaRaB Earth Radiation Budget Dataset, *Bull. Amer. Meteor. Soc.*, 79, 765-783.

Kessler, E., 1969: On the distribution and continuity of water substance in atmospheric circulation. Meteorolog. Monog., 10, *American Meteor. Soc.*, Boston, Mass.

King, M. D., Y. J. Kaufman, W. P. Menzel, and D. Tanre, 1992: Remote sensing of cloud, aerosol, and water vapor properties from the Moderate Resolution Imaging Spectrometer (MODIS). *IEEE Trans. Geosci. Remote Sensing*, 30, 2-27.

Kriebel K.T., R.W. Saunders, and G.Gesell 1989: Optical properties of clouds derived from fully cloudy AVHRR pixels, *Beitr. Phys. Atmosph.*, 62, 165-171

Kristjansson, J.E., J.M. Edwards, and D.L. Mitchel, 2000: Impact of a new scheme for optical propoerties of ice crystals on climates of two GCMs, *J. Geophys. Res.*, 105, 10,063-10,079.

Lammeren, A.C.A.P. van and A.J. Feijt (1997). The emissivity of Cirrus clouds derived from LITE and Meteosat measurements. Selected Papers of the 18th International Laser Radar Conference (ILRC), Berlin 22-26 July 1996, published by Springer Verlag New York-Berlin-Heidelberg (ISDN 3-540-61887-2) pp. 201-204.

Le Treut, H. and B. McAvaney, 2000: Equilibrium climate change in response to a CO_2 doubling: an intercomparison of AGCM simulations coupled to slab oceans. *Technical Report , Institut Pierre Simon Laplace*, 18, 20 pp. 27

Lindzen, R. 1990: Some coolness regarding global warming. *Bull. Amer. Meteor. Soc.*, 71, 288-299.

Liu, Z., I. Matsui and N. Sugimoto, 1999: High-spectral-resolution lidar using an iodine absorption filter for atmospheric measurements, *Opt. Eng.*, 36(10), 1661-1670.

Mace G G, K. Sassen, S. Kinne and T P Ackerman 1998: An examination of cirrus cloud characteristics using data from millimetre wave radar and lidar: The 24 April SUCCESS case study, *Geophys. Res. Lett.*, 25, 1133-1136.

Mahfouf, J.-F., A. Beljaars, A. Chevalier, D. Gregory, C. Jakob, M. Janiskova, J.-J. Morcrette, J. Teixeira and P. Viterbo, 1999: The importance of the Earth radiation Mission for numerical weather prediction. ECMWF Technical Memorandum, 288, 77pp.

Minnis, P., and E.F. Harrison, 1984: Diurnal variability of regional cloud and clear-sky radiative parameters derived from GOES data. Part I: Analysis method, *J. Climate Appl. Meteor.*, 23, 993-1011.

Mitchel, D.L., Steven K. Chai, Yangang Liu, Andrew J. Heymsfield, Yayi Dong, 1996: Modelling cirrus clouds. Part I: Treatment of bi-modal size-spectra and case analysis, *J. Atmos. Sci.*, 53, 2952-2966.

Morcrette, J.-J. and C. Jakob, 2000: The response of the ECMWF model to changes in the cloud overlap assumption. *Mon. Wea. Rev.*, 128, 1707-1732

Nakajima, T. and T. Nakajima, 1995: Wide area determination of cloud microphysical properties from NOAA AVHRR measurements for FIRE and ASTEX regions, *J. Atmos. Sci.*, 52, 4043-4059.

Nakajima, T., and A. Higurashi, 1998: A use of two-channel radiances for an aerosol characterization from space. *Geophys. Res. Lett.*, 25, 3815-3818.

Nakajima, T., A. Higurashi, K. Kawamoto, and J. E. Penner, 2001: A possible correlation between satellite-derived cloud and aerosol microphysical parameters. *Geophys. Res. Lett.*, 28, 1171-1174.

Okamoto, H., S. Iwasaki, M. Yasui, H. Horie, H. Kuroiwa and H. Kumagai, 2000: 95 GHz cloud radar and lidar systems: preliminary results of cloud microphysics, *Proc. SPIE*, 4152, 355-363.

Ou, S.C. and K.-N. Liou, 1995 : Ice microphysics and climate temperature feedback. *Atmos. Res.*, 35, 127-138

Pelon J., C. Flamant, V. Trouillet and P.H. Flamant, 2000: Optical and nicrophysical parameters of dense stratocumulus clouds during mission 206 of EUCREX'94 as retrieved from measurements made with the airborne lidar LEANDRE, *Atmos. Res.*, 55, pp. 47-64.

Platt C.M., S.A. Young, A.I. Carswell, S.R. Pal, M.P. McCormick, D.M. Winker. M. DelGuasta, L. Stefanutti, W.L. Eberhard, M. Hardesty, P.H. Flamant, R. Valentin, B. Forgan, G.G. Gimmestad, H. Jäger, S.S. Khmelevtsov, I. Kolev, B. Kaprieolev, Daren Lu, K. Sassen, V.S. Shamanaev, O. Uchino, Y. Mizuno, U. Wandinger, C. Weitkamp, A. Ansmann, and C. Wooldridge, 1994: The Experimental Cloud Lidar Pilot Study (ECLIPS) for Cloud Radiation research. *Bull. Am. Meteor. Soc.*, 75, 1635-1654.

Ramanathan, V., R. D. Cess, E. F. Harrison, P. Minnis, B. R. Barkstrom, E. Ahmad, and D. Hartmann, 1989: Cloud-radiative forcing and climate: results from the Earth Radiation Budget Experiment. Science, 243, 57-63.

Raval, A. and V. Ramanathan, 1989: Observational determination of the greenhouse effect. *Nature*, 342, 758-761.

Robock, A., 2000 : Volcanic eruptions and climate. *Rev. Geophys.*, 38, 191-219.

Rossow, W.B., and L.C. Garder, 1993: Cloud detection using satellite measurements of infrared and visible radiances for ISCCP, *J. Climate*, 6, 2341-2369

Rossow, W. B., and R. A. Schiffer, 1999: Advances in Understanding Clouds from ISCCP. *Bull. Amer. Meteor. Soc.*, 80, 2261–2288.

Satheesh, S.K., and V. Ramanathan, 2000. Large differences in tropical aerosol forcing at the top of the atmosphere and Earth's surface. *Nature*, 405, 60-63.

Schmetz J., 1989: Towards a surface radiation climatology: Retrieval of downward irradiances from satellite. *Atmos. Res.*, 23, 287-321

Senior, C. A., and J. F. B. Mitchell, 1993 : Carbon dioxide and climate: the impact of cloud parameterization, *J. Climate*, 6, 393-418.

Slingo, J.M., 1980: A cloud parametrization scheme derived from GATE data for use in a numerical model. *Quart. J. Roy. Meteor. Soc.*, 106,747-770

Slingo, A. and H.M. Schrecker, 1982: On the shortwave radiative properties of stratiform water clouds, *Quart. J. Roy.. Meteor. Soc.*, 108, 407-426.

Slingo J.M., and A. Slingo, 1988: The response of a general circulation model to cloud long-wave radiative forcing. I: Introduction and initial experiments. *Quart. J. Roy. Meteor. Soc.*, 114, 1027-1062.

Smith, R.N.B., 1990: A scheme for prediction layer clouds and their water content in a general circulation model. *Quart. J. Roy. Meteor. Soc.*, 116,435-460

Sommeria, G. and J.W. Deardorff, 1977: Subgrid-scale condensation in models of non-precipitating clouds. *J. Atmos. Sci.*, 34, 344-355

SRES, 2000: Special Report of the Intergovernmental Panel on Climate Change, N. Nakicenovic and R. Swart (Eds.), *Cambridge University Press*, UK. pp 570

Stenchikov, G.L., I. Kirchner, A. Robock, H.-F. Graf, J.C. Antuna, R.G. Grainger, A. Lambert, and L. Thomason, 1998: Radiative forcing from the 1991 Mount Pinatubo volcanic eruption. *J. Geophys. Res.*, 103 (D12), 13837-13857.

Stephens, G.L., 1978: Radiation profiles in extended water clouds. *I. Theory. J. Atmos. Sci.*, 35, 2111-2122

Stephens, G.L, Ackermann, S. and E.A. Smith,1984: A shortwave parameterization revised to improve cloud absorption. *J. Atmos. Sci*, 41, 687-690

Stephens G.L., S.C. Tsay, P.W. Stackhouse, and P.J. Flateau, 1990: The relevance of the microphysical and radiative properties of cirrus clouds to climate and climatic feedback, *J. Atmos. Sci.*, 47, 1742-1753.

Stott, P. A., S. F. B. Tett, G. S. Jones, M. R. Allen, J. F. B. Mitchell, and G. J. Jenkins, 2000: External control of 20th century temperature by natural and anthropogenic forcings. *Science*, 290, 2133-2137.

Sun, D.-Z., C. Covey, and R. S. Lindzen 2001: Vertical correlations of water vapor in GCMs. *Geophys. Res. Lett.*, 28, 259-262.

Sundqvist, H., 1978: A parameterization scheme for non-convective condensation including prediction of cloud water content. *Quart. J. Roy. Meteor. Soc.*, 104, 667-690

Tanré, D., J.-F. Geleyn and J. Slingo, 1984: First results of the introduction of an advanced aerosol-radiation interaction. Aerosols and their climatic effects. Pages 133-177. Edited by H. Gerber and A. Deepak

Thomas, L., J.C. Cartright, D.P. Watering, 1990: Lidar Observations of the horizontal orientation of ice crystals in cirrus clouds, *Tellus*, 42B, 211.

Tiedtke, M. 1993: Representation of clouds in large-scale models. *Mon. Wea. Rev.*, 121, 3040-3061

Tiedtke, M. 1996: An extension of cloud-radiation parameterization in the ECMWF model: the representation of subgrid-scale variations of optical depth. *Mon. Wea. Rev.*, 124, 745-750

Tinel, C., J. Testud, A. Guyot and K. Caillault, 2000: Cloud parameter retrieval from combined remote sensing observations, Phys. Chem. Earth (B), pp. 1063-1067.

Tompkins, 2001 : Representing the unresolved variability of water vapor and clouds in large-scale models: A prognostic cloud cover parameterization, *J. Atmos. Sci.* (submitted)

Veefkind, P.J., G. de Leeuw, P. A. Durkee, P.B. Russell, P.V. Hobbs and J.M.Livingston, 1999: Aerosol optical depth retrieval using ATSR-2 and AVHRR data during TARFOX, *J. Geophys. Res*, 104, No. D2, 2253-2260

Watts, P.D. 1996: Along-track Scanning Radiometer (ATSR) estimation of cloud droplet size, optical depth and phase, Tech. Proc. of International Radiation Symposium, Wisconsin.

Wetzel, M.A., and L. L. Stowe, 1999: Satellite-observed patterns in stratus microphysics, aerosol optical thickness, and shortwave radiative forcing. *J. Geophys. Res.*, 104, 31287-31299.

Wielicki, B. A., J. T. Suttles, A. J. Heymsfield, R. M. Welch, J. D. Spinhirne, M-L. C. Wu, D. O'C. Starr, L. Parker, and R. F. Arduini, 1990: The 27-28 October FIRE IFO Cirrus Case Study: Comparison of radiative transfer theory with observations by satellite and aircraft. *Month. Weath. Rev.*, 118, 2356-2376.

Wielicki,B. A., B.R. Barkstrom, E.F. Harrison, R.B. Lee III, G.L. Smith, and J.E. Cooper, 1996. Clouds and the Earth's Radiant Energy System (CERES): An Earth Observing System experiment. *Bull. Amer. Meteor. Soc.*, 77, 853-868.

Winker, D.M., R.M. Couch, and M.P: McCornick, (1996): An overview of LITE: NASA's lidar in-space technology experiment, *Proc. IEEE*, 84, 164-180.

Acronyms

ACCD	Accumulation Charge Coupled Device
ACE-Asia	Asian Pacific Regional Atmospheric Chemistry Experiment (IGAC)
ACE	Atmospheric Chemistry Experiment (CSA)
ACECHEM	Atmospheric Composition Explorer for CHEMistry and climate interaction (ESA)
ADEOS	Advanced earth Observing Satellite (NASDA)
ADM/Aeolus	Atmospheric Dynamics Mission (ESA)
AIT	Assembly, Integration and Testing
AMIP	Atmospheric Model Inter-comparison Programme
ARAT	Avion de Recherche Atmosphérique et de Télédétection (France)
ARM	Atmospheric Radiation Measurement program (USA)
ARMA	ATLID Reference Model of the Atmosphere
ATLID	ATmospheric backscatter LIDar
ATSR	Along Track Scanning Radiometer
AVHRR	Advanced Very High Resolution Radiometer
BB	Black Body
BBR	Broad Band Radiometer
BRDF	Bi-directional reflectance distribution
CCD	Charge Coupled Device
CCSR	Center for Climate System Research, University of Tokyo (Japan)
CDAE	Command and Data Acquisition Element
CERES	Clouds and Earth's Radiant Energy System (NASA)
CFC	Chloro-Fluoro-Carbons
CFRP	Carbon Fibre Reinforced Plastic
CNES	Centre National d'Etudes Spatiales (France)
CNRS	Centre National de la Recherche Scientifique (France)
CloudSat	ESSP 2 (NASA, CSA)
CMT	Cadmium-Mercury-Telluride
CPR	Cloud Profiling Radar
CRF	Cloud Radiative Forcing
CRL	Communication Research Laboratory
CSA	Canadian Space Agency (Canada)
DLR	Deutschen Zentrum für Luft- und Raumfahrt
DMSP	Defense Meteorological Satellite Program (USA)
DRU	Distribution and Regulation Unit
DSD	Drop Size Distribution
ECMWF	European Centre for Medium-range Weather Forecasts

EGSE	Electrical Ground Support Equipment
EIK	Extended Interaction Klystron
EOEP	Earth Observation Envelope Programme (ESA)
EOS	Earth Observing System (NASA)
ERBE	Earth Radiation Budget Experiment
ERM	Earth Radiation Mission
ESA	European Space Agency
ESSP	Earth System Science Pathfinder (NASA)
ESSP3-CENA	ESSP 3 – Climatologie Etendue des Nuages et des Aerosols (NASA, CNES)
EUMETSAT	European Organisation for the Exploitation of Meteorological Satellites
FOV	Field-of-View
FPA	Focal Plane Assembly
FTS	Fourier Transform Spectrometer
FWHM	Full Width Half Maximum
GCM	General Circulation Model
GCOM	Global Change Observing Mission (NASDA)
GERB	Geostationary Earth Radiation Experiment
GEWEX	Global Energy and Water cycle EXperiment (WCRP)
GNSS	Global Navigation Satellite System
GOCE	Gravity field and steady-state Ocean Circulation Explorer (ESA)
GOES	Geostationary Operational Environmental Satellite
GPM	Global Precipitation Measurement mission
HSR	High Spectral Resolution
HVPS	High Voltage Power Supply
IASI	Infra-red Atmospheric Sounding Interferometer
IFOV	Instantaneous Field of View
IGAC	International Global Atmospheric Chemistry Project
IMC	Image Motion Compensation
IMG	Interferometric Monitor for Greenhouse gases (MITI)
INDOEX	Indian Ocean Experiment
IPCC	Intergovernmental Panel on Climate Change
IPSL	Institut Pierre Simon Laplace (France)
IR	Infra-Red
ISCCP	International Satellite Cloud Climatology Project
ITCZ	Inter-Tropical Convergence Zone
IWC	Ice Water Content
IWP	Ice Water Path

LEANDRE	Lidars aéroportés pour l'Etude des Aérosols, des Nuages, de la Dynamique, du Rayonnement et du cycle de l'Eau (CNRS, CNES)
LEOP	Launch and Early Orbit Phase
LIDAR	LIght Detection and Ranging
Li-Ion	Lithium Ion
LITE	Lidar In-space Technology Experiment (NASA)
LMD	Laboratoire de Meteorologie Dynamique
LNA	Low Noise Amplifier
LW	Long Wave
LWC	Liquid Water Content
LWP	Liquid Water Path
MCT	Mercury Cadmium Telluride (HgCdTe)
MITI	Ministry of International Trade and Industry (Japan)
MLI	Multi-Layer Insulation
MODIS	MODerate resolution Imaging Spectroradiometer (NASA)
MSCE	Mission operation and Satellite Control Element
MSG	Meteosat Second Generation (EUMETSAT)
MSI	Multi-Spectral Imager
NASA	National Aeronatics and Space Administration (USA)
NASDA	National Space Development Agency of Japan
NEΔT	Noise Equivalent Delta Temperature
NESR	Noise Equivalent Spectral Radiance
NIES	National Institute of Environmental Studies (Japan)
NIR	Near Infra-Red
NOAA	National Oceanic and Atmospheric Administration (USA)
NPOESS	National Polar-orbiting Operational Environmental Satellite System (USA)
NWP	Numerical Weather Prediction
OBMU	On-Board Management Unit
OGSE	Optical Ground Support Equipment
OLR	Out-going Long-wave Radiation
OPD	Optical Path Difference
PAE	Processing and Archiving Element
PC	Photo-Conductive
PMT	Photo-Multiplier Tube
POLDER	POLarization and Directional Earth Radiation (CNES)
PRF	Pulse Repetition Frequency
PV	Photo-Voltaic
RAL	Rutherford Appleton Laboratory (UK)

European Space Agency
Agence spatiale européenne

Contact: ESA Publications Division
c/o ESTEC, PO Box 299, 2200 AG Noordwijk, The Netherlands
Tel. (31) 71 565 3400 - Fax (31) 71 565 5433